

An updated Type II supernova Hubble diagram

E.E.E. Gall^{1,2*}, R. Kotak¹, B. Leibundgut^{3,4}, S. Taubenberger^{2,3}, W. Hillebrandt², M. Kromer^{5,6,7}, W.S. Burgett⁸, K. Chambers⁹, H. Flewelling⁹, M. E. Huber⁹, N. Kaiser⁹, R.P. Kudritzki⁹, E.A. Magnier⁹, N. Metcalfe¹⁰, K. Smith¹, J.L. Tonry⁹, R.J. Wainscoat⁹, and C. Waters⁹

¹ Astrophysics Research Centre, School of Mathematics and Physics, Queen's University Belfast, Belfast BT7 1NN, UK

² Max-Planck-Institut für Astrophysik, Karl-Schwarzschild-Str. 1, DE-85748 Garching-bei-München, Germany

³ ESO, Karl-Schwarzschild-Strasse 2, 85748 Garching, Germany

⁴ Excellence Cluster Universe, Technische Universität München, Boltzmannstrasse 2, DE-85748 Garching-bei-München, Germany

⁵ Heidelberger Institut für Theoretische Studien, Schloss-Wolfsbrunnenweg 35, D-69118 Heidelberg, Germany

⁶ Zentrum für Astronomie der Universität Heidelberg, Institut für Theoretische Astrophysik, Philosophenweg 12, D-69120 Heidelberg, Germany

⁷ The Oskar Klein Centre & Department of Astronomy, Stockholm University, AlbaNova, SE-106 91 Stockholm, Sweden

⁸ GMTO Corporation, 465 N. Halstead St., Suite 250 Pasadena, California 91107, USA

⁹ Institute for Astronomy, University of Hawaii at Manoa, 2680 Woodlawn Drive, Honolulu, Hawaii 96822, USA

¹⁰ Centre for Extragalactic Astronomy, Department of Physics, Durham University, South Road, Durham DH1 3LE, UK

Received 30 May 2017

ABSTRACT

We present photometry and spectroscopy of nine Type II-P/L supernovae (SNe) with redshifts in the $0.045 \lesssim z \lesssim 0.335$ range, with a view to re-examining their utility as distance indicators. Specifically, we apply the expanding photosphere method (EPM) and the standardized candle method (SCM) to each target, and find that both methods yield distances that are in reasonable agreement with each other. The current record-holder for the highest-redshift SN II-P, PS1-13bni ($z = 0.335^{+0.009}_{-0.012}$), illustrates the promise of Type II SNe as cosmological tools. We updated existing EPM and SCM Hubble diagrams by adding our sample to those previously published. Within the context of Type II SN distance measuring techniques, we investigated two related questions. First, we explored the possibility of using spectral lines other than the traditionally used Fe II $\lambda 5169$ to infer the photospheric velocity of SN ejecta. Using local well-observed objects, we derive an epoch-dependent relation between the H α , H β , and Fe II $\lambda 5169$ velocities that is applicable 30-40 d post-explosion. Motivated in part by the continuum of key observables such as rise time and decline rates exhibited from II-P to II-L SNe, we assessed the possibility of using Hubble-flow Type II-L SNe as distance indicators. These yield similar distances as the Type II-P SNe. Although these initial results are encouraging, a significantly larger sample of SNe II-L would be required to draw definitive conclusions.

Key words. Stars: supernovae – distance scale

1. Introduction

The past decades have been marked by an ongoing revolution in cosmology and distance estimation techniques. Following the astounding discovery that the Universe was expanding at an accelerating rate (Riess et al. 1998; Perlmutter et al. 1999), the quest to determine the precise value of the Hubble constant, H_0 , has inspired a host of new distance determination techniques, systematic improvements to old approaches, as well as large-scale focussed projects dedicated to improving the precision in the measurements of H_0 in order to shed light on the constituents of the energy density of the Universe.

Already in the 1980s i.e., before the launch of the Hubble Space Telescope (HST), the measurement of the Hubble constant with an uncertainty of $\lesssim 10\%$ was chosen as one of three HST “Key Projects”. Freedman et al. (2001) presented the final results of this endeavour. Using an array of secondary distance indicators, calibrated using Cepheid distances, they reported a value for H_0 of $72 \pm 8 \text{ km s}^{-1} \text{ Mpc}^{-1}$.

Galaxies for which distance estimates from multiple sources are available are crucial as anchors for the extragalactic distance

scale. One example is NGC 4258, which has estimates for a geometric distance through mega masers (Humphreys et al. 2013), a Cepheid distance (e.g. Fiorentino et al. 2013), and a Type II-P SN distance (Polshaw et al. 2015). NGC 4258 may therefore be a more suitable anchor galaxy than the Large Magellanic Cloud, which was used as the first rung on the distance ladder for a variety of distance estimation techniques (Riess et al. 2011a,b, and references therein).

Recently, the Planck Collaboration XIII (2015) presented the outcomes of observations of the cosmic microwave background, which enabled them to restrict the Hubble constant to $H_0 = 67.8 \pm 0.9 \text{ km s}^{-1} \text{ Mpc}^{-1}$, corresponding to an uncertainty of only 1.3%.

In the latest update, Riess et al. (2016) combined both newly calibrated distance measurements of Cepheid stars and Type Ia SNe, to constrain the Hubble constant to only 2.4% as $H_0 = 73.0 \pm 1.8 \text{ km s}^{-1} \text{ Mpc}^{-1}$.

While the uncertainties in H_0 have decreased significantly over the years, a disagreement at the $2.0 - 2.5\sigma$ level between the values derived via SN Ia cosmology and measurements of the cosmic microwave background has emerged, reflecting a tension between local and global measurements of H_0 . Such a discrep-

* E-mail: egall01@qub.ac.uk

ancy could either imply unknown systematic uncertainties in the measurements of H_0 or that current cosmological models have to be revised (e.g. Bennett et al. 2014). However, Bennett et al. (2014) also argue that the various estimates of H_0 are “consistent within reasonable statistical expectations”.

In this pursuit for the value of H_0 , the “expanding photosphere method” (EPM; Kirshner & Kwan 1974) and “standardized candle method” (SCM; Hamuy & Pinto 2002), two distance measuring techniques utilizing Type II-P SNe, have played a minor role so far. On the most fundamental level, the EPM relies on the comparison of the angular size of an object with the ratio between its observed and theoretical flux, whereas the SCM uses the relation between the expansion velocities of SNe II-P during the plateau phase and its plateau luminosity to determine the distance. The EPM and SCM are subject to different systematics than the previously mentioned techniques and they have both undergone significant improvements from their original description (e.g. Wagoner 1981; Schmidt et al. 1994b; Eastman et al. 1996; Hamuy et al. 2001; Dessart & Hillier 2005; Gall et al. 2016 for the EPM or Nugent et al. 2006; Poznanski et al. 2009 for the SCM), aiming to reduce their systematic uncertainties. In particular, the EPM is independent of the cosmic distance ladder. Additionally, SNe II-P are more common (albeit fainter) than SNe Ia and bear the potential to be observed in statistically significant numbers. In the future, the EPM and SCM may be able to constrain H_0 with similar precision to either the SN Ia or cosmic microwave background measurements.

In this study, we build upon our previous work (Gall et al. 2015, 2016). In Gall et al. (2016) we examined the relativistic effects – specifically the difference between “angular size” and “luminosity” distance – that come into play when applying the EPM to SNe at non-negligible redshifts. We re-derived the basic equations of the EPM, and showed that for SNe at non-negligible redshifts, the angular size, θ , should be corrected by a factor of $(1+z)^2$, and that the observed flux has to be transformed into the SN rest frame. These results were applied to SN 2013eq ($z = 0.041 \pm 0.001$), implementing both EPM and SCM, and demonstrated that the two techniques give consistent results.

However, even in the local Universe the division between SNe II-P – which are typically used for the EPM and SCM – and SNe II-L is ambiguous and has given rise to extensive discussions on whether SNe II-P/L should, or should not be viewed as members of the same class with a continuum of properties. The rise times of a sample of 20 Type II-P and II-L SNe were analyzed in Gall et al. (2015), amongst them LSQ13cuw, a Type II-L SN with excellent constraints on its explosion epoch (< 1 d). We found some evidence for SNe II-L having longer rise times and higher luminosities than SNe II-P, but also indications that a clear separation of SNe II-P/L into two distinct classes can be challenging (see also Anderson et al. 2014; Gonzalez-Gaitan et al. 2015). Given that this distinction is marginal, we investigate the possibility of including SNe II-L into the Hubble diagram.

Here, we push the EPM and SCM techniques further, by applying both techniques to a set of Type II-P/L SNe, with redshifts in the following range: $0.04 < z < 0.34$. As will be discussed below, three SNe in our sample exhibited post-peak decline rates that would be consistent with a Type II-L classification. As we demonstrate, this has little bearing on our approach. Our sample also includes PS1-13bni with a redshift of $z = 0.335^{+0.009}_{-0.012}$ – to the best of our knowledge – the highest-redshift Type II-P SN discovered yet. Herewith, we prepare the path for future surveys that will find statistically significant numbers of SNe II-P/L in the Hubble flow, and provide an independent channel with

which to gain insights into the expansion history of the Universe, its geometry, the nature of dark energy, and other cosmological parameters.

The paper is divided into the following parts: observations of the SNe in our sample are presented in §2; distance measurements using the Expanding Photosphere Method as well as the Standard Candle Method are performed in §3; our main conclusions are given in §4.

2. Observations and data reduction

For this study we acquired a sample of eleven Type II SNe ranging in redshifts from $z \sim 0.04$ to $z \sim 0.34$ (see Table 1). The majority of these objects were discovered by the Panoramic Survey Telescope & Rapid Response System 1 (Pan-STARRS1), a detailed description of which is given in Kaiser et al. (2010). Observations were obtained in the Pan-STARRS1 (PS1) filter system comprising g_{PS1} , r_{PS1} , i_{PS1} , z_{PS1} , and y_{PS1} (see Tonry et al. 2012 for a detailed description of the photometric system). Aside from lying in the desired redshift range, targets were selected for their young age to allow for photometric and spectroscopic follow-up within the first 50 days after explosion.

Additionally, we began follow-up observations of SN 2013ca (also known as LSQ13aco) after announcements both in the Astronomers’ Telegrams¹ (ATels; Walker et al. 2013) and the Central Bureau Electronic Telegrams² (CBET; Zhang et al. 2013). We also include LSQ13cuw (Gall et al. 2015) and SN 2013eq (Gall et al. 2016) in our sample. All three objects fall in the aspired redshift range and fulfill the criterion of having been discovered at a relatively young age. In the following we present the data reduction procedures as well as an overview of the photometric and spectroscopic observations.

2.1. Data reduction

The PS1 data were processed by the Image Processing Pipeline (Magnier 2006), which carries out a number of steps including bias correction, flat-fielding, bad pixel masking and artefact location. Subsequently, difference imaging was performed by subtracting high quality reference images from the new observations. The subtracted images then formed the basis for point-spread function (PSF) fitting photometry.

In cases where the Pan-STARRS1 photometry did not provide sufficient coverage, ancillary imaging was obtained with either RATCam or the Optical Wide Field Camera, IO:O, mounted on the 2m Liverpool Telescope (LT; $g'r'i'$ filters) or the Andalucia Faint Object Spectrograph and Camera, ALFOSC mounted on the Nordic Optical Telescope (NOT; $u'g'r'i'z'$ filters). All data were reduced in the standard fashion using either the LT pipelines or IRAF³. This includes trimming, bias subtraction, and flat-fielding. For PS1-14vk we additionally performed a template subtraction due to its location within the host galaxy (it has a projected distance of ~ 4.5 kpc from the center of the host galaxy). Template images were obtained from the SDSS catalogue in the filters g' , r' , and i' . Point-spread function (PSF) fitting photometry was carried out on all LT and NOT images us-

¹ <http://www.astronomerstelegram.org>.

² <http://www.cbat.eps.harvard.edu/index.html>.

³ IRAF (Image Reduction and Analysis Facility) is distributed by the National Optical Astronomy Observatories, which are operated by the Association of Universities for Research in Astronomy, Inc., under cooperative agreement with the National Science Foundation.

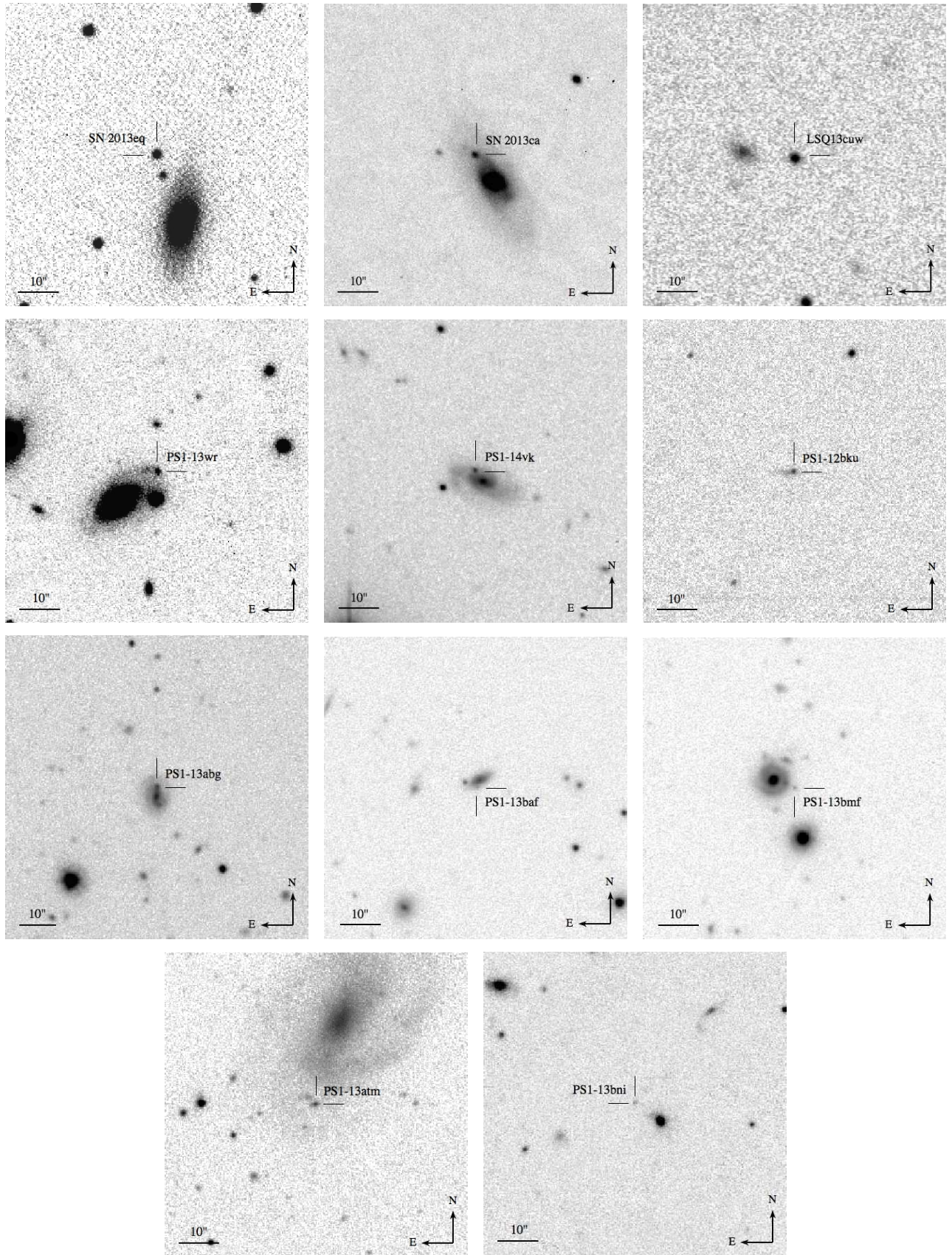


Fig. 1: The SNe in our sample and their environments. Short dashes mark the location of the respective supernova (see Table 1 for the exact coordinates). The images were taken in the SDSS i' -band on MJD 56520.89 for SN 2013eq, the i' -band on MJD 56462.90 for SN 2013ca, the r' -band on MJD 56625.03 for LSQ13cuw, the i_{PS1} -band on MJD 56462.31 for PS1-13wr, the i' -band on MJD 56768.92 for PS1-14vk, the i' -band on MJD 56205.88 for PS1-12bku, the i_{PS1} -band on MJD 56422.29 for PS1-13abg, the i_{PS1} -band on MJD 56414.52 for PS1-13baf, the i_{PS1} -band on MJD 56422.34 for PS1-13bmf, the i_{PS1} -band on MJD 56422.29 for PS1-13atm, and the i_{PS1} -band on MJD 56432.50 for PS1-13bni.

Table 1: Sample of intermediate redshift Type II-P/L SNe

SN	Type	R.A.	Dec.	Host galaxy	$E(B - V)$ [mag] galactic	$E(B - V)$ [mag] host	Redshift
SN 2013eq	II-P	17:33:15.73	+36:28:35.2	-	0.034	0.062 ± 0.028	0.041 ± 0.001
SN 2013ca	II-P	11:58:43.25	+19:08:56.2	PGC 37698	0.029	< 0.04	0.045 ± 0.001
LSQ13cuw	II-L	02:39:57.35	-08:31:24.2	SDSS J023957.37-083123.8	0.023	< 0.16	0.045 ± 0.003
PS1-13wr	II-P	14:15:57.97	+14:15:58.0	SDSS J141558.95+520302.9	0.012	0.110 ± 0.049	0.076 ± 0.001
PS1-14vk	II-L	12:10:45.47	+48:41:46.7	SDSS J121045.27+484143.9	0.020	< 0.09	0.080 ± 0.001
PS1-12bku	II-P	22:16:40.20	-01:08:24.4	SDSS J221640.32-010824.7	0.029	< 0.27	$0.088^{+0.006}_{-0.002}$
PS1-13abg	II-P	10:00:51.10	+02:11:40.0	zCOSMOS 824314	0.014	< 0.07	0.123 ± 0.001
PS1-13baf	II-P	16:16:01.61	+54:58:31.3	SDSS J161601.54+545833.0	0.007	< 0.36	0.144 ± 0.001
PS1-13bmf	II-L	12:23:10.93	+47:44:24.9	SDSS J122311.46+474426.7	0.011	-	0.163 ± 0.001
PS1-13atm	II-L?	09:59:16.60	+03:18:28.3	SDSS J095916.19+031848.5	0.020	-	0.220 ± 0.001
PS1-13bni	II-P	16:12:37.31	+56:18:36.8	SDSS J161236.57+561832.4	0.007	-	$0.335^{+0.009}_{-0.012}$

a) Gall et al. (2016); b) this study; c) NASA/IPAC Extragalactic Database; d) Gall et al. (2015); e) Sloan Digital Sky Survey; f) Lilly et al. (2007)

ing the custom built SNOoPY⁴ package within `IRAF`. Photometric zero points and colour terms were derived using observations of Landolt standard star fields (Landolt 1992) in photometric nights and their averaged values were then used to calibrate the magnitudes of a set of local sequence stars that were in turn used to calibrate the photometry of the SNe in the remainder of nights.

We estimated the uncertainties of the PSF-fitting via artificial star experiments. An artificial star of the same magnitude as the SN was placed close to the position of the SN. The magnitude was measured, and the process was repeated for several positions around the SN. The standard deviation of the magnitudes of the artificial star were combined in quadrature with the uncertainty of the PSF-fit and the uncertainty of the photometric zeropoint to give the final uncertainty of the magnitude of the SN.

Within the restrictions imposed by instrument availability and weather conditions, we obtained a series of three to six optical spectra per SN with the Optical System for Imaging and low-Intermediate-Resolution Integrated Spectroscopy (OSIRIS, grating IDs R300R or R300B) mounted on the Gran Telescopio CANARIAS (GTC). The spectra were reduced using `IRAF` following standard procedures. These included trimming, bias subtraction, flat-fielding, optimal extraction, wavelength calibration via arc lamps, flux calibration via spectrophotometric standard stars, and re-calibration of the spectral fluxes to match the photometry. The spectra were also corrected for telluric absorption using a model spectrum of the telluric bands, which was created using the standard star spectrum.

2.2. The Type II SN sample

An overview of our sample and the SN properties is given in Table 1. A more detailed description of each individual SN is given in Appendix A alongside Figures A.1 to A.9 and Tables A.1-A.18 that present the photometric and spectroscopic observations. Photometry and spectroscopy for LSQ13cuw as well as SN 2013eq are adopted from Gall et al. (2015) and Gall et al. (2016), respectively.

The photometric coverage ranges from rather poor (with just one photometric epoch in g_{PS1} and r_{PS1} for PS1-13atm) to very good (e.g. for PS1-13baf, which has an average 5-8 day cadence coverage in $g_{PS1}r_{PS1}i_{PS1}z_{PS1}$ up to ~ 100 d after discovery). Most SNe show clear plateaus in their light curves, which helps us to

identify them as SNe II-P. The $r_{PS1}i_{PS1}z_{PS1}$ decline rates of PS1-13bni have relatively large uncertainties, however they point towards a II-P classification.

A few SNe, namely LSQ13cuw, PS1-14vk and PS1-13baf, display decline rates after maximum that are higher than 0.5 mag/50 d, which – following the definition by Li et al. (2011) – places them in the SN II-L class. The photometric coverage of PS1-13atm, with just a single observation in the g_{PS1} - and r_{PS1} -band hampers classification. However, PS1-13atm shows only a very weak $H\alpha$ absorption component, which is more of a II-L characteristic (see Gutiérrez et al. 2014). Furthermore the i_{PS1} -band photometry is suggestive of a relatively long rise time ($\sim > 15$ d), which could also be an indication that PS1-13atm is a Type II-L SN.

We are able to constrain the explosion epoch for LSQ13cuw, PS1-12bku, PS1-13abg, PS1-13abg, PS1-13bmf and PS1-13atm to a precision ranging from ± 0.1 d to ± 5.0 d using only photometric data, i.e. via pre-discovery non-detections, or a low-order polynomial fit to the rise time photometry.

All our SNe display the typical lines of $H\alpha$ and $H\beta$ in their spectra. Features stemming from weak lines of iron, in particular $Fe\text{ II } \lambda 5169$ are visible in at least one spectrum for most, albeit not all, of our SNe.

We adopt the redshifts for our SNe either from a spectroscopic redshift of the host galaxy, via identification of host-galaxy lines in the SN spectra or, if neither is available, directly from the SN spectra. The redshifts of our SNe are summarized in Table 1, while details of the redshift determination for the individual objects are given in Appendix A.

The galactic extinction for the SNe in our sample was adopted from the NASA/IPAC Extragalactic Database and is based on the values published by Schlafly & Finkbeiner (2011). A measure of the dust extinction within the SN host galaxy was obtainable only for selected SNe. For SN 2013eq a value of $E(B - V)_{SN 2013eq}^{host} = 0.062 \pm 0.028$ was adopted from Gall et al. (2016). Weak $Na\text{ I D}$ absorptions, are visible in the PS1-13wr spectra, which we use to determine the host galaxy extinction: $E(B - V)_{PS1-13wr}^{host} = 0.110 \pm 0.049$ (applying Equation 9 from Poznanski et al. 2012). In most other cases we derived an upper limit to the equivalent width of the $Na\text{ I D}$ absorption and the extinction within the host galaxy. This process is described in detail in Appendix A.2. For our three highest- z SNe PS1-13bmf, PS1-13atm and PS1-13bni, we are not able to obtain a meaning-

⁴ SuperNOva PhotometrY, a package for SN photometry implemented in `IRAF` by E. Cappellaro; <http://sngroup.oapd.inaf.it/snoopy.html>.

ful upper limit for the EW of the Na I D blend, due to the poor signal-to-noise ratio of their spectra.

3. Results and discussion

The EPM has been applied to a variety of SNe II. Detailed discussions of the EPM as well as examples of applying this technique in practice can be found e.g. in Kirshner & Kwan (1974), Schmidt et al. (1994a), Hamuy et al. (2001), Leonard et al. (2002a), Dessart & Hillier (2005), or Jones et al. (2009). Here, we will closely follow the approach presented in Gall et al. (2016), who explore relativistic effects when applying the EPM to SNe at intermediate redshifts. We will use the dilution factors for the filter combination $\{BVI\}$ as presented by Hamuy et al. (2001) and Dessart & Hillier (2005), respectively.

The SCM has been developed in Hamuy & Pinto (2002), Nugent et al. (2006), Poznanski et al. (2009), and D’Andrea et al. (2010). We follow the approach of Nugent et al. (2006), who modified the technique to be applicable for SNe at cosmologically significant redshifts.

In the following, we give a short overview of the use of SNe II-L as distance indicators up to this point (see Section 3.1) and then present the preparatory steps required to apply either the EPM or the SCM. These are the application of K -corrections (Section 3.2) and the determination of the temperatures (Section 3.3) and expansion velocities (Section 3.4). In particular, we will explore the possibility of using the $H\alpha$ - or $H\beta$ -velocities to estimate the photospheric velocity of Type II-P SNe (see Section 3.4.2). We then apply the EPM (Section 3.5) and SCM (Section 3.6) to our sample and compare the results in Section 3.7. Finally we create an EPM and a SCM Hubble diagram (Section 3.8) and investigate the implications of applying the EPM and SCM also to Type II-L SNe (Section 3.9).

3.1. Type II-L SNe as distance indicators

Traditionally, Type II-L SNe were not explicitly used as distance indicators and in some cases even discarded completely. Nonetheless, SNe II-L have occasionally found their way into EPM and SCM samples. One such example is the Type II-L SN 1979C, for which Eastman et al. (1996) find an EPM distance of 15 ± 4 Mpc, consistent with the Cepheid distance of its host galaxy, NGC 4321 (~ 17 Mpc, e.g. Freedman et al. 1994). Another case is the Type II-L SN 1990K which was included in the SCM sample of Hamuy & Pinto (2002). Moreover, some SNe in the intermediate redshift SCM sample of Nugent et al. (2006) appear to have relatively steeply declining light curves (see e.g. SNLS-03D4cw in their Figure 7 or SNLS-04D1ln in their Figure 8).

Poznanski et al. (2009) select only objects with the lowest decline rates – i.e. Type II-P SNe – for their SCM sample, claiming that this reduces the scatter in the Hubble diagram. However, they also admit that only some of the steeper declining SNe II defy the velocity-luminosity correlation, while others do appear to be as close to the Hubble line as the rest of their sample. This was noted also by D’Andrea et al. (2010), who find that “none of the five most deviant SNe in [their] sample would be removed using the decline rate method.”

From a physical point of view we expect no fundamental difference between the progenitors of SNe II-P and II-L, i.e. we assume a one-parameter continuum depending mainly on the mass of the hydrogen envelope of the progenitor star at the time of explosion. Of course, other factors (like metallicity) may influence

the details of the explosion and its observational characteristics and thereby affect the precision of distance measurements.

Here, we will keep those objects with more steeply declining light curves in our sample, aiming to identify potential strengths and weaknesses of a more inclusive approach towards the use of Type II-L SNe as cosmological probes.

3.2. K -corrections

In order to correctly apply the EPM in combination with the $\{BVI\}$ dilution factors, as well as for consistency and inter-comparability within our own sample, the photometric data available for the SNe need to be converted to the Johnson-Cousins filter system. Additionally, both the EPM and the SCM require the photometry to be transformed into the rest frame of each SN (see Equation 13 in Gall et al. 2016).

We perform the transformations from the observed photometry to the rest frame Johnson-Cousins BVI filters in one step by calculating K -corrections with the SNAKE code (SuperNova Algorithm for K -correction Evaluation) within the S3 package (Inserra et al. 2016). We proceed in slightly different ways for the more nearby objects in our sample, the more distant ones, and for PS1-13bni, which is our highest- z object. This is described in detail in the following.

SNe with $z < 0.13$: for these SNe the spectral coverage is sufficient to estimate valid K -corrections and consequently, the spectra of each SN are used for this purpose.

SNe PS1-13baf, PS1-13bmf and PS1-13atm: due to their redshifts above $z \sim 0.14$ the spectra of these SNe only partly cover the rest frame I -band. For this reason we combined the spectra of these three SNe with spectra from SNe 2013eq and 2013ca at similar epochs to obtain more accurate estimates for the respective K -corrections.

For PS1-13bni, our highest redshift SN with $z = 0.335^{+0.009}_{-0.012}$, we calculate the K -corrections to the rest frame I -band using SN 2013eq and 2013ca spectra, and interpolate these to the epochs of the PS1-13bni spectra. This should give valid results considering that most SNe II-P/L are relatively homogeneous in their spectral and consequently, their temperature evolution. Nonetheless, a small error in the I -band K -corrections for PS1-13bni cannot be excluded due to the unknown explosion times and thereby exact epochs of either SNe 2013eq, 2013ca or PS1-13bni. The K -corrections to the rest frame B - and V -band are calculated using the PS1-13bni spectroscopy.

3.3. Temperature evolution

In preparation for a temperature determination, the uncorrected observed photometry for each SN, is interpolated to the epochs of spectroscopic observations and subsequently dereddened and K -corrected. For PS1-12bku, where photometry from multiple sources is available we first interpolate the K -corrections for each instrument to the epochs of photometric observations and then correct the K -corrected photometry for dust extinction. The dereddened and K -corrected B , V , and I -band light curves are then interpolated to the epochs of spectroscopic observations.

Finally, the rest frame BVI magnitudes are converted into physical fluxes and the temperature at each epoch and for all SNe, is estimated via a blackbody fit to the BVI -fluxes at the respective effective wavelengths. With the aim to estimate the uncertainties of the temperatures we performed additional blackbody fits to all combinations of extrema of the SN fluxes. The standard deviation of the resulting array of temperatures was

taken as a conservative estimate of the temperature's uncertainty. As in Gall et al. (2016) we used this technique aiming to exhaust all available information in all bands.

The results are presented in Table B.1 in the appendix.

3.4. Velocities

3.4.1. Fe II $\lambda 5169$

The EPM and the SCM require an estimate of the photospheric velocities. It has been argued that the Fe II $\lambda 5169$ absorption minimum provides a reasonable estimate of the photospheric velocity (Dessart & Hillier 2005). While the use of other weak lines, such as Fe II $\lambda 5018$, or Fe II $\lambda\lambda 4629, 4670, 5276, 5318$ has also been discussed (e.g. Leonard et al. 2002a; Leonard 2002), here we will advance using the Fe II $\lambda 5169$ velocities when available, for the main reason, that the relatively low quality of the spectra for our more distant SNe renders the measurement of other weak lines impossible. For this same reason we also explore the possibility to estimate the Fe II $\lambda 5169$ velocity via the H α or H β velocities in the subsequent section.

3.4.2. Using H α and H β to estimate photospheric velocities

Nugent et al. (2006) explored the ratio between the H β and the Fe II $\lambda 5169$ velocities and found a correlation. Poznanski et al. (2010) later improved this correlation and found that the Fe II $\lambda 5169$ velocities stand in a linear relation with the H β velocities⁵: $v_{H\beta}/v_{Fe\,5169} = 1.19^{+0.08}_{-0.07}$. They included spectra from epochs between 5 and 40 days post-explosion.

In order to test this relation we put together a set of five very well observed Type II-P SNe from the literature: SN 1999em (Leonard et al. 2002a; Leonard 2002), SN 1999gi (Leonard et al. 2002b), SN 2004et (Sahu et al. 2006), SN 2005cs (Pastorello et al. 2006, 2009), and SN 2006bp (Quimby et al. 2007). These objects were carefully selected on the basis of the quality and cadence of their available spectroscopy as well as for the good constraints on their explosion epochs. Note that none of the selected objects is of Type II-L, which might potentially show a different velocity evolution than SNe II-P. A more detailed discussion on this matter will follow in Section 3.4.3.

We determined the H β and Fe II $\lambda 5169$ velocities up to ~ 70 d post explosion for these SNe using `IRAF` by fitting a Gaussian function to the minima of the respective lines and assumed an uncertainty of 5 % for all velocity measurements. Subsequently, we performed exponential fits to the velocity evolution for each line and each SN, respectively following:

$$v(t^*) = a e^{-bt^*} + c, \quad (1)$$

where $v(t^*)$ is the velocity of a particular line at time t^* since explosion (rest frame)⁶ and a , b , and c are the fit parameters. The uncertainty of each fit was estimated by calculating the root mean square of the deviation between the data and the fit. The explosion times for the five SNe were assumed to be as given in Gall et al. (2015, and references therein). The fit parameters are given in Table B.2 in the appendix.

⁵ Poznanski et al. (2010) give the relation in the form: $v_{Fe\,5169} = (0.84 \pm 0.05) v_{H\beta}$. We converted this into a $v_{H\beta}/v_{Fe\,5169}$ ratio for easier comparability with our results.

⁶ Throughout this paper we adopt the notation of Gall et al. (2016) in that variables in the SN rest frame will be marked with “ \star ”, while “ \diamond ” denotes variables in the observer frame.

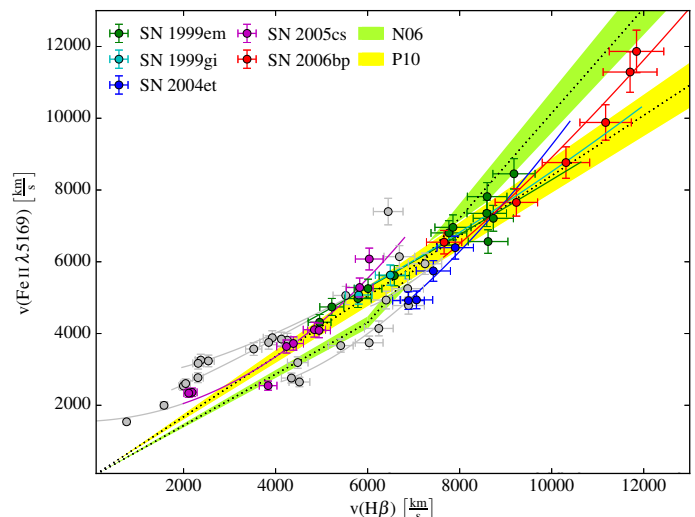


Fig. 2: Comparison of H β and Fe II $\lambda 5169$ velocities. The coloured points correspond to velocities measured between 5 and 40 days from explosion, while the gray points represent epochs either within 5 days of the explosion or after 40 days. The solid lines correspond to the fitted evolution of the H β and Fe II $\lambda 5169$ velocities for each SN. The green and yellow shaded regions reflect the $v_{H\beta}/v_{Fe\,5169}$ ratios as presented by Nugent et al. (2006) and Poznanski et al. (2010).

In Figure 2 we show the resulting relation between the H β and Fe II $\lambda 5169$ velocities in comparison with the corresponding relation as given by Nugent et al. (2006) and Poznanski et al. (2010) (areas shaded in green and yellow). The coloured points mark velocities measured between 5 and 40 days after explosion, while the gray points depict velocities measured either before day 5 or after day 40. While the relations from Nugent et al. (2006) and Poznanski et al. (2010) follow the general trend of the data, it is also clear that in particular at later epochs the velocities of the individual SNe evolve “away” from the linear relations. The fitted velocity evolution for each SN – depicted as solid lines in Figure 2 – is not linear (as the Poznanski et al. (2010) relation) but rather a curve, only part of which lies in the linear regime.

Obviously, a linear relation between H β and Fe II $\lambda 5169$ velocities neglects a certain degree of epoch dependence. We therefore take a slightly different approach than Nugent et al. (2006) or Poznanski et al. (2010) in that we investigate the ratio between the H β and the Fe II $\lambda 5169$ velocities not as a function of velocity but rather as a function of time (i.e. epoch since explosion). At the same time, we also explore the viability of a relation between the H α and the Fe II $\lambda 5169$ velocities, which might be a potential asset when dealing with spectra from high- z SNe II (such as those that will be routinely discovered by the LSST⁷) in which neither Fe II $\lambda 5169$ nor H β can be detected.

We interpolated the H α , H β and Fe II $\lambda 5169$ velocities to all epochs up to ~ 70 days after explosion and then calculated the $v_{H\alpha}/v_{Fe\,5169}$ and $v_{H\beta}/v_{Fe\,5169}$ ratios for each epoch and each SN, respectively (Figure 3). The uncertainties of the individual line fits were propagated to estimate the uncertainty of the ratios. We then averaged the $v_{H\alpha}/v_{Fe\,5169}$ and $v_{H\beta}/v_{Fe\,5169}$ ratios of the five SNe for each epoch (represented as black points in Figure 3). The uncertainties were estimated by adding the uncertainties of the individual SN line ratios and the standard deviation of the

⁷ Large Synoptic Survey Telescope: www.lsst.org.

Table 2: $v_{\text{H}\alpha}/v_{\text{Fe}\lambda 5169}$ ratio

Epoch*	Ratio**	Epoch*	Ratio**
5.0	1.14 ± 0.14	23.0	1.41 ± 0.09
6.0	1.16 ± 0.14	24.0	1.42 ± 0.09
7.0	1.18 ± 0.13	25.0	1.43 ± 0.09
8.0	1.19 ± 0.13	26.0	1.44 ± 0.09
9.0	1.21 ± 0.12	27.0	1.44 ± 0.09
10.0	1.23 ± 0.12	28.0	1.45 ± 0.08
11.0	1.24 ± 0.12	29.0	1.46 ± 0.08
12.0	1.26 ± 0.11	30.0	1.47 ± 0.08
13.0	1.27 ± 0.11	31.0	1.47 ± 0.08
14.0	1.29 ± 0.11	32.0	1.48 ± 0.08
15.0	1.30 ± 0.11	33.0	1.48 ± 0.08
16.0	1.32 ± 0.10	34.0	1.49 ± 0.08
17.0	1.33 ± 0.10	35.0	1.49 ± 0.08
18.0	1.34 ± 0.10	36.0	1.49 ± 0.08
19.0	1.36 ± 0.10	37.0	1.50 ± 0.08
20.0	1.37 ± 0.10	38.0	1.50 ± 0.09
21.0	1.38 ± 0.10	39.0	1.50 ± 0.09
22.0	1.39 ± 0.09	40.0	1.50 ± 0.10

*Epoch from explosion in SN rest frame.

**Averaged ratio between $\text{H}\alpha$ and $\text{Fe}\text{II}\lambda 5169$ velocities.

five values at each epoch in quadrature. The latter is the dominant contributor to the uncertainty, which means that the velocity evolution is distinct for each SN. The results of our endeavour are presented in Figure 3 as well as Table 2 for the $v_{\text{H}\alpha}/v_{\text{Fe}\lambda 5169}$ ratio and Table 3 for the $v_{\text{H}\beta}/v_{\text{Fe}\lambda 5169}$ ratio.

It is immediately apparent that the individual $v_{\text{H}\alpha}/v_{\text{Fe}\lambda 5169}$ or $v_{\text{H}\beta}/v_{\text{Fe}\lambda 5169}$ ratios of the five SNe match well at early epochs both for $\text{H}\alpha$ and $\text{H}\beta$. After about 40 days for $\text{H}\alpha$ and about 30 days for $\text{H}\beta$ the velocity ratios to $\text{Fe}\text{II}\lambda 5169$ of the various SNe begin to diverge significantly. A possible explanation is that during the cooling phase of the SN after the shock breakout, Type II-P SNe display relatively homogeneous properties: the hydrogen envelope is still fully ionized and the ejecta are expanding and cooling. Hydrogen recombination sets in only after a few weeks and differences between the individual SNe in progenitor size, composition, or hydrogen envelope mass become apparent. This is reflected in the variety of luminosities and velocities observed for SNe II-P/L – in fact the relation between luminosity and velocity builds the basis for the standardized candle method (Hamuy & Pinto 2002). These differences are echoed also in the $v_{\text{H}\alpha}/v_{\text{Fe}\lambda 5169}$ or $v_{\text{H}\beta}/v_{\text{Fe}\lambda 5169}$ ratios. A related pattern seems to be that the most extreme SNe in terms of deviation from the average ratios, SNe 2004et and 2005cs, display a relatively high (~ -17.2 mag for SN 2004et) or rather low (~ -15.1 mag for SN 2005cs) R/r -band maximum brightness compared to the other objects (ranging between -16.5 and -16.9 mag). This suggests that the uncertainties in the $v_{\text{H}\alpha}/v_{\text{Fe}\lambda 5169}$ or $v_{\text{H}\beta}/v_{\text{Fe}\lambda 5169}$ ratios could potentially be reduced by taking the absolute magnitudes of the individual objects into account. We encourage such an attempt whenever more objects with suitable data (constraints on the explosion epoch and good spectral coverage) become available.

Overall, the $v_{\text{H}\beta}/v_{\text{Fe}\lambda 5169}$ ratio is flatter than the $v_{\text{H}\alpha}/v_{\text{Fe}\lambda 5169}$ ratio, suggesting that it is less epoch dependent. In fact, one could view the $v_{\text{H}\beta}/v_{\text{Fe}\lambda 5169}$ ratio as constant within the errors between 5 and 30 days after explosion, which is in agreement with the results from Poznanski et al. (2010, shown in yellow in the right panel of Figure 3.). This statement does not hold for the $v_{\text{H}\alpha}/v_{\text{Fe}\lambda 5169}$ ratio.

Table 3: $v_{\text{H}\beta}/v_{\text{Fe}\lambda 5169}$ ratio

Epoch*	Ratio**	Epoch*	Ratio**
5.0	1.09 ± 0.09	18.0	1.17 ± 0.04
6.0	1.09 ± 0.09	19.0	1.17 ± 0.04
7.0	1.10 ± 0.08	20.0	1.18 ± 0.04
8.0	1.11 ± 0.07	21.0	1.18 ± 0.05
9.0	1.12 ± 0.07	22.0	1.18 ± 0.05
10.0	1.12 ± 0.07	23.0	1.19 ± 0.05
11.0	1.13 ± 0.06	24.0	1.19 ± 0.05
12.0	1.14 ± 0.06	25.0	1.19 ± 0.06
13.0	1.14 ± 0.05	26.0	1.19 ± 0.06
14.0	1.15 ± 0.05	27.0	1.19 ± 0.07
15.0	1.16 ± 0.05	28.0	1.19 ± 0.07
16.0	1.16 ± 0.05	29.0	1.19 ± 0.08
17.0	1.17 ± 0.04	30.0	1.19 ± 0.08

*Epoch from explosion in SN rest frame.

**Averaged ratio between $\text{H}\beta$ and $\text{Fe}\text{II}\lambda 5169$ velocities.

3.4.3. Velocities in Type II-L SNe

The $v_{\text{H}\alpha}/v_{\text{Fe}\lambda 5169}$ and $v_{\text{H}\beta}/v_{\text{Fe}\lambda 5169}$ relations derived above were created using only Type II-P SNe. While we expect SNe II-L to display similar properties in their velocity evolution as SNe II-P, we caution that applying the relations also for SNe II-L might introduce some systematic biases, e.g. due to the fact that SNe II-L are generally believed to produce more energetic ejecta than SNe II-P. It is also unclear whether the $v_{\text{H}\alpha}/v_{\text{Fe}\lambda 5169}$ and $v_{\text{H}\beta}/v_{\text{Fe}\lambda 5169}$ ratios of individual SNe II-L would diverge at the same epoch as for SNe II-P.

Additional – more practical – complications when using SNe II-L might emerge due to the fact that they typically show smaller absorption components in their $\text{H}\alpha$ features compared to SNe II-P (Gutiérrez et al. 2014). As the very extreme case of LSQ13cuw shows (see Section 3.5.4) this can make a velocity determination challenging.

3.5. EPM distances

To measure the EPM distances for the SNe in our sample we apply Equations 13 and 14 from Gall et al. (2016):

$$\theta^\dagger = 2 \sqrt{\frac{f_{\star,F}^{\text{dered}}}{\zeta_{\star,BVI}^2(T_{\star,BVI}) \pi B(\lambda_{\star,\text{eff}_F}, T_{\star,BVI})}}, \quad (2)$$

and

$$\chi = \frac{\theta^\dagger}{2v} = \frac{t^* - t_0^*}{D_L}, \quad (3)$$

where $\theta^\dagger = \theta/(1+z)^2$ is the modified “angular size” of the SN, $f_{\star,F}^{\text{dered}}$ is the rest frame flux for the filter F , $\zeta_{\star,BVI}(T_{\star,BVI})$ is the rest frame dilution factor for the filter combination $\{BVI\}$ at the rest frame BVI -temperature $T_{\star,BVI}$, $\lambda_{\star,\text{eff}_F}$ is the effective wavelength of the corresponding filter F , in the rest frame, $B(\lambda_{\star,\text{eff}_F}, T_{\star,BVI})$ is the black body function, v is the photospheric velocity, t^* the time after explosion at t_0^* in the SN frame, and D_L is the luminosity distance of the SN.

As in Gall et al. (2016) we use the temperature dependent $\{BVI\}$ dilution factors presented by Hamuy et al. (2001, based on the dilution factors calculated by Eastman et al. 1996) and Dessart & Hillier (2005). The $\text{Fe}\text{II}\lambda 5169$ velocities were used to determine the distance to the SNe if they could be measured

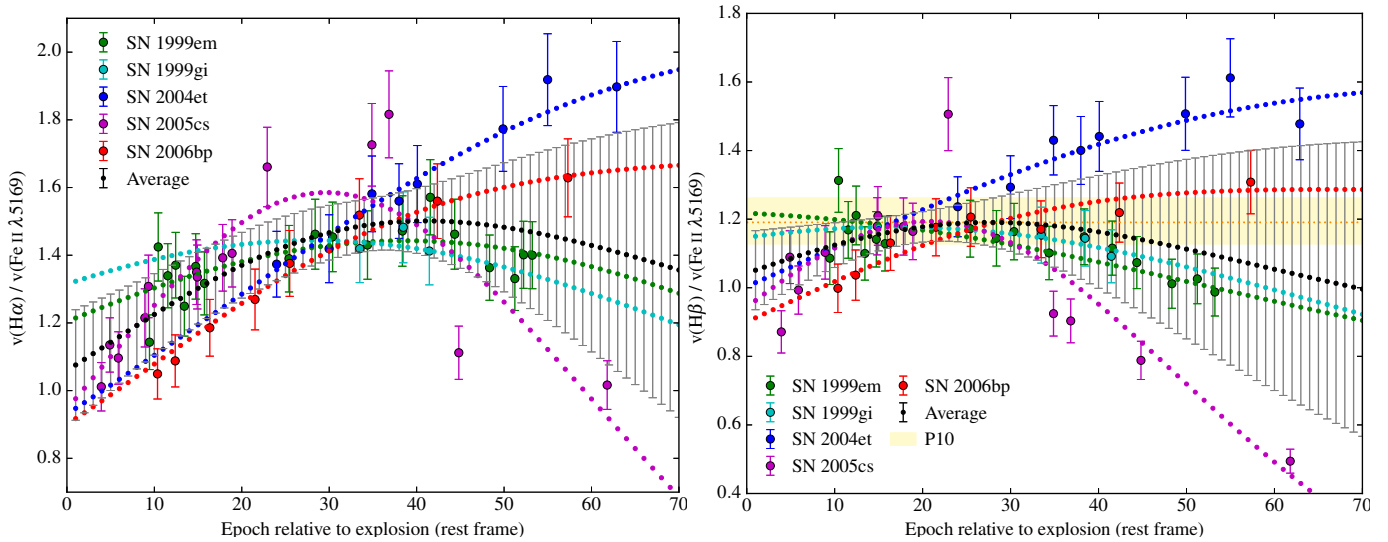


Fig. 3: $v_{\text{H}\alpha}/v_{\text{Fe II} \lambda 5169}$ ratio (left panel) and $v_{\text{H}\beta}/v_{\text{Fe II} \lambda 5169}$ ratio (right panel) compared to the rest frame epoch (from explosion). The thick dotted lines represent the $v_{\text{H}\alpha}/v_{\text{Fe II} \lambda 5169}$ and $v_{\text{H}\beta}/v_{\text{Fe II} \lambda 5169}$ ratios for the individual SNe as well as the averaged ratios. For reasons of better visibility the uncertainty is depicted only for the averaged ratios and not for the fitted velocity ratios of the individual SN. The circle markers represent the measured $v_{\text{H}\alpha}/v_{\text{Fe II} \lambda 5169}$ and $v_{\text{H}\beta}/v_{\text{Fe II} \lambda 5169}$ ratios for those epochs and SNe where spectroscopic data was available and both $\text{H}\alpha$ (or $\text{H}\beta$) and the $\text{Fe II} \lambda 5169$ velocity could be measured. The yellow shaded band in the right panel corresponds to the ratio of $v_{\text{H}\beta}/v_{\text{Fe II} \lambda 5169} = 1.19^{+0.08}_{-0.07}$ as given by Poznanski et al. (2010).

in the SN spectra. For those SNe where the $\text{Fe II} \lambda 5169$ feature could not be confidently identified, we instead applied the $v_{\text{H}\alpha}/v_{\text{Fe II} \lambda 5169}$ and/or $v_{\text{H}\beta}/v_{\text{Fe II} \lambda 5169}$ ratio, to estimate the photospheric velocities and in turn the distance to the SN.

This was done by calculating the values of χ for each filter (B , V , and I) and epoch, respectively and then performing a linear fit using D_L and t_0^* as parameters. With the aim to estimate the uncertainties of both the distance and the time of explosion we performed additional fits to all combinations of adding or subtracting the uncertainties of χ . The standard deviation of the resulting arrays of distances and explosion times was taken as a conservative estimate of their respective uncertainties.

3.5.1. Commonalities

Figures 4 and 5 show the distance fits for PS1-14vk and are representative for the $\chi-t^*$ -fits made for all SNe (see Figures C.1-C.8 in Appendix C). We use PS1-14vk as an example to outline a number of commonalities.

- The results using either the dilution factors by Hamuy et al. (2001) or Dessart & Hillier (2005) are very similar for all SNe, although applying the dilution factors by Dessart & Hillier (2005) systematically yields slightly larger distances.
- As in the case of SN 2013eq (see Gall et al. 2016) the V -band distance is typically smaller and the explosion epoch later than for the BI -bands. The exception of the rule is PS1-13baf, where the V -band distances are larger than derived from B - and I -band. Discrepancies in the EPM distances when using different filter combinations have previously been observed (e.g. Hamuy et al. 2001; Jones et al. 2009).
- For some SNe the photometry provides independent estimates of the time of explosion. In these cases we use the “observed” explosion epoch as an additional data point in the fit and are able to significantly reduce the error in the distance determination.

- In Section 3.4.2 we derived an epoch dependent $v_{\text{H}\beta}/v_{\text{Fe II} \lambda 5169}$ ratio, which after about 30 days begins to diverge significantly for the individual SNe. In those cases where we apply this ratio, we therefore only include data up to ~ 30 days from explosion.
- Jones et al. (2009) argue that after around 40 days from explosion the linearity of the θ/v versus t relation in Type II-P SNe deteriorates. Considering the scarcity of data points for our SNe, we use data up to ~ 60 days from explosion for the distance fits, whenever viable. For the SNe in our sample the $\chi-t^*$ relation seems to be linear also in this extended regime. Even for PS1-14vk; a Type II-L SN, the comparison between Figures 4 and 5 illustrates a breakdown in the linearity of the $\chi-t^*$ relation only in the interval between +33 and +49 days after discovery. Taking into account the epoch of explosion ~ 20 days before discovery, this corresponds to a breakdown in the linearity of the $\chi-t^*$ relation sometime between ~ 50 and ~ 70 days post explosion. When performing a $\chi-t^*$ fit beyond the linear regime the distances are overestimated significantly and the estimated epoch of explosion is considerably earlier than when using only the linear regime.
- Our errors on the distances (averaged over the BVI filters) span a wide range between $\sim 3\%$ and $\sim 54\%$, essentially depending on the quality of the available data for each SN. E.g. a strong constraint on the epoch of explosion reduces the uncertainty of the distance fit significantly. The errors account for the uncertainties from the photometry, the SN redshift, the K -corrections, the photospheric velocities and – for SNe 2013eq and PS1-13wr – the dust extinction in the host galaxy.

The velocities and dilution factors that were used to derive various values of θ^* are presented in Table B.3 in the appendix, while our final distance results are summarized in Table 4. We have taken great care to proceed with all SNe in the same manner as far as possible. Nonetheless, a case-by-case evaluation cannot be avoided entirely. In the following we outline the particularities for each individual SN.

Table 4: EPM distances and explosion times for the SNe in our sample

SN	Dilution factor	Filter	D_L Mpc	Averaged D_L Mpc	t_0^* days*	Averaged t_0^* days*	t_0^\diamond MJD	Estimate of t_0 via
SN 2013ca	H01	<i>B</i>	237 ± 129		13.5 ± 21.5			
		<i>V</i>	170 ± 43	216 ± 51	0.9 ± 10.6	$9.3^{+9.7}_{-9.3}$	$56382.3^{+9.7}_{-10.1}$	
		<i>I</i>	242 ± 72		13.6 ± 16.4			
	D05	<i>B</i>	247 ± 115		9.3 ± 21.3			EPM
		<i>V</i>	180 ± 43	227 ± 47	-1.7 ± 9.2	$5.7^{+9.0}_{-5.7}$	$56386.1^{+5.9}_{-9.4}$	
		<i>I</i>	253 ± 68		9.4 ± 13.6			
LSQ13cuw	H01 – H β	<i>B</i>	267 ± 49					
		<i>V</i>	270 ± 42	267 ± 24				
		<i>I</i>	263 ± 34					
	D05 – H β	<i>B</i>	306 ± 57					
		<i>V</i>	310 ± 48	306 ± 28			56593.4 ± 0.7	G15
		<i>I</i>	303 ± 39					
PS1-13wr	H01	<i>B</i>	325 ± 200		19.2 ± 22.7			
		<i>V</i>	282 ± 161	309 ± 93	15.9 ± 22.1	17.7 ± 11.6	56330.5 ± 12.5	
		<i>I</i>	319 ± 113		18.1 ± 14.4			
	D05	<i>B</i>	347 ± 200		17.5 ± 24.1			
		<i>V</i>	302 ± 161	330 ± 94	14.5 ± 19.7	16.2 ± 11.3	56332.2 ± 12.1	
		<i>I</i>	341 ± 115		16.5 ± 13.1			
PS1-14vk	H01 – all	<i>B</i>	1149 ± 887		79.3 ± 20.9			
		<i>V</i>	624 ± 214	921 ± 333	39.8 ± 19.3	59.8 ± 11.4	56675.9 ± 12.4	
		<i>I</i>	989 ± 409		60.5 ± 19.2			
	H01 – lin	<i>B</i>	532 ± 738		26.0 ± 18.0			
		<i>V</i>	375 ± 142	480 ± 260	15.9 ± 13.2	21.8 ± 9.4	56717.0 ± 10.1	
		<i>I</i>	534 ± 210		23.4 ± 17.0			
	D05 – all	<i>B</i>	1147 ± 953		67.6 ± 20.4			
		<i>V</i>	649 ± 201	934 ± 346	34.9 ± 19.1	51.6 ± 11.2	56684.8 ± 12.1	
		<i>I</i>	1005 ± 356		52.3 ± 18.7			
	D05 – lin	<i>B</i>	564 ± 570		23.1 ± 19.6			
		<i>V</i>	403 ± 142	511 ± 207	14.1 ± 11.6	19.3 ± 9.0	56719.6 ± 9.7	
		<i>I</i>	567 ± 203		20.8 ± 14.5			
PS1-12bku	H01	<i>B</i>	357 ± 43					
		<i>V</i>	349 ± 34	357 ± 21				
		<i>I</i>	366 ± 29					
	D05	<i>B</i>	409 ± 49					
		<i>V</i>	399 ± 39	409 ± 24			56160.9 ± 0.4	PS1
		<i>I</i>	419 ± 33					
PS1-13abg	H01	<i>B</i>	474 ± 54					
		<i>V</i>	440 ± 47	459 ± 29				
		<i>I</i>	463 ± 47					
	D05	<i>B</i>	505 ± 58					
		<i>V</i>	469 ± 50	489 ± 30			56375.4 ± 5.0	PS1
		<i>I</i>	494 ± 50					
PS1-13baf	H01 – H β	<i>B</i>	689 ± 740					
		<i>V</i>	717 ± 426	690 ± 294				
		<i>I</i>	666 ± 221					
	D05 – H β	<i>B</i>	790 ± 854					
		<i>V</i>	821 ± 490	792 ± 339			56408.0 ± 1.5	PS1
		<i>I</i>	763 ± 254					
PS1-13bmf	H01	<i>B</i>	620 ± 40					
		<i>V</i>	606 ± 34	622 ± 21				
		<i>I</i>	639 ± 35					
	D05	<i>B</i>	705 ± 45					
		<i>V</i>	689 ± 39	707 ± 24			56420.0 ± 0.1	PS1
		<i>I</i>	727 ± 41					
PS1-13bni	H01 – H β	<i>B</i>	1699 ± 451		7.3 ± 12.4			
		<i>V</i>	1538 ± 1109	1772 ± 538	5.4 ± 8.3	8.1 ± 5.9	56401.3 ± 7.9	
		<i>I</i>	2078 ± 1082		11.7 ± 9.7			
	D05 – H β	<i>B</i>	2019 ± 542		8.6 ± 13.6			
		<i>V</i>	1823 ± 1349	2110 ± 658	6.6 ± 8.8	9.5 ± 6.4	56400.0 ± 8.6	
		<i>I</i>	2488 ± 1336		13.4 ± 10.5			

*Days in SN rest frame before discovery. H01 = Hamuy et al. (2001); D05 = Dessart & Hillier (2005); G15 = Gall et al. (2015). PS1 = PanSTARRS1 photometry and/or non-detections.

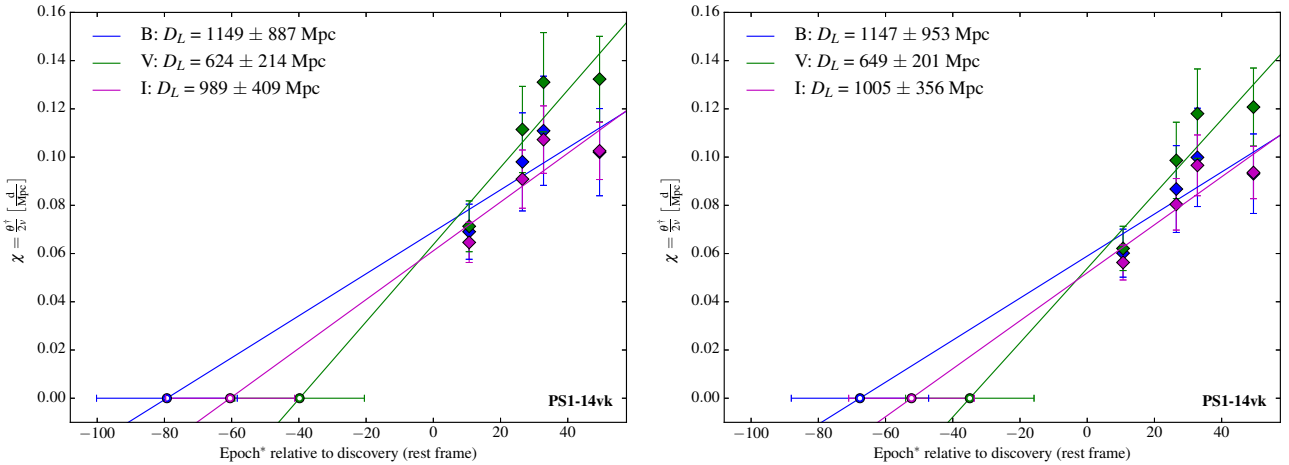


Fig. 4: Distance fit for PS1-14vk using all available epochs and ζ_{BVI} as given in Hamuy et al. (2001) (left panel) and Dessart & Hillier (2005) (right panel). The diamond markers denote values of χ through which the fit is made.

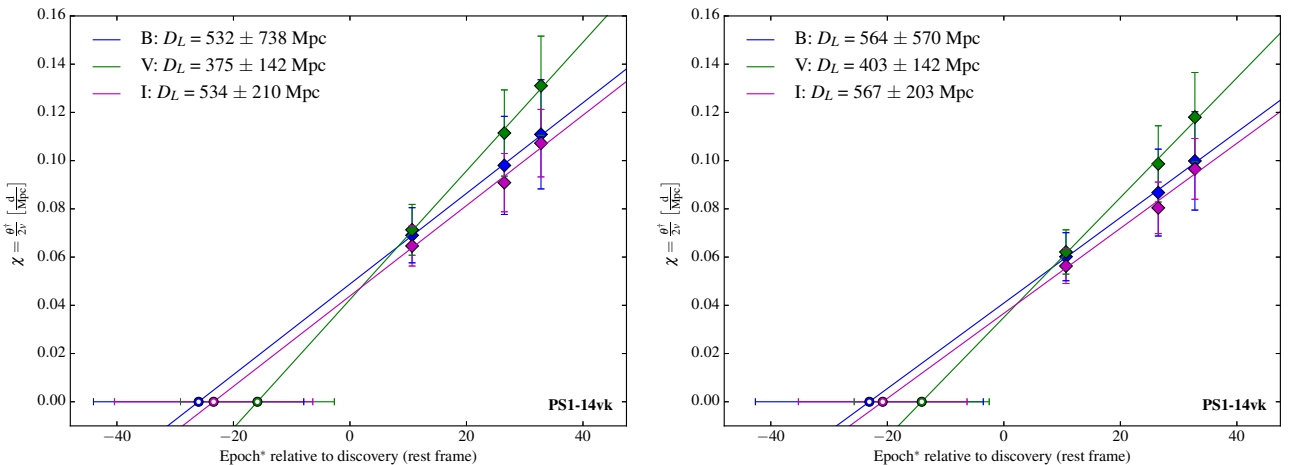


Fig. 5: Distance fit for PS1-14vk using only those epochs that follow a linear relation and ζ_{BVI} as given in Hamuy et al. (2001) (left panel) and Dessart & Hillier (2005) (right panel). The diamond markers denote values of χ through which the fit is made.

3.5.2. SN 2013eq

SN 2013eq is presented in detail in Gall et al. (2016). Using the dilution factors from Hamuy et al. (2001), Gall et al. (2016) found a luminosity distance of $D_L = 151 \pm 18 \text{ Mpc}$ and an explosion time of 4.1 ± 4.4 days before discovery (rest frame), corresponding to a t_0^\diamond of MJD 56499.6 ± 4.6 (observer frame). Applying the dilution factors from Dessart & Hillier (2005) they found $D_L = 164 \pm 20 \text{ Mpc}$ and an explosion time of 3.1 ± 4.1 days before discovery (rest frame) corresponding to a t_0^\diamond of MJD 56500.7 ± 4.3 (observer frame).

3.5.3. SN 2013ca

For SN 2013ca good quality spectroscopy is available allowing us to determine the photospheric velocity directly from the $\text{Fe II } \lambda 5169$ line. Unfortunately, the photometric coverage is less exhaustive, with only 2 points observed in each of the LT $g'r'i'$ filters. The flux at the epochs of spectroscopic observations was linearly interpolated through those two data points. This should be a reasonable assumption for a Type II-P SN during the plateau phase.

3.5.4. LSQ13cuw (SN II-L)

LSQ13cuw photometry as well as spectroscopy was adopted from Gall et al. (2015). They constrain the epoch of explosion to MJD 56593.4 ± 0.7 . This was used as a further data point in the distance fit and provides a more accurate result. Unfortunately, lines of $\text{Fe II } \lambda 5169$ are not visible in any of the LSQ13cuw spectra and we applied the $v_{\text{H}\beta}/v_{\text{Fe} 5169}$ ratio to estimate the photospheric velocities.

However, the spectra of LSQ13cuw are characterised by $\text{H}\alpha$ and $\text{H}\beta$ features that show almost no absorption component, which makes a velocity determination difficult. We were only able to confidently measure the $\text{H}\beta$ velocity from the +32 d spectrum on. However, as outlined in Section 3.4.2 the $v_{\text{H}\beta} - v_{\text{Fe} 5169}$ relation is not reliable after ~ 30 days from explosion. This leaves us with only one estimate for the photospheric velocity from the +32 d spectrum.

3.5.5. PS1-13wr

The reasonably high signal-to-noise spectra of PS1-13wr allow us to determine the photospheric velocity directly from the

Fe II $\lambda 5169$ line. The errors in the distance determination of PS1-13wr are larger than for the other SNe in our sample due to the uncertainty of the dust extinction within its host galaxy (Table 1).

3.5.6. PS1-14vk (SN II-L)

For PS1-14vk, we were able to determine the photospheric velocity directly from the Fe II $\lambda 5169$ line for all epochs, except ~ 2 d and ~ 14 d post-discovery, where the line was either not visible, or blended.

As mentioned previously (see Section 3.5.1) the values of χ in PS1-14vk for the epochs +11, +27, and +33 d follow a clearly linear relation in contrast to the last epoch at +49 d after discovery. This is the case independently of whether we apply the dilution factors given by Hamuy et al. (2001) or Dessart & Hillier (2005). Consequently, we performed fits only through χ values at +11, +27, and +33 d (for both sets of dilution factors by Hamuy et al. (2001) or Dessart & Hillier (2005)). Whenever referring to the distance and explosion epoch results of SN 2014vk, we will be using the latter fit.

3.5.7. PS1-12bku

We are able to identify the Fe II $\lambda 5169$ line in the PS1-12bku spectra and use it to estimate the photospheric velocity. We can additionally constrain the fits by using the estimate for the explosion epoch available for PS1-12bku. This reduces the errors in the distance significantly.

3.5.8. PS1-13abg

For PS1-13abg only relatively poor quality spectra are available and we can identify a Fe II $\lambda 5169$ feature only in the +44 d spectrum. We use this measurement as well as the loose constraint for the explosion epoch to estimate the distance to PS1-13abg.

3.5.9. PS1-13baf

Unfortunately, the spectra of PS1-13baf have a poor signal-to-noise ratio and we are not able to identify Fe II $\lambda 5169$ features in any of the spectra. We apply the $v_{H\beta} - v_{Fe\,5169}$ relation to the first two epochs (i.e. before ~ 30 d), to estimate the photospheric velocities. We were able to additionally constrain the fits by using the estimate for the explosion epoch reducing the error in the distance.

3.5.10. PS1-13bmf (SN II-L)

The spectra of PS1-13bmf at the first two epochs (+5 d and +8 d) are basically featureless. We are therefore able to identify the Fe II $\lambda 5169$ feature only in the later epochs at +29 and +47 d. However, we can additionally constrain the fits by using the estimate for the explosion epoch available for PS1-13bmf (see also Section A.9 in the appendix).

3.5.11. PS1-13atm (SN II-L)

Unfortunately the photometric coverage of PS1-13atm, our second-highest- z SN, is insufficient to perform reliable fits for an estimate of the BVI magnitudes at the epochs of spectroscopic observations with the g_{PS1} - and r_{PS1} -band having only a single

data point each. We therefore forgo an attempt to calculate an EPM distance to PS1-13atm.

3.5.12. PS1-13bni

For PS1-13bni, the Fe II $\lambda 5169$ feature could not be clearly identified at any epoch, so we relied entirely on estimates of the photospheric velocities using the $H\beta$ line (at +15 d and +24 d) and the $v_{H\beta} - v_{Fe\,5169}$ relation. We note that the relation is prone to large uncertainties at epochs $\gtrsim 50$ days post explosion.

Since the $v_{H\beta} - v_{Fe\,5169}$ relation is epoch dependent, but no estimate of an explosion epoch from other sources is available for PS1-13bni, we pursue an iterative approach to derive the time of explosion. For the initial iteration we assume the first detection to be the time of explosion and evaluate the $v_{H\beta} - v_{Fe\,5169}$ relation at the resulting epochs. Then we fit for the distance and the explosion epoch as would be done for any other SN. The derived explosion epoch is then used as a base for the second iteration, and the spectral epochs as well as $v_{H\beta}/v_{Fe\,5169}$ ratios are adjusted accordingly. We repeat this process until the explosion time converges.

3.6. SCM distances

In order to apply the SCM the SN magnitudes have to be converted to the rest frame. We use the V - and I -band K -corrections that were already evaluated for the EPM. These are then interpolated to 50 d after explosion and used to correct the interpolated 50 d photometry.

The expansion velocity is determined using the relation published by Nugent et al. (2006, Equation 2):

$$v_{50} = v(t^*) \left(\frac{t^*}{50} \right)^{0.464 \pm 0.017}, \quad (4)$$

where $v(t^*)$ is the Fe II $\lambda 5169$ velocity at time t^* after explosion (rest frame). For the SNe where we could not identify the Fe II $\lambda 5169$ feature in their spectra we first applied the $v_{H\beta} - v_{Fe\,5169}$ relation and then utilized the derived Fe II $\lambda 5169$ velocities to estimate the expansion velocity at day 50. This procedure was carried out twice for those SNe where estimates of the explosion epoch were available via the EPM (depending on dilution factors).

Finally, we use Equation 1 in Nugent et al. (2006) to derive the distance modulus and thereby the distance:

$$M_{I_{50}} = -\alpha \log_{10} \left(\frac{v_{50,Fe\,II}}{5000} \right) - 1.36 [(V - I)_{50} - (V - I)_0] + M_{I_0}, \quad (5)$$

where M_I is the rest frame I -band magnitude, $(V - I)$ the colour, and v is the expansion velocity each evaluated at 50 days after explosion. The parameters are set as follows: $\alpha = 5.81$, $M_{I_0} = -17.52$ (for an H_0 of $70 \text{ km s}^{-1} \text{ Mpc}^{-1}$) and $(V - I)_0 = 0.53$, following Nugent et al. (2006).

Our results are shown in Table 5. Additionally, we adopt the SCM distances derived by Gall et al. (2016) for SN 203eq: $D_L = 160 \pm 32 \text{ Mpc}$ and $D_L = 157 \pm 31 \text{ Mpc}$, using the explosion epochs calculated via the EPM and utilizing the dilution factors either from Hamuy et al. (2001) or Dessart & Hillier (2005).

The final errors on individual distances span a range between 11 and 35 % depending mainly on whether the explosion epoch is well constrained or not. While the I -band magnitude and the $(V - I)$ colour will not change significantly during the plateau phase of Type II-P SNe and are therefore relatively robust; however, this is not true for the expansion velocity. Any uncertainty

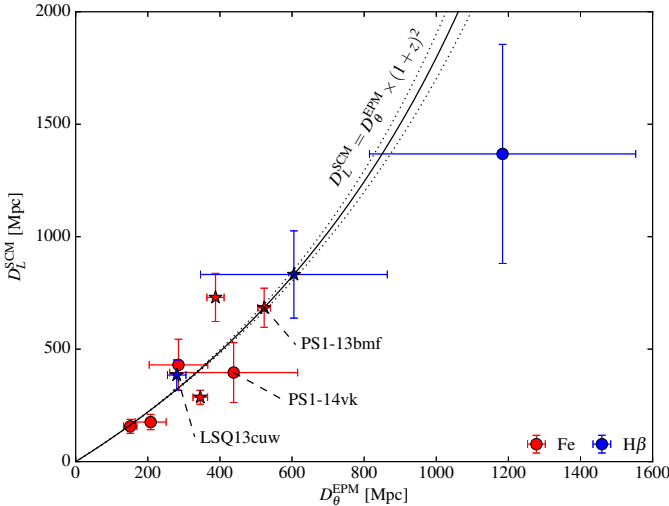


Fig. 6: Comparison of EPM and SCM distances, using the dilution factors by Dessart & Hillier (2005). Filled circles denote SNe for which an estimate of the explosion epoch was obtained via EPM, while the filled stars are for SNe where the explosion epoch was estimated from the photometry. The labelled SNe are the three Type II-L SNe. Different colours denote the line that was used to estimate the photospheric velocities: red corresponds to $\text{Fe II } \lambda 5169$, and dark blue to $\text{H}\beta$. $D_L^{\text{SCM}} = D_E^{\text{EPM}} \times (1 + z)^2$ is shown as a solid line, for a ΛCDM cosmology with $H_0 = 70 \pm 5 \text{ km s}^{-1} \text{ Mpc}^{-1}$, $\Omega_m = 0.3$ and $\Omega_\Lambda = 0.7$.

in the explosion epoch directly translates into an uncertainty in the 50 d velocity and thereby affects the precision of the distance measurement. In our sample this is borne out in the fact that the SCM distances derived using estimates for the explosion epoch from photometry, have significantly smaller relative uncertainties, than those derived using estimates via the EPM.

3.7. Comparison of EPM and SCM distances

Fig. 6 shows the comparison between the EPM and SCM distances for the entire sample. Although there is some scatter, it is reassuring to find overall consistency. Furthermore, there is no obvious trend for one technique to systematically result in longer or shorter distances than the other; a shift would indicate an $H_0 \neq 70 \text{ km s}^{-1} \text{ Mpc}^{-1}$. Similarly, there appears to be no obvious systematic shift amongst the SNe (in red) for which the EPM and SCM distances were derived using the $\text{Fe II } \lambda 5169$ line as an estimator for the photospheric velocity.

3.8. The Hubble diagram

Figure 7 shows the Hubble diagrams using EPM and SCM distances, respectively. The red and blue points represent SNe from our sample for which either $\text{Fe II } \lambda 5169$ or $\text{H}\beta$ was used to estimate the photospheric velocities. For reasons of better visibility we only depict our distance results using the Dessart & Hillier (2005) dilution factors, which give somewhat larger distances than the Hamuy et al. (2001) dilution factors. Our conclusions are the same regardless of which set of dilution factors is used. The grey points depict SNe from other samples. The solid line in both panels represents a ΛCDM cosmology with $H_0 =$

$70 \text{ km s}^{-1} \text{ Mpc}^{-1}$, $\Omega_m = 0.3$ and $\Omega_\Lambda = 0.7$.⁸ We do not aim to perform a fit for H_0 . The three Type II-L SNe LSQ13cuw, PS1-14vk and PS1-13bm are labeled in both the EPM and the SCM Hubble diagram.

3.8.1. EPM Hubble diagram

In addition to the EPM measurements from our own sample we also included EPM distances from the samples of Eastman et al. (1996, Table 6), Jones et al. (2009, Table 5) and Bose & Kumar (2014, Table 3) in the EPM Hubble diagram (see left panel of Figure 7). These values were adopted as they are, without any correction for potential systematic differences. In the cases of Jones et al. (2009) and Bose & Kumar (2014) we selected the distances given using the Dessart & Hillier (2005) dilution factors. In addition, Bose & Kumar (2014) give alternate results for the SNe 2004et, 2005cs, and 2012aw, for which constraints for the explosion epoch are available. We chose these values rather than the less constrained distance measurements in these three cases. Note that the Jones et al. (2009) sample has SN 1992ba in common with the Eastman et al. (1996) sample and SN 1999gi in common with the Bose & Kumar (2014) sample.

Exploring the EPM Hubble diagram, it is immediately apparent that our measured distances follow the slope of the Hubble line, despite the rather poor quality of the data available for some of our SNe.

3.8.2. SCM Hubble diagram

The SCM Hubble diagram shows the SCM distances derived for our sample alongside SCM measurements from the samples of Poznanski et al. (2009, Table 2), Olivares et al. (2010, Table 8) and D’Andrea et al. (2010, Table 3). The Poznanski et al. (2009) sample contains all objects from the Nugent et al. (2006) sample. We also included those objects that Poznanski et al. (2009) “culled” due to their higher decline rates. These are distinguished by a different symbol in the right panel of Figure 7. We applied no corrections for systematic differences or different parameters used in the various samples. D’Andrea et al. (2010) do not give the distance measurements directly but rather their derived values for the I -band magnitude, the $(V - I)$ -colour and the velocity 50 days after explosion (rest frame). We used these to apply the same equation and parameters from Nugent et al. (2006) as for our own sample, to find the distances to these objects. Note that the Poznanski et al. (2009) and Olivares et al. (2010) samples have a number of SNe in common: SNe 1991al, 1992af, 1992ba, 1999br, 1999cr, 1999em, 1999gi, 2003hl, 2003iq, and 2004et.

Our SCM distances scatter around the $H_0 = 70 \text{ km s}^{-1} \text{ Mpc}^{-1}$ line, which of course is no surprise considering that the SCM is based on a previously chosen value of H_0 (in our case $H_0 = 70 \text{ km s}^{-1} \text{ Mpc}^{-1}$ following Nugent et al. 2006).

Interestingly, there seems to be no obvious difference regarding scatter between those SNe for which an estimate of the explosion epoch was available through the SN photometry or those that rely on an EPM estimate for the time of explosion. This implies either that the epochs of explosion derived via the EPM are relatively accurate, or that constraints on the explosion epoch of only a few days, are not relevant for precise SCM measurements.

⁸ The choice of $H_0 = 70 \text{ km s}^{-1} \text{ Mpc}^{-1}$ is rather arbitrary and adopted mainly for consistency with the SCM parameters suggested by Nugent et al. (2006). The general principles and our conclusions are the same, notwithstanding the exact choice of H_0 .

Table 5: SCM quantities and distances

SN	Estimate of t_0 via	t_0^* mjd	V_{50}^* mag	I_{50}^* mag	v_{50} km s $^{-1}$	Estimate of velocity via	μ mag	D_L Mpc
SN 2013ca	EPM – H01	56382.3 $^{+9.7}_{-10.1}$	19.08 \pm 0.10	18.56 \pm 0.08	5427 \pm 798	Fe II λ 5169	36.28 \pm 0.43	180 \pm 36
	EPM – D05	56386.1 $^{+5.9}_{-9.4}$	19.12 \pm 0.10	18.59 \pm 0.08	5228 \pm 758		36.22 \pm 0.42	176 \pm 34
LSQ13cuw	G15	56593.4 \pm 0.7	20.61 \pm 0.10	20.00 \pm 0.09	5616 \pm 655	$H\beta$	37.93 \pm 0.38	385 \pm 67
	EPM – H01	56330.5 \pm 12.5	21.38 \pm 0.06	20.49 \pm 0.07	4458 \pm 963		38.21 \pm 0.57	438 \pm 115
PS1-13wr	EPM – D05	56332.2 \pm 12.1	21.39 \pm 0.06	20.49 \pm 0.07	4368 \pm 959	Fe II λ 5169	38.17 \pm 0.58	430 \pm 114
	EPM – H01	56717.0 \pm 10.1	20.95 \pm 0.29	20.63 \pm 0.24	5228 \pm 818		37.98 \pm 0.75	394 \pm 136
PS1-14vk	EPM – D05	56719.6 \pm 9.7	21.02 \pm 0.27	20.68 \pm 0.23	5093 \pm 816	Fe II λ 5169	37.99 \pm 0.73	396 \pm 133
	PS1	56160.9 \pm 0.4	20.70 \pm 0.07	20.18 \pm 0.06	4258 \pm 291		37.28 \pm 0.23	286 \pm 31
PS1-12bku	PS1	56375.4 \pm 5.0	22.27 \pm 0.08	21.12 \pm 0.09	4672 \pm 438	Fe II λ 5169	39.32 \pm 0.32	730 \pm 107
PS1-13abg	PS1	56408.0 \pm 1.5	23.06 \pm 0.22	22.38 \pm 0.12	4093 \pm 473	$H\beta$	39.60 \pm 0.51	832 \pm 194
PS1-13bmf	PS1	56420.0 \pm 0.1	22.51 \pm 0.06	21.92 \pm 0.11	4363 \pm 256	Fe II λ 5169	39.18 \pm 0.28	684 \pm 87
PS1-13bni	EPM – H01	56401.3 \pm 7.9	23.39 \pm 0.26	23.18 \pm 0.20	5814 \pm 1175	$H\beta$	40.65 \pm 0.76	1348 \pm 470
	EPM – D05	56400.0 \pm 8.6	23.39 \pm 0.26	23.19 \pm 0.20	5913 \pm 1237		40.68 \pm 0.77	1368 \pm 487

* K -corrected magnitudes in the Johnson-Cousins Filter System. H01: Hamuy et al. (2001); D05: Dessart & Hillier (2005).

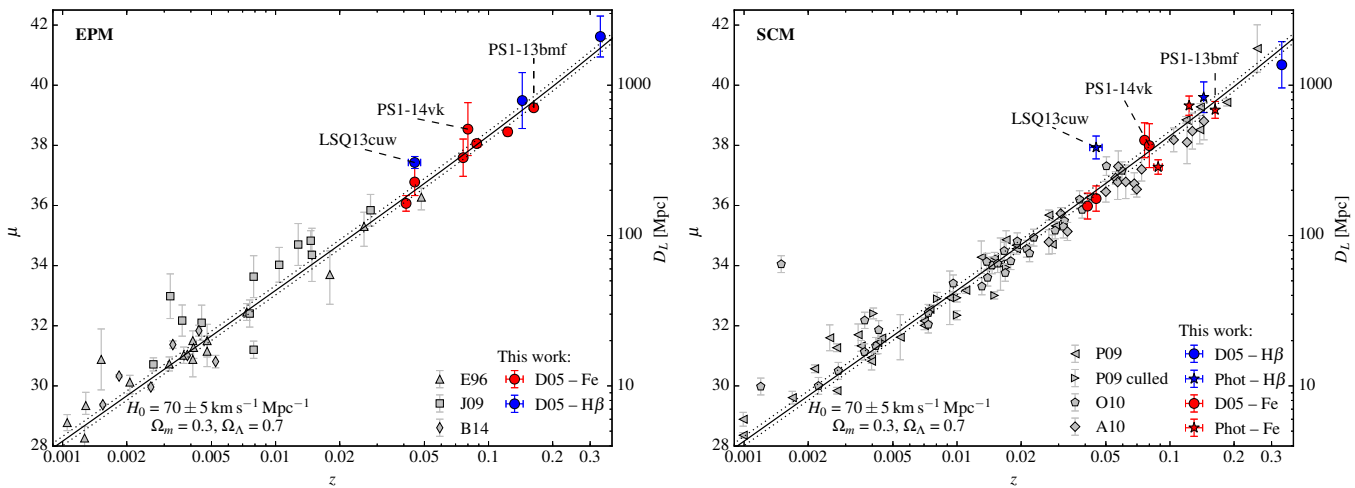


Fig. 7: SN II Hubble diagram using the distances determined via the EPM (left panel) and the SCM (right panel). EPM Hubble diagram (left): the distances derived for our sample (circles) use the dilution factors published by Dessart & Hillier (2005). The labelled SNe represent the three Type II-L SNe in our sample. The different colours (red/blue) denote the line that was used to estimate the photospheric velocities of the particular SN (Fe II λ 5169 or $H\beta$). We also included EPM measurements from the samples of Eastman et al. (1996, E96), Jones et al. (2009, J09) and Bose & Kumar (2014, B14). The solid line corresponds to a Λ CDM cosmology with $H_0 = 70$ km s $^{-1}$ Mpc $^{-1}$, $\Omega_m = 0.3$ and $\Omega_\Lambda = 0.7$, and the dotted lines to the range covered by an uncertainty of 5 km s $^{-1}$ Mpc $^{-1}$. SCM Hubble diagram (right): circle markers depict the SCM distances derived for our sample using the explosion epochs previously derived via the EPM and applying the dilution factors published in Dessart & Hillier (2005). The star shaped markers depict those SNe for which an independent estimate of the explosion time was available via photometry. The labelled SNe represent the three Type II-L SNe in our sample. The colours are coded in the same way as for the EPM Hubble diagram. Similarly, the solid and dotted lines portray the same relation between redshift and distance modulus as in the left panel. We also included SCM measurements from the samples of Poznanski et al. (2009, P09, which includes all objects from the Nugent et al. (2006) sample), Olivares et al. (2010, O10) and D’Andrea et al. (2010, A10). We separated the objects “culled” by Poznanski et al. (2009) from the rest of the sample by using a different symbol. The three Type II-L SNe LSQ13cuw, PS1-14vk and PS1-13bmf are identified in both the EPM and the SCM Hubble diagram.

3.8.3. PS1-13bni

Finally, we would like to point out that our distance measurements to PS1-13bni (at a redshift of $z = 0.335^{+0.009}_{-0.012}$) demonstrates that both the EPM and the SCM bear great potential for cosmology. This statement is, however, slightly tainted by the relatively large uncertainties in the decline rates of PS1-13bni, i.e. the implication that PS1-13bni could, in fact, be a Type II-L SN and the open question whether these can be used as distance indicators.

3.9. Applying the EPM and SCM to Type II-L SNe

When considering the use of SNe II-L for cosmology, a few peculiarities have to be taken into account. As discussed in Section 3.4.3 it is unclear whether SNe II-L display the same velocity evolution as SNe II-P and hence whether the $v_{H_0}/v_{Fe\lambda 5169}$ and $v_{H\beta}/v_{Fe\lambda 5169}$ ratios evolve in the same way for SNe II-L and SNe II-P. For the EPM the additional question arises whether the relation between χ and t^* on which the EPM is based is linear also for SNe II-L (see Equation 3). The case of PS1-14vk indicates

that this linear relation might be valid for a similar period of time as for SNe II-P (see Section 3.5.1).

Furthermore, SNe II-L – as indicated by their name – decline linearly, and therefore become fainter (and for high- z SNe potentially undetectable) faster than SNe II-P that retain a roughly constant luminosity throughout their plateau phase. However, on average, SNe II-L are also brighter and can potentially compensate this defect. Gall et al. (2015) suggest that SNe II-L might have slightly longer rise times than SNe II-P. This could somewhat facilitate obtaining pre-maximum data, thereby resulting in a better constraint on the explosion epoch, the error on which is a contributes significantly to the total error budget.

The three Type II-L SNe in our sample, LSQ13cuw, PS1-14vk, and PS1-13bmf, are indistinguishable from the rest of the sample, in both the EPM and the SCM Hubble diagrams. Although our sample is admittedly small, and definitive statements cannot be made, our results indicate that including SNe II-L would allow for a more efficient way of building up sample sizes. We emphasize that there is no clear observational distinction between the SNe II-P and II-L classes (see e.g. Anderson et al. 2014; Gall et al. 2015), nor is one expected on theoretical grounds. Therefore, testing the validity of Type II-P SN relations, like the χ - t^* relation in the EPM, or the velocity-luminosity correlation for the SCM for SNe with a variety of decline rates, will help to better understand the sources of systematic uncertainties for both techniques.

4. Conclusions

We presented optical light curves and spectra of nine Type II-P/L SNe with redshifts between $z = 0.045$ and $z = 0.335$: SN 2013ca, PS1-13wr, PS1-14vk, PS1-12bku, PS1-13abg, PS1-13baf, PS1-13bmf, PS1-13atm and PS1-13bni. To this sample, we added the Type II-P SN 2013eq (Gall et al. 2016, $z = 0.041 \pm 0.001$) and the Type II-L SN LSQ13cuw (Gall et al. 2015, $z = 0.045 \pm 0.003$), and utilized the expanding photosphere method as well as the standardized candle method to derive the distances to the respective SNe.

We followed the procedures presented in Gall et al. (2016) for the EPM at cosmologically significant redshifts and the approach of Nugent et al. (2006) for the SCM.

We additionally explored the possibility of estimating the photospheric velocities in Type II-P/L SNe using alternative lines ($H\alpha$ and $H\beta$) and used five well observed SNe from the literature (SNe 1999gi, 1999em, 2004et, 2005cs, and 2006bp) to calculate an epoch dependent relation between the $H\alpha$ and $Fe\text{ II } \lambda 5169$ velocity as well as between the $H\beta$ and $Fe\text{ II } \lambda 5169$ velocity.

We found that the $v_{H\alpha}/v_{Fe\text{ II } 5169}$ and $v_{H\beta}/v_{Fe\text{ II } 5169}$ ratios are in good agreement for five well-observed SNe at early epochs, i.e. before ~ 40 days after explosion for $H\alpha$ and ~ 30 days after explosion for $H\beta$ (within 4–14%). Thereafter the $v_{H\alpha}/v_{Fe\text{ II } 5169}$ and $v_{H\beta}/v_{Fe\text{ II } 5169}$ ratios for individual SNe diverge significantly.

For the utilization in the EPM and the SCM we used the $Fe\text{ II } \lambda 5169$ line as an estimator of the photospheric velocity where ever possible. In cases where no $Fe\text{ II } \lambda 5169$ feature could be identified in the SN spectra we applied the $v_{H\beta} - v_{Fe\text{ II } 5169}$ relation to obtain an estimate for the velocity. The possibility to use alternate lines to iron will not only be of use for SNe of very distant galaxies, but can also be applied to nearby samples.

In general, our EPM and SCM distances are in good agreement with the distances we would expect from the redshifts of the respective host galaxies, using standard Λ CDM cosmology. This is especially encouraging given the necessarily discrepant

quality of the available datasets for local versus intermediate- or high-redshift objects. Comparable precision to other distance indicators can feasibly be achieved via larger samples and higher quality data of Type II SNe. Upcoming future facilities – such as the LSST – will pave the way forward.

The case of PS1-13bni at a redshift of $z = 0.335^{+0.009}_{-0.012}$ is the highest- z SN II for which a distance measurement was ever attempted, further demonstrating the potential of the EPM and SCM for cosmological applications.

Finally, we evaluated the implications of using Type II-L SNe for cosmology. Our sample contains three Type II-L SNe. These yield similar distances compared to the SNe II-P in our sample. It appears that including SNe II-L would allow for larger samples to be considered. However, we note that that further investigations on the differences and similarities between SNe II-L and II-P are necessary to robustly assess the systematics.

Acknowledgements

Based in part on observations made with the Gran Telescopio Canarias (GTC2007-12ESO, ESO program ID: 189.D-2007, PI:RK), installed in the Spanish Observatorio del Roque de los Muchachos of the Instituto de Astrofísica de Canarias, on the island of La Palma.

EEEG, BL, ST, and WH acknowledge support for this work by the Deutsche Forschungsgemeinschaft through the TransRegio project TRR33 ‘The Dark Universe’. R.K. acknowledges funding from STFC (ST/L000709/1). N.M. acknowledges support from the Science and Technology Facilities Council [ST/L00075X/1].

Based in part on observations obtained at the Liverpool Telescope (program ID: XIL10B01, PI:RK), operated on the island of La Palma by Liverpool John Moores University in the Spanish Observatorio del Roque de los Muchachos of the Instituto de Astrofísica de Canarias with financial support from the UK Science and Technology Facilities Council.

Based in part on observations obtained at the Nordic Optical Telescope, operated by the Nordic Optical Telescope Scientific Association at the Observatorio del Roque de los Muchachos, La Palma, Spain, of the Instituto de Astrofísica de Canarias.

This research has made use of the NASA/IPAC Extragalactic Database (NED) which is operated by the Jet Propulsion Laboratory, California Institute of Technology, under contract with the National Aeronautics and Space Administration.

The Pan-STARRS1 Surveys (PS1) have been made possible through contributions of the Institute for Astronomy, the University of Hawaii, the Pan-STARRS Project Office, the Max-Planck Society and its participating institutes, the Max Planck Institute for Astronomy, Heidelberg and the Max Planck Institute for Extraterrestrial Physics, Garching, The Johns Hopkins University, Durham University, the University of Edinburgh, Queen’s University Belfast, the Harvard-Smithsonian Center for Astrophysics, the Las Cumbres Observatory Global Telescope Network Incorporated, the National Central University of Taiwan, the Space Telescope Science Institute, the National Aeronautics and Space Administration under Grant No. NNX08AR22G issued through the Planetary Science Division of the NASA Science Mission Directorate, the National Science Foundation under Grant No. AST-1238877, the University of Maryland, and Eotvos Lorand University (ELTE) and the Los Alamos National Laboratory.

Funding for the Sloan Digital Sky Survey (SDSS) and SDSS-II has been provided by the Alfred P. Sloan Foundation, the Participating Institutions, the National Science Foundation, the

U.S. Department of Energy, the National Aeronautics and Space Administration, the Japanese Monbukagakusho, the Max Planck Society, and the Higher Education Funding Council for England. The SDSS Web Site is <http://www.sdss.org/>.

The SDSS is managed by the Astrophysical Research Consortium for the Participating Institutions. The Participating Institutions are the American Museum of Natural History, Astrophysical Institute Potsdam, University of Basel, University of Cambridge, Case Western Reserve University, University of Chicago, Drexel University, Fermilab, the Institute for Advanced Study, the Japan Participation Group, Johns Hopkins University, the Joint Institute for Nuclear Astrophysics, the Kavli Institute for Particle Astrophysics and Cosmology, the Korean Scientist Group, the Chinese Academy of Sciences (LAMOST), Los Alamos National Laboratory, the Max-Planck-Institute for Astronomy (MPIA), the Max-Planck-Institute for Astrophysics (MPA), New Mexico State University, Ohio State University, University of Pittsburgh, University of Portsmouth, Princeton University, the United States Naval Observatory, and the University of Washington.

References

Anderson, J. P., González-Gaitán, S., Hamuy, M., et al. 2014, *ApJ*, 786, 67
 Baltay, C., Rabinowitz, D., Hadjyska, E., et al. 2013, *PASP*, 125, 683
 Bennett, C. L., Larson, D., Weiland, J. L., & Hinshaw, G. 2014, *ApJ*, 794, 135
 Blondin, S. & Tonry, J. L. 2007, *ApJ*, 666, 1024
 Bose, S. & Kumar, B. 2014, *ApJ*, 782, 98
 D'Andrea, C. B., Sako, M., Dilday, B., et al. 2010, *ApJ*, 708, 661
 Dessart, L. & Hillier, D. J. 2005, *A&A*, 439, 671
 Eastman, R. G., Schmidt, B. P., & Kirshner, R. 1996, *ApJ*, 466, 911
 Fiorentino, G., Musella, I., & Marconi, M. 2013, *MNRAS*, 434, 2866
 Freedman, W. L., Madore, B. F., Gibson, B. K., et al. 2001, *ApJ*, 553, 47
 Freedman, W. L., Madore, B. F., Mould, J. R., et al. 1994, *Nature*, 371, 757
 Gall, E. E. E., Kotak, R., Leibundgut, B., et al. 2016, ArXiv e-prints
 Gall, E. E. E., Polshaw, J., Kotak, R., et al. 2015, *A&A*, 582, A3
 Gonzalez-Gaitan, S., Tominaga, N., Molina, J., et al. 2015, ArXiv:1505.02988
 Gutiérrez, C. P., Anderson, J. P., Hamuy, M., et al. 2014, *ApJ*, 786, L15
 Hamuy, M. & Pinto, P. A. 2002, *ApJ*, 566, L63
 Hamuy, M., Pinto, P. A., Maza, J., et al. 2001, *ApJ*, 558, 615
 Humphreys, E. M. L., Reid, M. J., Moran, J. M., Greenhill, L. J., & Argon, A. L. 2013, *ApJ*, 775, 13
 Inserra, C., Smartt, S. J., Gall, E. E. E., et al. 2016, ArXiv e-prints
 Jones, M. I., Hamuy, M., Lira, P., et al. 2009, *ApJ*, 696, 1176
 Kaiser, N., Burgett, W., Chambers, K., et al. 2010, in Society of Photo-Optical Instrumentation Engineers (SPIE) Conference Series, Vol. 7733, Society of Photo-Optical Instrumentation Engineers (SPIE) Conference Series, 0
 Kirshner, R. P. & Kwan, J. 1974, *ApJ*, 193, 27
 Landolt, A. U. 1992, *AJ*, 104, 340
 Leonard, D. C. 2002, *PASP*, 114, 1291
 Leonard, D. C., Filippenko, A. V., Gates, E. L., et al. 2002a, *PASP*, 114, 35
 Leonard, D. C., Filippenko, A. V., Li, W., et al. 2002b, *AJ*, 124, 2490
 Li, W., Leaman, J., Chornock, R., et al. 2011, *MNRAS*, 412, 1441
 Lilly, S. J., Le Fèvre, O., Renzini, A., et al. 2007, *ApJS*, 172, 70
 Magnier, E. 2006, in The Advanced Maui Optical and Space Surveillance Technologies Conference, 50
 Nugent, P., Sullivan, M., Ellis, R., et al. 2006, *ApJ*, 645, 841
 Olivares, E. F., Hamuy, M., Pignata, G., et al. 2010, *ApJ*, 715, 833
 Pastorello, A., Sauer, D., Taubenberger, S., et al. 2006, *MNRAS*, 370, 1752
 Pastorello, A., Valenti, S., Zampieri, L., et al. 2009, *MNRAS*, 394, 2266
 Perlmutter, S., Aldering, G., Goldhaber, G., et al. 1999, *ApJ*, 517, 565
 Planck Collaboration XIII. 2015, ArXiv e-prints
 Polshaw, J., Kotak, R., Chambers, K. C., et al. 2015, *A&A*, 580, L15
 Poznanski, D., Butler, N., Filippenko, A. V., et al. 2009, *ApJ*, 694, 1067
 Poznanski, D., Nugent, P. E., & Filippenko, A. V. 2010, *ApJ*, 721, 956
 Poznanski, D., Prochaska, J. X., & Bloom, J. S. 2012, *MNRAS*, 426, 1465
 Quimby, R. M., Wheeler, J. C., Höflich, P., et al. 2007, *ApJ*, 666, 1093
 Riess, A. G., Filippenko, A. V., Challis, P., et al. 1998, *AJ*, 116, 1009
 Riess, A. G., Macri, L., Casertano, S., et al. 2011a, *ApJ*, 732, 129
 Riess, A. G., Macri, L., Casertano, S., et al. 2011b, *ApJ*, 730, 119
 Riess, A. G., Macri, L. M., Hoffmann, S. L., et al. 2016, *ApJ*, 826, 56
 Sahu, D. K., Anupama, G. C., Srividya, S., & Muneer, S. 2006, *MNRAS*, 372, 1315
 Schlafly, E. F. & Finkbeiner, D. P. 2011, *ApJ*, 737, 103
 Schmidt, B. P., Kirshner, R. P., Eastman, R. G., et al. 1994a, *AJ*, 107, 1444
 Schmidt, B. P., Kirshner, R. P., Eastman, R. G., et al. 1994b, *ApJ*, 432, 42
 Tonry, J. L., Stubbs, C. W., Lykke, K. R., et al. 2012, *ApJ*, 750, 99
 Wagoner, R. V. 1981, *ApJ*, 250, L65
 Walker, E. S., Hadjyska, E., Rabinowitz, D., et al. 2013, *The Astronomer's Telegram*, 5056, 1
 Zhang, K., Wang, X., Zhou, L., et al. 2013, *Central Bureau Electronic Telegrams*, 3508, 1

Appendix A: Photometric and spectroscopic observations of the individual SNe

An overview of our sample and the SN properties is given in Section 2, Table 1. In the following we present a description of the observations for each individual SN.

Appendix A.1: SN 2013eq

Photometric data up to 76 days after discovery (rest frame) as well as a series of five spectra ranging from 7 to 65 days after discovery (rest frame) for SN 2013eq are presented in Gall et al. (2016). They find a redshift of $z = 0.041 \pm 0.001$, a host galaxy extinction of $E(B-V)_{\text{host}} = 0.062 \pm 0.028$ mag and a Galactic extinction of $E(B-V)_{\text{Gal}} = 0.034$ mag from Schlafly & Finkbeiner (2011). We adopt these values also for this study.

Appendix A.2: SN 2013ca

SN 2013ca was discovered on 2013 April 21 as “LSQ13aco” by the La Silla Quest Supernova Survey (LSQ; Baltay et al. 2013), and spectroscopically classified as a Type II-P SN (Walker et al. 2013). It was independently discovered on 2013 May 1 and likewise classified as a Type II-P SN by Zhang et al. (2013), who also report further detections on 2013 April 10 and May 3.

We obtained LT $g'r'i'$ photometry 41 and 68 days (rest frame) after the first detection and a series of four GTC spectra ranging between +30 and +60 d (rest frame) after the first detection.

In order to determine the redshift of SN 2013ca we extracted host galaxy spectra alongside the SN spectra at all epochs and measured the redshift of the narrow H_{α} emission line. Averaging over all epochs results in a redshift of 0.045 ± 0.001 which was adopted for SN 2013ca.

Features attributable to the Na I doublet from interstellar gas either in the Milky Way or the host galaxy, are not apparent in the spectra of SN 2013ca. In order to derive an upper limit to the equivalent width (EW) of a putative Na I D absorption feature, we constructed a weighted stack of all SN 2013ca spectra, where the weights reflect the signal-to-noise ratio in the 6900–7100 Å region. We then created a series of artificial Gaussian profiles centered at 5893 Å and subtracted these from the stacked spectrum. The FWHM of the Gaussian profiles was set to 17.0 Å, which corresponds to our lowest resolution spectrum. We increased the EW of the artificial profile in steps of 0.1 Å in order to determine the limiting EW at which an artificial line profile as described above would be just detectable in the stacked spectrum. Using this method we derive the upper limit for the EW of the $\text{Na I D } \lambda\lambda 5890, 5896$ blend to be < 0.4 Å. Applying the relation in Equation 9 of Poznanski et al. (2012), we find $E(B-V)_{\text{host}} < 0.04$ mag.

The light curves of SN 2013eq are presented in the left panel of Figure A.1. Table A.1 shows the log of imaging observations as well as the final calibrated magnitudes. Unfortunately the photometric coverage of SN 2013ca is relatively sparse. Using the two available data points in the r' -band we find a decline rate of 0.34 ± 0.18 mag/50 d, which is below the threshold of 0.5 mag/50 d set by Li et al. (2011) to distinguish SNe II-P from SNe II-L.

Table A.2 gives the journal of spectroscopic observations for SN 2013ca. The fully reduced and calibrated spectra of SN 2013ca are presented in the right panel of Figure A.1. They are corrected for galactic reddening and redshift ($z = 0.045$). The

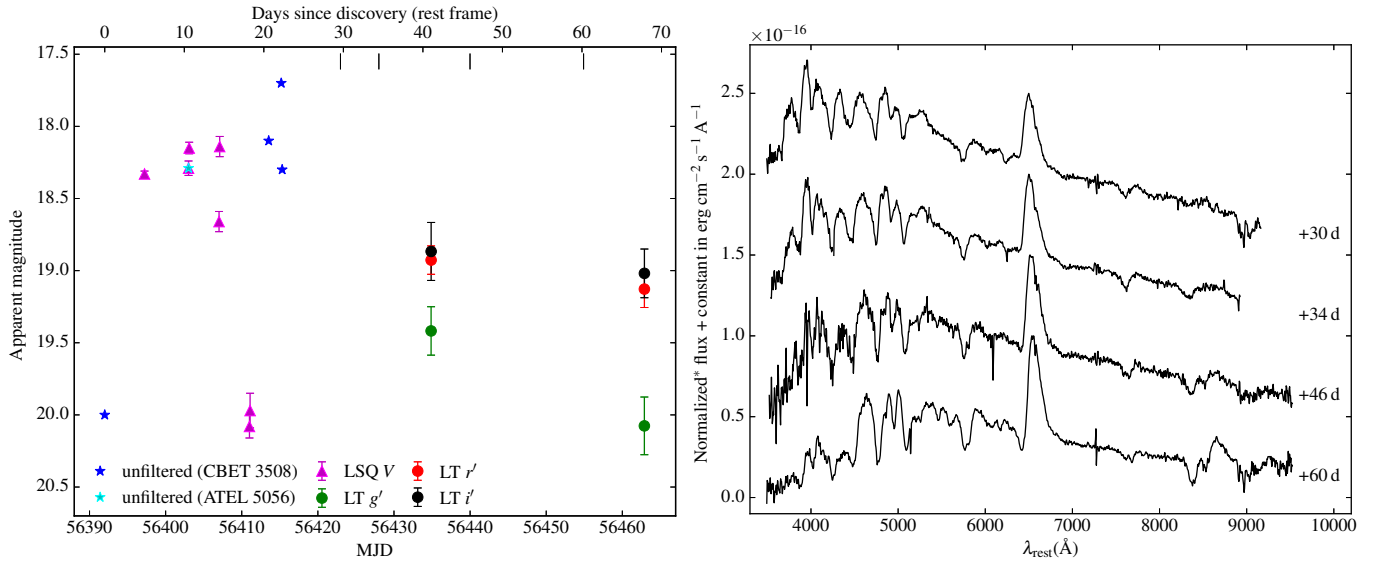


Fig. A.1: SN 2013ca. Left panel: LT $g'r'i'$ and LSQ V light curves of SN 2013ca. The vertical ticks on the top mark the epochs of the observed spectra. ATel 5056: Walker et al. (2013); CBET 3508: Zhang et al. (2013). Right panel: SN 2013ca spectroscopy. *Flux normalized to the maximum $H\alpha$ flux for better visibility of the features. The exact normalizations are: flux/1.3 for the +30 d spectrum; flux/1.4 for +34 d; flux/1.5 for +46 d; flux/1.5 for +60 d.

Table A.1: SN 2013ca: Photometric observations

Date	MJD	Rest frame epoch*	Magnitude	Filter	Telescope
2013-05-22	56434.88	+41.03	19.42 ± 0.17	g'	LT
2013-06-19	56462.90	+67.84	20.08 ± 0.20	g'	LT
2013-05-22	56434.88	+41.03	18.93 ± 0.10	r'	LT
2013-06-19	56462.90	+67.85	19.13 ± 0.13	r'	LT
2013-05-22	56434.88	+41.04	18.87 ± 0.20	i'	LT
2013-06-19	56462.90	+67.85	19.02 ± 0.17	i'	LT

The tabulated magnitudes are given “as observed”, i.e. neither corrected for dust extinction nor K -corrected. *Rest frame epochs (assuming a redshift of 0.045) with respect to the first detection on 56392.0 (MJD). LT = Liverpool Telescope.

spectra display the typical features of $H\alpha$ and $H\beta$. The $H\alpha$ line shows only a very small absorption in the +30 and +34 d spectra, which then becomes more prominent from +46 d on. We can also discern weak lines of iron, in particular $Fe\text{ II } \lambda 5169$ which is visible in all four spectra.

Appendix A.3: LSQ13cuw

Photometric data up to 100 days after discovery (rest frame) as well as a series of 5 spectra ranging from 25 to 84 days after discovery (rest frame) for LSQ13cuw are presented in Gall et al. (2015). Performing a fit to the pre-peak photometry Gall et al. (2015) are able to constrain the epoch of explosion to be MJD 56593.42 ± 0.68 . They find a redshift of $z = 0.045 \pm 0.003$, a host galaxy extinction $E(B - V)_{\text{host}} < 0.16$ mag and a Galactic extinction of $E(B - V)_{\text{Gal}} = 0.023$ mag from Schlafly & Finkbeiner (2011). We adopt these values also for this study.

Appendix A.4: PS1-13wr

PS1-13wr was discovered on 2013 February 26 by the PS1 MD survey. g_{PS1} , r_{PS1} , i_{PS1} , z_{PS1} , y_{PS1} photometry was obtained in the course of the PS1 MD survey up to 150 d (rest frame) after the first detection. We additionally obtained a series of four GTC

spectra ranging between +12 and +41 d (rest frame) after discovery.

PS1-13wr lies close to the galaxy SDSS J141558.95+520302.9 for which the SDSS reports a spectroscopic redshift of 0.076 ± 0.001 . This redshift was adopted also for PS1-13wr and is consistent with the redshift derived from the $Na\text{ I D}$ doublet visible in the spectra of PS1-13wr.

Weak $Na\text{ I D}$ absorptions are visible in the PS1-13wr spectra. In order to obtain an accurate measure of the equivalent width we constructed a weighted stack of all PS1-13wr spectra, where the weights reflect the signal-to-noise ratio in the 5850–6000 Å region. We measure an equivalent width of $EW_{Na\text{ I D}} = 0.76 \pm 0.07$ Å in the stacked PS1-13wr spectrum. Applying the empirical relation between $Na\text{ I D}$ absorption and dust extinction given in Poznanski et al. (2012, Equation 9), this translates into an extinction within the host galaxy of $E(B - V)_{\text{PS1-13wr}}^{\text{host}} = 0.110 \pm 0.049$ mag for PS1-13wr.

The light curves of PS1-13wr are presented in the left panel of Figure A.2. Table A.3 shows the log of imaging observations as well as the final calibrated magnitudes. PS1-13wr shows a distinct plateau in the r_{PS1} , i_{PS1} , z_{PS1} , and y_{PS1} -bands until about 80 d after discovery when it drops onto the radioactive tail. Its r_{PS1} -band decline rate is $\sim 0.20 \pm 0.07$ mag/50 d, characterising it as a II-P SN.

Table A.2: SN 2013ca: Journal of spectroscopic observations

Date	MJD	Epoch* rest frame	Wavelength range in Å	Resolution Å	Telescope+Instrument
2013-05-10	56422.97	+29.63	3650 - 9595	17.0	GTC+OSIRIS+R300B
2013-05-15	56428.02	+34.46	3700 - 9345	16.9	GTC+OSIRIS+R300B
2013-05-27	56439.99	+45.92	3680 - 9970	16.9	GTC+OSIRIS+R300B
2013-06-11	56454.91	+60.20	3650 - 9970	16.8	GTC+OSIRIS+R300B

*Rest frame epochs (assuming a redshift of 0.045) with respect to the first detection on 56392.0 (MJD). The resolution was determined from the FWHM of the $\text{O I } \lambda 5577.34$ sky line.

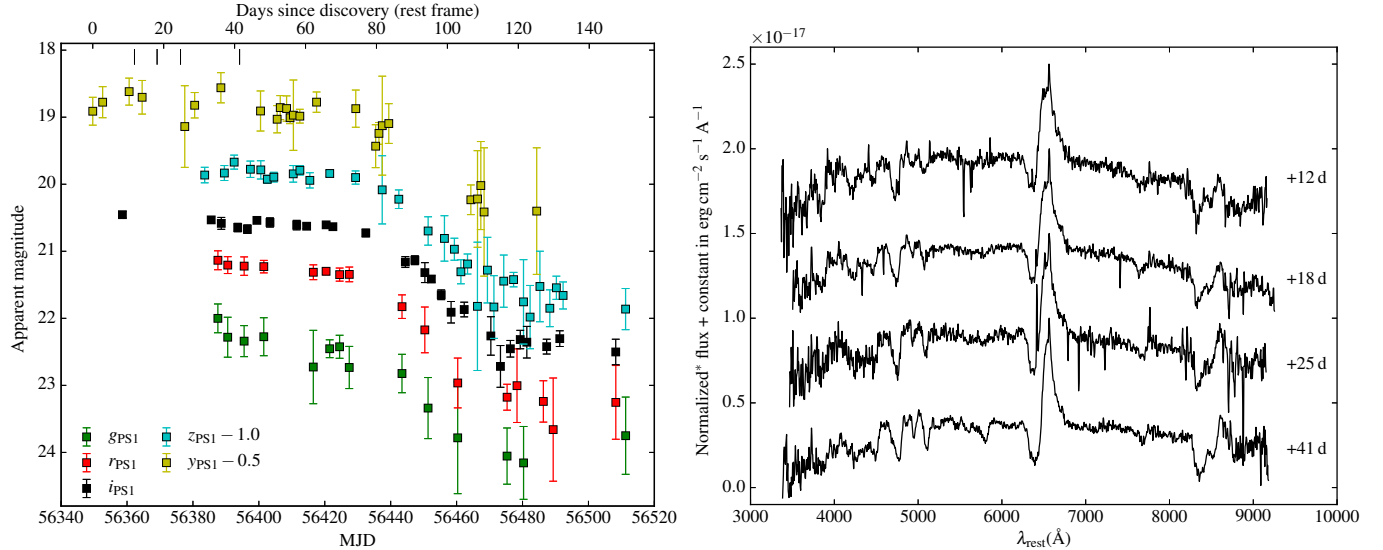


Fig. A.2: PS1-13wr. Left panel: $grizy_{PS1}$ light curves of PS1-13wr. The vertical ticks on the top mark the epochs of the observed spectra. Right panel: PS1-13wr spectroscopy. *Flux normalized to the maximum $\text{H}\alpha$ flux for better visibility of the features. The exact normalizations are: flux/3.4 for the +12 d spectrum; flux/3.5 for +18 d; flux/3.6 for +25 d; flux/3.6 for +41 d.

Table A.4 gives the journal of spectroscopic observations for PS1-13wr. The fully reduced and calibrated spectra of PS1-13wr are presented in the right panel of Figure A.2. They are corrected for galactic and host galaxy reddening as well as redshift ($z = 0.076$). The spectra display the typical features of $\text{H}\alpha$ and $\text{H}\beta$. The $\text{H}\alpha$ lines in all four spectra have a clear P-Cygni profile shape. It additionally displays a narrow component which is likely a contamination from the host galaxy. Weak lines of iron, in particular $\text{Fe II } \lambda 5169$ are visible in all four spectra.

Appendix A.5: PS1-14vk

PS1-14vk was discovered on 2014 March 24 by the PS1 3 π survey. We obtained LT $g'r'i'$ photometry up to 68 d (rest frame) after discovery as well as a series of six GTC spectra ranging between +2 and +49 d (rest frame) after the first detection.

PS1-14vk lies in the vicinity of the galaxy SDSS J121045.27+484143.9 for which the SDSS reports a spectroscopic redshift of 0.080 ± 0.001 , which we adopt also for PS1-14vk.

Features attributable to the Na I doublet from interstellar gas either in the Milky Way or the host galaxy, are not apparent in the spectra of PS1-14vk. Consequently, we derived an upper limit for the equivalent width of the $\text{Na I D } \lambda\lambda 5890, 5896$ blend in the same manner as for SN 2013ca (see Section A.1). We find $\text{EW}_{\text{Na I D}} < 0.7 \text{ Å}$, which translates into a host extinction of $E(B - V)_{\text{host}} < 0.09 \text{ mag}$ (Equation 9 of Poznanski et al. 2012).

The light curves of PS1-14vk are presented in the left panel of Figure A.3. Table A.5 shows the log of imaging observations as well as the final calibrated magnitudes. PS1-14vk declines linearly in the g' -, r' - and i' -band with an averaged decline rate of $1.16 \pm 0.23 \text{ mag/50 d}$ in the r' -band. Consequently, we classify it as a Type II-L SN, following the scheme of Li et al. (2011).

Table A.6 gives the journal of spectroscopic observations for PS1-14vk. The fully reduced and calibrated spectra of PS1-14vk are presented in the right panel of Figure A.3. They are corrected for galactic reddening and redshift ($z = 0.080$). The spectra at all epochs show features of $\text{H}\alpha$ and $\text{H}\beta$. At the earliest epoch the $\text{H}\alpha$ emission is dominated by a narrow component, which is visible at all epochs - though less prominent. We attribute this to contamination by the host galaxy, due to the projected distance of the SN of only $\sim 4.5 \text{ kpc}$ from the center of the host galaxy. $\text{H}\alpha$ displays only a very weak absorption until +14 d after discovery, as is also observed by Gutiérrez et al. (2014) for other SNe II-L. At later epochs the $\text{H}\alpha$ absorption becomes more prominent. Weak lines of iron are not visible in the first spectrum, however a faint line of $\text{Fe II } \lambda 5169$ can be seen in the +11 d and later spectra.

Appendix A.6: PS1-12bku

PS1-12bku was discovered on 2012 August 22 by the PS1 MD survey. $g_{PS1}r_{PS1}i_{PS1}z_{PS1}y_{PS1}$ photometry was obtained in the course of the PS1 MD survey as well as NOT $u'g'r'i'z'$ photometry up to 114 d (rest frame) after the first detection. We addi-

Table A.3: PS1-13wr: Photometric observations

Date	MJD	Rest frame epoch*	Magnitude	Filter	Telescope
2013-04-05	56387.56	+35.28	22.00 ± 0.21	<i>gps1</i>	PS1
2013-04-08	56390.55	+38.05	22.28 ± 0.30	<i>gps1</i>	PS1
2013-04-13	56395.53	+42.68	22.34 ± 0.23	<i>gps1</i>	PS1
2013-04-19	56401.49	+48.22	22.27 ± 0.28	<i>gps1</i>	PS1
2013-05-04	56416.52	+62.19	22.73 ± 0.55	<i>gps1</i>	PS1
2013-05-09	56421.49	+66.81	22.45 ± 0.13	<i>gps1</i>	PS1
2013-05-12	56424.50	+69.60	22.42 ± 0.17	<i>gps1</i>	PS1
2013-05-15	56427.43	+72.33	22.73 ± 0.31	<i>gps1</i>	PS1
2013-05-31	56443.42	+87.19	22.82 ± 0.29	<i>gps1</i>	PS1
2013-06-08	56451.34	+94.55	23.34 ± 0.46	<i>gps1</i>	PS1
2013-06-17	56460.33	+102.90	23.78 ± 0.83	<i>gps1</i>	PS1
2013-07-02	56475.30	+116.82	24.05 ± 0.42	<i>gps1</i>	PS1
2013-07-07	56480.31	+121.48	24.16 ± 0.54	<i>gps1</i>	PS1
2013-08-07	56511.29	+150.27	23.75 ± 0.58	<i>gps1</i>	PS1
2013-04-05	56387.58	+35.29	21.13 ± 0.14	<i>rps1</i>	PS1
2013-04-08	56390.56	+38.06	21.21 ± 0.13	<i>rps1</i>	PS1
2013-04-13	56395.54	+42.69	21.22 ± 0.14	<i>rps1</i>	PS1
2013-04-19	56401.50	+48.24	21.23 ± 0.09	<i>rps1</i>	PS1
2013-05-04	56416.53	+62.20	21.31 ± 0.11	<i>rps1</i>	PS1
2013-05-08	56420.40	+65.79	21.30 ± 0.05	<i>rps1</i>	PS1
2013-05-12	56424.51	+69.62	21.35 ± 0.10	<i>rps1</i>	PS1
2013-05-15	56427.44	+72.34	21.34 ± 0.11	<i>rps1</i>	PS1
2013-05-31	56443.43	+87.20	21.83 ± 0.18	<i>rps1</i>	PS1
2013-06-07	56450.35	+93.63	22.17 ± 0.34	<i>rps1</i>	PS1
2013-06-17	56460.34	+102.91	22.96 ± 0.37	<i>rps1</i>	PS1
2013-07-02	56475.32	+116.84	23.18 ± 0.19	<i>rps1</i>	PS1
2013-07-05	56478.32	+119.63	23.00 ± 0.55	<i>rps1</i>	PS1
2013-07-13	56486.32	+127.06	23.24 ± 0.31	<i>rps1</i>	PS1
2013-07-16	56489.30	+129.83	23.66 ± 0.77	<i>rps1</i>	PS1
2013-08-04	56508.30	+147.49	23.25 ± 0.55	<i>rps1</i>	PS1
2013-03-07	56358.60	+8.36	20.45 ± 0.04	<i>ips1</i>	PS1
2013-04-03	56385.54	+33.40	20.53 ± 0.05	<i>ips1</i>	PS1
2013-04-06	56388.60	+36.24	20.58 ± 0.09	<i>ips1</i>	PS1
2013-04-11	56393.58	+40.87	20.65 ± 0.06	<i>ips1</i>	PS1
2013-04-14	56396.51	+43.60	20.67 ± 0.06	<i>ips1</i>	PS1
2013-04-17	56399.40	+46.28	20.54 ± 0.04	<i>ips1</i>	PS1
2013-04-21	56403.38	+49.98	20.57 ± 0.07	<i>ips1</i>	PS1
2013-04-29	56411.47	+57.50	20.61 ± 0.07	<i>ips1</i>	PS1
2013-05-02	56414.50	+60.31	20.63 ± 0.04	<i>ips1</i>	PS1
2013-05-08	56420.41	+65.81	20.61 ± 0.03	<i>ips1</i>	PS1
2013-05-10	56422.46	+67.71	20.63 ± 0.04	<i>ips1</i>	PS1
2013-05-20	56432.44	+76.99	20.73 ± 0.06	<i>ips1</i>	PS1
2013-06-01	56444.45	+88.15	21.16 ± 0.08	<i>ips1</i>	PS1
2013-06-04	56447.33	+90.83	21.13 ± 0.07	<i>ips1</i>	PS1
2013-06-07	56450.37	+93.65	21.32 ± 0.15	<i>ips1</i>	PS1
2013-06-09	56452.33	+95.47	21.41 ± 0.05	<i>ips1</i>	PS1
2013-06-12	56455.33	+98.26	21.65 ± 0.07	<i>ips1</i>	PS1
2013-06-15	56458.32	+101.04	21.91 ± 0.16	<i>ips1</i>	PS1
2013-06-19	56462.31	+104.74	21.87 ± 0.11	<i>ips1</i>	PS1
2013-06-27	56470.39	+112.25	22.26 ± 0.29	<i>ips1</i>	PS1
2013-06-30	56473.30	+114.96	22.72 ± 0.31	<i>ips1</i>	PS1
2013-07-03	56476.31	+117.76	22.45 ± 0.12	<i>ips1</i>	PS1
2013-07-06	56479.31	+120.55	22.32 ± 0.14	<i>ips1</i>	PS1
2013-07-08	56481.30	+122.40	22.36 ± 0.24	<i>ips1</i>	PS1
2013-07-14	56487.32	+127.99	22.42 ± 0.11	<i>ips1</i>	PS1
2013-07-18	56491.30	+131.69	22.30 ± 0.12	<i>ips1</i>	PS1
2013-08-04	56508.28	+147.47	22.50 ± 0.19	<i>ips1</i>	PS1
2013-04-01	56383.57	+31.56	20.86 ± 0.12	<i>zps1</i>	PS1
2013-04-07	56389.54	+37.11	20.83 ± 0.11	<i>zps1</i>	PS1
2013-04-10	56392.51	+39.88	20.67 ± 0.10	<i>zps1</i>	PS1
2013-04-15	56397.43	+44.45	20.78 ± 0.12	<i>zps1</i>	PS1
2013-04-18	56400.59	+47.38	20.79 ± 0.14	<i>zps1</i>	PS1
2013-04-20	56402.56	+49.22	20.93 ± 0.06	<i>zps1</i>	PS1
2013-04-22	56404.55	+51.06	20.89 ± 0.07	<i>zps1</i>	PS1
2013-04-28	56410.43	+56.54	20.85 ± 0.12	<i>zps1</i>	PS1
2013-04-30	56412.45	+58.41	20.79 ± 0.07	<i>zps1</i>	PS1

Table A.3: (continued)

Date	MJD	Rest frame epoch*	Magnitude	Filter	Telescope
2013-05-03	56415.47	+61.21	20.94 ± 0.11	z_{PS1}	PS1
2013-05-09	56421.50	+66.82	20.84 ± 0.05	z_{PS1}	PS1
2013-05-17	56429.34	+74.11	20.90 ± 0.10	z_{PS1}	PS1
2013-05-25	56437.42	+81.62	21.08 ± 0.51	z_{PS1}	PS1
2013-05-30	56442.46	+86.30	21.22 ± 0.14	z_{PS1}	PS1
2013-06-08	56451.36	+94.57	21.70 ± 0.21	z_{PS1}	PS1
2013-06-13	56456.31	+99.17	21.81 ± 0.34	z_{PS1}	PS1
2013-06-16	56459.32	+101.97	21.97 ± 0.16	z_{PS1}	PS1
2013-06-18	56461.30	+103.81	22.31 ± 0.18	z_{PS1}	PS1
2013-06-20	56463.31	+105.67	22.19 ± 0.15	z_{PS1}	PS1
2013-06-23	56466.32	+108.47	22.82 ± 0.96	z_{PS1}	PS1
2013-06-26	56469.35	+111.29	22.28 ± 0.49	z_{PS1}	PS1
2013-06-28	56471.32	+113.12	22.83 ± 0.47	z_{PS1}	PS1
2013-07-01	56474.30	+115.89	22.45 ± 0.39	z_{PS1}	PS1
2013-07-04	56477.29	+118.67	22.42 ± 0.11	z_{PS1}	PS1
2013-07-07	56480.29	+121.46	22.75 ± 0.63	z_{PS1}	PS1
2013-07-09	56482.29	+123.32	22.98 ± 0.47	z_{PS1}	PS1
2013-07-12	56485.27	+126.09	22.53 ± 0.53	z_{PS1}	PS1
2013-07-15	56488.28	+128.88	22.85 ± 0.27	z_{PS1}	PS1
2013-07-17	56490.27	+130.73	22.54 ± 0.17	z_{PS1}	PS1
2013-07-19	56492.31	+132.63	22.66 ± 0.20	z_{PS1}	PS1
2013-08-07	56511.27	+150.25	22.86 ± 0.31	z_{PS1}	PS1
2013-02-26	56349.60	+0.00	20.41 ± 0.21	y_{PS1}	PS1
2013-03-01	56352.60	+2.79	20.28 ± 0.23	y_{PS1}	PS1
2013-03-09	56360.65	+10.26	20.12 ± 0.20	y_{PS1}	PS1
2013-03-13	56364.59	+13.93	20.20 ± 0.25	y_{PS1}	PS1
2013-03-26	56377.52	+25.94	20.64 ± 0.61	y_{PS1}	PS1
2013-03-29	56380.52	+28.74	20.32 ± 0.19	y_{PS1}	PS1
2013-04-06	56388.48	+36.13	20.06 ± 0.23	y_{PS1}	PS1
2013-04-18	56400.50	+47.31	20.41 ± 0.30	y_{PS1}	PS1
2013-04-23	56405.55	+52.00	20.53 ± 0.20	y_{PS1}	PS1
2013-04-24	56406.49	+52.87	20.36 ± 0.18	y_{PS1}	PS1
2013-04-26	56408.42	+54.66	20.37 ± 0.19	y_{PS1}	PS1
2013-04-27	56409.47	+55.64	20.51 ± 0.09	y_{PS1}	PS1
2013-04-28	56410.48	+56.57	20.47 ± 0.52	y_{PS1}	PS1
2013-04-30	56412.43	+58.39	20.48 ± 0.10	y_{PS1}	PS1
2013-05-05	56417.51	+63.11	20.28 ± 0.15	y_{PS1}	PS1
2013-05-17	56429.40	+74.16	20.37 ± 0.28	y_{PS1}	PS1
2013-05-23	56435.44	+79.77	20.93 ± 0.32	y_{PS1}	PS1
2013-05-24	56436.44	+80.70	20.74 ± 0.16	y_{PS1}	PS1
2013-05-25	56437.45	+81.64	20.63 ± 0.74	y_{PS1}	PS1
2013-05-27	56439.42	+83.47	20.59 ± 0.30	y_{PS1}	PS1
2013-06-21	56464.32	+106.61	21.73 ± 0.22	y_{PS1}	PS1
2013-06-23	56466.34	+108.49	21.72 ± 0.72	y_{PS1}	PS1
2013-06-24	56467.34	+109.42	21.52 ± 0.66	y_{PS1}	PS1
2013-06-25	56468.34	+110.35	21.91 ± 0.96	y_{PS1}	PS1
2013-07-11	56484.30	+125.19	21.90 ± 0.94	y_{PS1}	PS1

The tabulated magnitudes are given “as observed”, i.e. neither corrected for dust extinction nor K -corrected. *Rest frame epochs (assuming a redshift of 0.076) with respect to the first detection on 56349.60 (MJD). PS1 = Panoramic Survey Telescope & Rapid Response System 1.

Table A.4: PS1-13wr: Journal of spectroscopic observations

Date	MJD	Epoch* rest frame	Wavelength range in Å	Resolution Å	Telescope+Instrument
2013-03-11	56362.26	+11.77	3600 - 9970	17.0	GTC+OSIRIS+R300B
2013-03-17	56369.12	+18.14	3770 - 9970	17.0	GTC+OSIRIS+R300B
2013-03-25	56376.23	+24.74	3730 - 9865	16.7	GTC+OSIRIS+R300B
2013-04-11	56394.15	+41.40	3640 - 9895	16.9	GTC+OSIRIS+R300B

*Rest frame epochs (assuming a redshift of 0.076) with respect to the first detection on 56349.60 (MJD). The resolution was determined from the FWHM of the $\text{O I } \lambda 5577.34$ sky line.

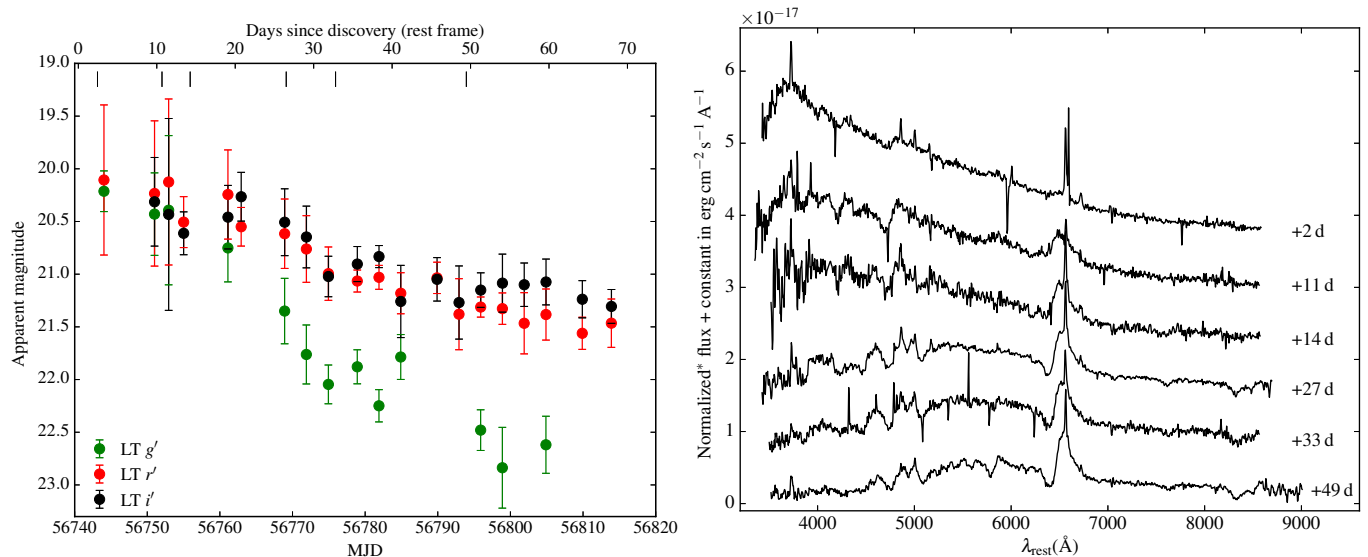


Fig. A.3: PS1-14vk. Left panel: LT $g'r'i'$ light curves of PS1-14vk. The vertical ticks on the top mark the epochs of the observed spectra. Right panel: PS1-14vk spectroscopy. *Flux normalized to the maximum H α flux for better visibility of the features. The exact normalizations are: flux/2.6 for the +2 d spectrum; flux/2.7 for +11 d; flux/2.8 for +14 d; flux/2.3 for +27 d; flux/2.1 for +33 d; flux/1.9 for +49 d.

tionally obtained a series of four GTC spectra ranging between +23 and +81 d (rest frame) after discovery.

PS1-12bku displays neither narrow emissions reminiscent of the host galaxy nor is a spectroscopic redshift for its host galaxy available in a public data base. With the objective of estimating the redshift of PS1-12bku, we performed a series of cross correlations using SNID (Supernova Identification, Blondin & Tonry 2007). Suggested matches were scrutinized and the selected results span a range of redshifts between 0.086 and 0.094 with a median of 0.088. We therefore adopt this value as the redshift of the SN, and give the range in redshifts mentioned above as a conservative estimate of its uncertainty: $z = 0.088^{+0.006}_{-0.002}$.

No features attributable to the Na I doublet from interstellar gas either in the Milky Way or the host galaxy, are apparent in the spectra of PS1-12bku. Consequently, we derived an upper limit for the equivalent width of the Na I D $\lambda\lambda 5890, 5896$ blend in the same manner as for SN 2013ca (see Section A.1). We find $\text{EW}_{\text{NaID}} < 1.1 \text{\AA}$, which translates into a host extinction of $E(B - V)_{\text{host}} < 0.27 \text{ mag}$ (Equation 9 of Poznanski et al. 2012).

The light curves of PS1-12bku are presented in the left panel of Figure A.4. Table A.7 shows the log of imaging observations as well as the final calibrated magnitudes. PS1-12bku was discovered only 0.8 d after the last non-detection in the z_{PS1} -band on MJD 56160.51. This allows us to constrain the explosion epoch of PS1-12bku to MJD 56160.9 ± 0.4 . The r_{PS1} -, i_{PS1} -, z_{PS1} -, y_{PS1} light curves display a plateau that seems to last until about 100 days after discovery where the r -band data suggests a drop in the luminosity.

Table A.8 gives the journal of spectroscopic observations for PS1-12bku. The fully reduced and calibrated spectra of PS1-12bku are presented in the right panel of Figure A.4. They are corrected for galactic reddening and redshift ($z = 0.088$). The spectra of PS1-12bku display strong features of H α and H β . A weak Fe II $\lambda 5169$ absorption can also be seen at all epochs.

Appendix A.7: PS1-13abg

PS1-13abg was discovered on 2013 March 29 by the PS1 MD survey. $g_{\text{PS1}}r_{\text{PS1}}i_{\text{PS1}}z_{\text{PS1}}y_{\text{PS1}}$ photometry was obtained in the course of the PS1 MD survey up to 38 d (rest frame) after the first detection. We additionally obtained a series of three GTC spectra ranging between +7 and +44 d (rest frame) after discovery.

PS1-13abg lies close to the galaxy zCOSMOS 824314, for which Lilly et al. (2007) report a redshift of 0.123 ± 0.001 . This redshift was adopted also for PS1-13abg.

Features attributable to the Na I doublet from interstellar gas either in the Milky Way or the host galaxy, are not apparent in the spectra of PS1-13abg. Consequently, we derived an upper limit for the equivalent width of the Na I D $\lambda\lambda 5890, 5896$ blend in the same manner as for SN 2013ca (see Section A.1). We find $\text{EW}_{\text{NaID}} < 0.6 \text{\AA}$, which corresponds to a host extinction of $E(B - V)_{\text{host}} < 0.07 \text{ mag}$ (Equation 9 of Poznanski et al. 2012).

The light curves of PS1-13abg are presented in the left panel of Figure A.5. Table A.9 shows the log of imaging observations as well as the final calibrated magnitudes. PS1-13abg was discovered ten days after the last non-detection in the z_{PS1} -band on MJD 56370.34. This allows us to put a loose constraint on the explosion epoch of PS1-13abg to MJD 56375.4 ± 5.0 . The r_{PS1} -, i_{PS1} -, z_{PS1} -, y_{PS1} light curves display a clear plateau. The drop onto the radioactive tail is not observed.

Table A.10 gives the journal of spectroscopic observations for PS1-13abg. The fully reduced and calibrated spectra of PS1-13abg are presented in the right panel of Figure A.5. They are corrected for galactic reddening and redshift ($z = 0.123$). The +7 d spectrum of PS1-13abg is an almost featureless continuum with the exception of two narrow lines in the regions of H α and H β , respectively. The +32 and +44 d spectra exhibit features of both H α and H β , the +32 d H α line showing a strong narrow component. Narrow components are not observed in the +44 d spectrum, this could, however, be due to the poor signal-to-noise ratio in the last spectrum. A weak Fe II $\lambda 5169$ absorption can also be found in the +44 d spectrum.

Table A.5: PS1-14vk: Photometric observations

Date	MJD	Rest frame epoch*	Magnitude	Filter	Telescope
2014-03-27	56744.04	+3.26	20.21 ± 0.19	g'	LT
2014-04-03	56751.00	+9.71	20.43 ± 0.39	g'	LT
2014-04-05	56752.95	+11.51	20.39 ± 0.71	g'	LT
2014-04-13	56761.11	+19.07	20.75 ± 0.32	g'	LT
2014-04-21	56768.91	+26.30	21.35 ± 0.31	g'	LT
2014-04-24	56771.91	+29.07	21.76 ± 0.28	g'	LT
2014-04-27	56774.94	+31.88	22.05 ± 0.18	g'	LT
2014-05-01	56778.92	+35.56	21.88 ± 0.16	g'	LT
2014-05-04	56781.90	+38.32	22.25 ± 0.15	g'	LT
2014-05-07	56784.90	+41.10	21.79 ± 0.21	g'	LT
2014-05-18	56795.90	+51.29	22.48 ± 0.19	g'	LT
2014-05-21	56798.89	+54.05	22.84 ± 0.38	g'	LT
2014-05-27	56804.89	+59.61	22.62 ± 0.27	g'	LT
2014-03-27	56744.04	+3.27	20.11 ± 0.71	r'	LT
2014-04-03	56751.00	+9.71	20.23 ± 0.69	r'	LT
2014-04-05	56752.95	+11.51	20.12 ± 0.79	r'	LT
2014-04-07	56755.01	+13.43	20.51 ± 0.24	r'	LT
2014-04-13	56761.11	+19.07	20.24 ± 0.42	r'	LT
2014-04-15	56762.93	+20.76	20.55 ± 0.18	r'	LT
2014-04-21	56768.92	+26.30	20.62 ± 0.33	r'	LT
2014-04-24	56771.91	+29.07	20.76 ± 0.32	r'	LT
2014-04-27	56774.94	+31.88	21.00 ± 0.25	r'	LT
2014-05-01	56778.92	+35.56	21.07 ± 0.10	r'	LT
2014-05-04	56781.91	+38.33	21.03 ± 0.11	r'	LT
2014-05-07	56784.90	+41.10	21.18 ± 0.19	r'	LT
2014-05-12	56789.90	+45.73	21.04 ± 0.15	r'	LT
2014-05-15	56792.92	+48.53	21.38 ± 0.34	r'	LT
2014-05-18	56795.91	+51.29	21.31 ± 0.10	r'	LT
2014-05-21	56798.90	+54.06	21.33 ± 0.15	r'	LT
2014-05-24	56801.90	+56.84	21.47 ± 0.29	r'	LT
2014-05-27	56804.90	+59.62	21.38 ± 0.24	r'	LT
2014-06-01	56809.89	+64.24	21.56 ± 0.15	r'	LT
2014-06-05	56813.90	+67.95	21.46 ± 0.23	r'	LT
2014-04-03	56751.00	+9.71	20.31 ± 0.42	i'	LT
2014-04-05	56752.95	+11.51	20.43 ± 0.91	i'	LT
2014-04-07	56755.01	+13.43	20.61 ± 0.20	i'	LT
2014-04-13	56761.11	+19.07	20.46 ± 0.30	i'	LT
2014-04-15	56762.93	+20.76	20.27 ± 0.23	i'	LT
2014-04-21	56768.92	+26.30	20.51 ± 0.32	i'	LT
2014-04-24	56771.91	+29.07	20.65 ± 0.29	i'	LT
2014-04-27	56774.95	+31.88	21.02 ± 0.19	i'	LT
2014-05-01	56778.92	+35.56	20.90 ± 0.17	i'	LT
2014-05-04	56781.91	+38.33	20.83 ± 0.10	i'	LT
2014-05-07	56784.91	+41.11	21.26 ± 0.34	i'	LT
2014-05-12	56789.90	+45.73	21.05 ± 0.21	i'	LT
2014-05-15	56792.93	+48.53	21.27 ± 0.35	i'	LT
2014-05-18	56795.91	+51.30	21.15 ± 0.16	i'	LT
2014-05-21	56798.90	+54.06	21.09 ± 0.28	i'	LT
2014-05-24	56801.90	+56.84	21.10 ± 0.21	i'	LT
2014-05-27	56804.90	+59.62	21.07 ± 0.22	i'	LT
2014-06-01	56809.90	+64.25	21.24 ± 0.18	i'	LT
2014-06-05	56813.91	+67.96	21.31 ± 0.16	i'	LT

The tabulated magnitudes are given “as observed”, i.e. neither corrected for dust extinction nor K -corrected. *Rest frame epochs (assuming a redshift of 0.080) with respect to the first detection on 56740.51 (MJD). LT = Liverpool Telescope.

Appendix A.8: PS1-13baf

PS1-13baf was discovered on 2013 August 13 by the PS1 MD survey. $g_{\text{PS1}} r_{\text{PS1}} i_{\text{PS1}} z_{\text{PS1}} y_{\text{PS1}}$ photometry was obtained in the course of the PS1 MD survey up to 113 d (rest frame) after the first detection. We additionally obtained a series of three GTC spectra ranging between +16 and +39 d (rest frame) after discovery.

Spectroscopic redshifts of the host galaxy were not available for PS1-13baf. Its redshift was therefore determined by measuring the narrow H_{α} and H_{β} component (presumably a contamination from the host galaxy) in the +28 and +39 d spectra and averaging the respective results: $z = 0.144 \pm 0.001$.

Features attributable to the Na I doublet from interstellar gas either in the Milky Way or the host galaxy, are not apparent in the spectra of PS1-13baf. Consequently, we derived an upper

Table A.6: PS1-14vk: Journal of spectroscopic observations

Date	MJD	Epoch* rest frame	Wavelength range in Å	Resolution Å	Telescope+Instrument
2014-03-26	56743.15	+2.44	3700 - 9290	17.0	GTC+OSIRIS+R300B
2014-04-04	56752.03	+10.66	3620 - 9270	16.7	GTC+OSIRIS+R300B
2014-04-08	56755.91	+14.26	3800 - 9280	16.5	GTC+OSIRIS+R300B
2014-04-21	56769.13	+26.50	3700 - 9410	16.6	GTC+OSIRIS+R300B
2014-04-28	56775.93	+32.79	3780 - 9270	17.0	GTC+OSIRIS+R300B
2014-05-16	56793.93	+49.46	3800 - 9750	16.8	GTC+OSIRIS+R300B

*Rest frame epochs (assuming a redshift of 0.080) with respect to the first detection on 56740.51 (MJD). The resolution was determined from the FWHM of the O I $\lambda 5577.34$ sky line.

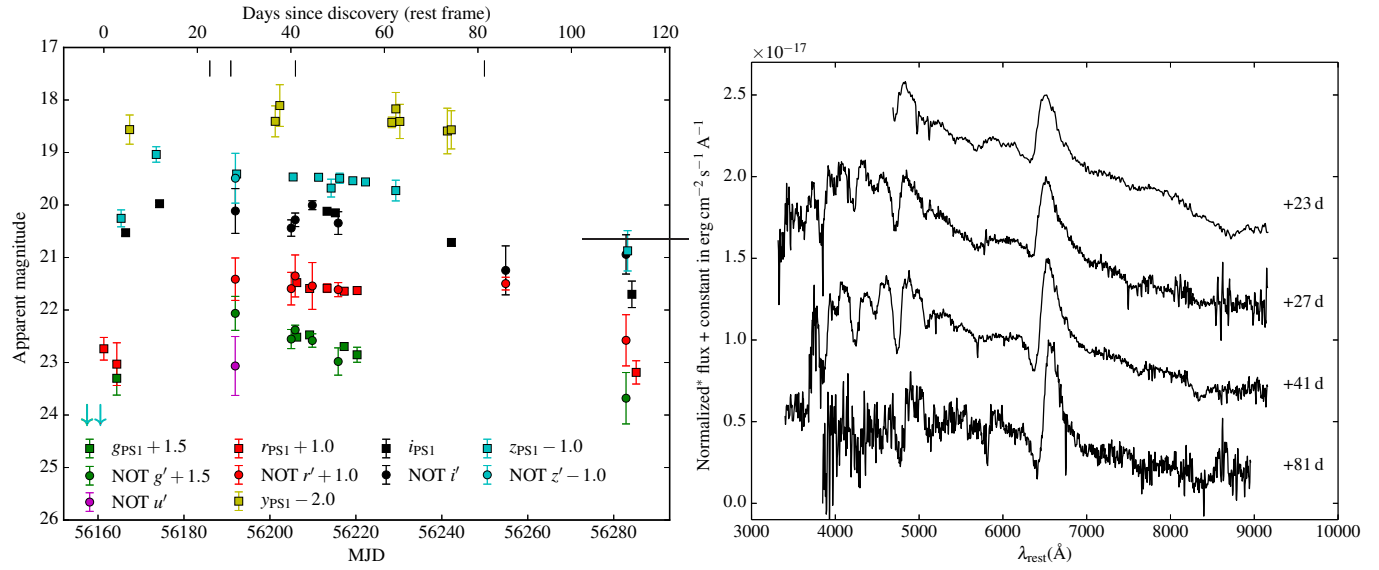


Fig. A.4: PS1-12bku. Left panel: $grizy_{\text{PS1}}$ and NOT $u'g'r'i'z'$ light curves of PS1-12bku. The vertical ticks on the top mark the epochs of the observed spectra. Right panel: PS1-12bku spectroscopy. *Flux normalized to the maximum H α flux for better visibility of the features. The exact normalizations are: flux/3.3 for the +23 d spectrum; flux/3.6 for +27 d; flux/3.5 for +41 d; flux/2.9 for +81 d.

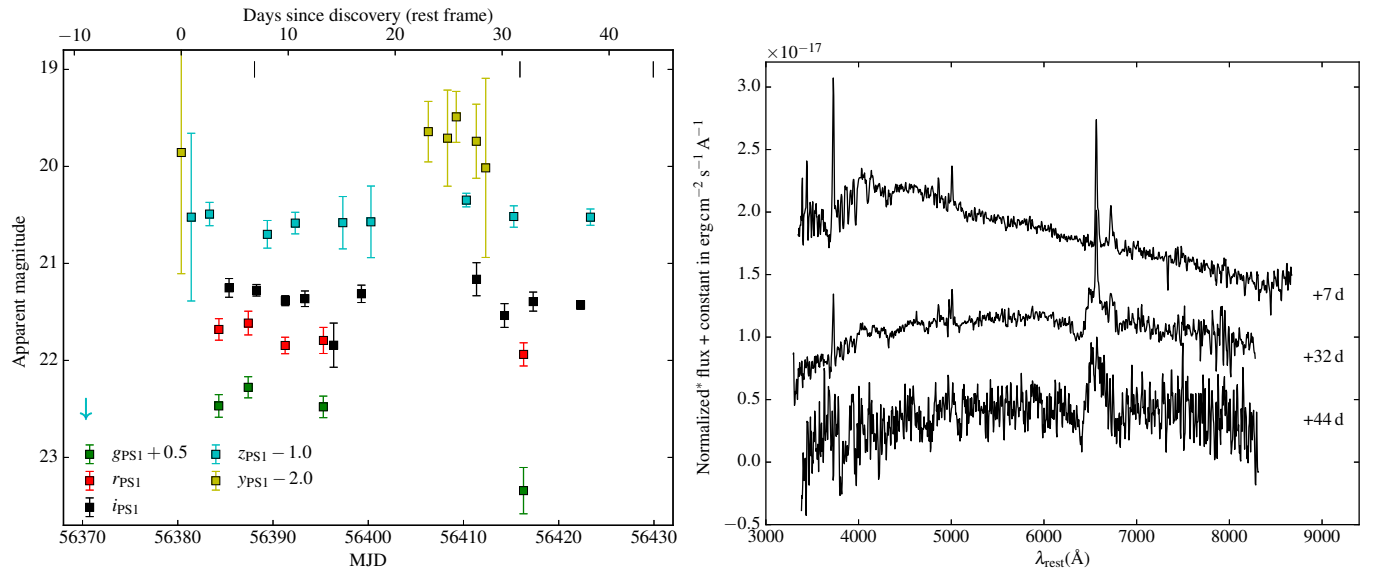


Fig. A.5: PS1-13abg. Left panel: $grizy_{\text{PS1}}$ light curves of PS1-13abg. The vertical ticks on the top mark the epochs of the observed spectra. Right panel: PS1-13abg spectroscopy. *Flux normalized to the maximum H α flux for better visibility of the features. The exact normalizations are: flux/0.7 for the +7 d spectrum; flux/0.8 for +32 d; flux/1.1 for +44 d.

Table A.7: PS1-12bku: Photometric observations

Date	MJD	Rest frame epoch*	Magnitude	Filter	Telescope
2012-09-21	56191.93	+28.10	23.07 ± 0.56	<i>u</i>	NOT
2012-08-25	56164.36	+2.76	21.80 ± 0.32	<i>gps1</i>	PS1
2012-10-06	56206.24	+41.25	21.01 ± 0.06	<i>gps1</i>	PS1
2012-10-09	56209.24	+44.01	20.97 ± 0.04	<i>gps1</i>	PS1
2012-10-17	56217.28	+51.40	21.20 ± 0.07	<i>gps1</i>	PS1
2012-10-20	56220.28	+54.16	21.35 ± 0.14	<i>gps1</i>	PS1
2012-09-21	56191.94	+28.11	20.56 ± 0.32	<i>g'</i>	NOT
2012-10-04	56204.95	+40.07	21.05 ± 0.18	<i>g'</i>	NOT
2012-10-05	56205.88	+40.92	20.88 ± 0.09	<i>g'</i>	NOT
2012-10-09	56209.86	+44.58	21.08 ± 0.13	<i>g'</i>	NOT
2012-10-15	56215.88	+50.12	21.48 ± 0.26	<i>g'</i>	NOT
2012-12-21	56282.86	+111.68	22.18 ± 0.49	<i>g'</i>	NOT
2012-08-22	56161.36	+0.00	21.74 ± 0.22	<i>rps1</i>	PS1
2012-08-25	56164.37	+2.77	22.03 ± 0.41	<i>rps1</i>	PS1
2012-10-06	56206.25	+41.26	20.48 ± 0.03	<i>rps1</i>	PS1
2012-10-09	56209.25	+44.02	20.59 ± 0.04	<i>rps1</i>	PS1
2012-10-13	56213.31	+47.75	20.59 ± 0.08	<i>rps1</i>	PS1
2012-10-17	56217.29	+51.41	20.64 ± 0.05	<i>rps1</i>	PS1
2012-10-20	56220.30	+54.17	20.63 ± 0.07	<i>rps1</i>	PS1
2012-12-24	56285.22	+113.85	22.19 ± 0.22	<i>rps1</i>	PS1
2012-09-21	56191.95	+28.12	20.41 ± 0.40	<i>r'</i>	NOT
2012-10-04	56204.96	+40.07	20.59 ± 0.31	<i>r'</i>	NOT
2012-10-05	56205.88	+40.92	20.35 ± 0.40	<i>r'</i>	NOT
2012-10-09	56209.86	+44.58	20.54 ± 0.45	<i>r'</i>	NOT
2012-10-15	56215.89	+50.12	20.61 ± 0.13	<i>r'</i>	NOT
2012-11-23	56254.86	+85.94	20.50 ± 0.12	<i>r'</i>	NOT
2012-12-21	56282.87	+111.68	21.58 ± 0.49	<i>r'</i>	NOT
2012-08-27	56166.43	+4.66	20.53 ± 0.05	<i>i_{PS1}</i>	PS1
2012-09-04	56174.33	+11.92	19.98 ± 0.03	<i>i_{PS1}</i>	PS1
2012-10-13	56213.29	+47.73	20.12 ± 0.06	<i>i_{PS1}</i>	PS1
2012-10-15	56215.23	+49.51	20.15 ± 0.06	<i>i_{PS1}</i>	PS1
2012-11-11	56242.23	+74.34	20.71 ± 0.06	<i>i_{PS1}</i>	PS1
2012-12-23	56284.22	+112.93	21.70 ± 0.25	<i>i_{PS1}</i>	PS1
2012-09-21	56191.96	+28.13	20.11 ± 0.43	<i>i'</i>	NOT
2012-10-04	56204.96	+40.08	20.44 ± 0.16	<i>i'</i>	NOT
2012-10-05	56205.88	+40.92	20.28 ± 0.13	<i>i'</i>	NOT
2012-10-09	56209.87	+44.59	20.00 ± 0.08	<i>i'</i>	NOT
2012-10-15	56215.89	+50.12	20.34 ± 0.22	<i>i'</i>	NOT
2012-11-23	56254.86	+85.94	21.25 ± 0.47	<i>i'</i>	NOT
2012-12-21	56282.87	+111.68	20.94 ± 0.37	<i>i'</i>	NOT
2012-08-26	56165.38	+3.70	21.25 ± 0.16	<i>z_{PS1}</i>	PS1
2012-09-03	56173.55	+11.21	20.04 ± 0.18	<i>z_{PS1}</i>	PS1
2012-09-22	56192.26	+28.40	20.41 ± 0.06	<i>z_{PS1}</i>	PS1
2012-10-05	56205.40	+40.48	20.47 ± 0.02	<i>z_{PS1}</i>	PS1
2012-10-11	56211.33	+45.93	20.47 ± 0.04	<i>z_{PS1}</i>	PS1
2012-10-14	56214.25	+48.61	20.68 ± 0.17	<i>z_{PS1}</i>	PS1
2012-10-16	56216.23	+50.43	20.49 ± 0.10	<i>z_{PS1}</i>	PS1
2012-10-19	56219.29	+53.25	20.54 ± 0.04	<i>z_{PS1}</i>	PS1
2012-10-22	56222.24	+55.96	20.56 ± 0.04	<i>z_{PS1}</i>	PS1
2012-10-29	56229.29	+62.43	20.73 ± 0.20	<i>z_{PS1}</i>	PS1
2012-12-22	56283.23	+112.02	21.87 ± 0.38	<i>z_{PS1}</i>	PS1
2012-09-21	56191.97	+28.14	20.49 ± 0.47	<i>z'</i>	NOT
2012-08-28	56167.36	+5.52	20.56 ± 0.28	<i>y_{PS1}</i>	PS1
2012-10-01	56201.24	+36.65	20.41 ± 0.29	<i>y_{PS1}</i>	PS1
2012-10-02	56202.30	+37.63	20.11 ± 0.40	<i>y_{PS1}</i>	PS1
2012-10-28	56228.36	+61.59	20.43 ± 0.10	<i>y_{PS1}</i>	PS1
2012-10-29	56229.29	+62.44	20.17 ± 0.31	<i>y_{PS1}</i>	PS1
2012-10-30	56230.23	+63.30	20.41 ± 0.33	<i>y_{PS1}</i>	PS1
2012-11-10	56241.29	+73.46	20.59 ± 0.43	<i>y_{PS1}</i>	PS1
2012-11-11	56242.20	+74.31	20.57 ± 0.36	<i>y_{PS1}</i>	PS1

The tabulated magnitudes are given “as observed”, i.e. neither corrected for dust extinction nor K -corrected. *Rest frame epochs (assuming a redshift of 0.088) with respect to the discovery on 56161.36 (MJD). NOT = Nordic Optical Telescope; PS1 = Panoramic Survey Telescope & Rapid Response System 1.

Table A.8: PS1-12bku: Journal of spectroscopic observations

Date	MJD	Epoch* rest frame	Wavelength range in Å	Resolution Å	Telescope+Instrument
2012-09-16	56186.01	+22.66	5100 - 9999	31.2	GTC+OSIRIS+R300R
2012-09-20	56190.90	+27.15	3400 - 9965	21.3	GTC+OSIRIS+R300B
2012-10-05	56205.94	+40.98	3700 - 9965	21.6	GTC+OSIRIS+R300B
2012-11-17	56249.92	+81.40	3980 - 9755	21.4	GTC+OSIRIS+R300B

*Rest frame epochs (assuming a redshift of 0.088) with respect to the first detection on 56161.36 (MJD). The resolution was determined from the FWHM of the O I $\lambda 5577.34$ sky line.

Table A.9: PS1-13abg: Photometric observations

Date	MJD	Rest frame epoch*	Magnitude	Filter	Telescope
2013-04-02	56384.31	+3.51	21.97 \pm 0.12	g_{PS1}	PS1
2013-04-05	56387.39	+6.25	21.78 \pm 0.11	g_{PS1}	PS1
2013-04-13	56395.28	+13.28	21.98 \pm 0.11	g_{PS1}	PS1
2013-05-04	56416.30	+32.00	22.84 \pm 0.24	g_{PS1}	PS1
2013-04-02	56384.32	+3.52	21.68 \pm 0.11	r_{PS1}	PS1
2013-04-05	56387.40	+6.26	21.61 \pm 0.12	r_{PS1}	PS1
2013-04-09	56391.27	+9.71	21.85 \pm 0.08	r_{PS1}	PS1
2013-04-13	56395.29	+13.29	21.79 \pm 0.13	r_{PS1}	PS1
2013-05-04	56416.31	+32.01	21.94 \pm 0.12	r_{PS1}	PS1
2013-04-03	56385.38	+4.47	21.25 \pm 0.10	i_{PS1}	PS1
2013-04-06	56388.27	+7.03	21.28 \pm 0.06	i_{PS1}	PS1
2013-04-09	56391.29	+9.73	21.38 \pm 0.05	i_{PS1}	PS1
2013-04-11	56393.35	+11.56	21.36 \pm 0.08	i_{PS1}	PS1
2013-04-14	56396.37	+14.25	21.84 \pm 0.23	i_{PS1}	PS1
2013-04-17	56399.28	+16.84	21.31 \pm 0.09	i_{PS1}	PS1
2013-04-29	56411.37	+27.61	21.16 \pm 0.17	i_{PS1}	PS1
2013-05-02	56414.31	+30.22	21.54 \pm 0.12	i_{PS1}	PS1
2013-05-05	56417.32	+32.90	21.39 \pm 0.10	i_{PS1}	PS1
2013-05-10	56422.29	+37.33	21.43 \pm 0.04	i_{PS1}	PS1
2013-03-30	56381.41	+0.93	21.52 \pm 0.86	z_{PS1}	PS1
2013-04-01	56383.34	+2.64	21.49 \pm 0.12	z_{PS1}	PS1
2013-04-07	56389.40	+8.05	21.70 \pm 0.14	z_{PS1}	PS1
2013-04-10	56392.33	+10.66	21.58 \pm 0.11	z_{PS1}	PS1
2013-04-15	56397.33	+15.11	21.58 \pm 0.27	z_{PS1}	PS1
2013-04-18	56400.28	+17.73	21.57 \pm 0.37	z_{PS1}	PS1
2013-04-28	56410.30	+26.65	21.35 \pm 0.07	z_{PS1}	PS1
2013-05-03	56415.28	+31.09	21.52 \pm 0.11	z_{PS1}	PS1
2013-05-11	56423.33	+38.25	21.52 \pm 0.08	z_{PS1}	PS1
2013-03-29	56380.37	+0.00	21.86 \pm 1.25	y_{PS1}	PS1
2013-04-24	56406.31	+23.10	21.64 \pm 0.31	y_{PS1}	PS1
2013-04-26	56408.32	+24.89	21.71 \pm 0.50	y_{PS1}	PS1
2013-04-27	56409.24	+25.71	21.49 \pm 0.26	y_{PS1}	PS1
2013-04-29	56411.34	+27.58	21.74 \pm 0.38	y_{PS1}	PS1
2013-04-30	56412.33	+28.46	22.02 \pm 0.92	y_{PS1}	PS1

The tabulated magnitudes are given “as observed”, i.e. neither corrected for dust extinction nor K -corrected. *Rest frame epochs (assuming a redshift of 0.123) with respect to the first detection on 56380.37 (MJD). PS1 = Panoramic Survey Telescope & Rapid Response System 1.

limit for the equivalent width of the Na I D $\lambda\lambda 5890,5896$ blend in the same manner as for SN 2013ca (see Section A.1). We find $EW_{NaID} < 1.2$ Å, which can be converted into a host extinction of $E(B-V)_{host} < 0.36$ mag (Equation 9 of Poznanski et al. 2012).

The light curves of PS1-13baf are presented in the left panel of Figure A.6. Table A.11 shows the log of imaging observations as well as the final calibrated magnitudes. PS1-13baf was discovered three days after the last non-detection in the y_{PS1} -band on MJD 56406.59. This allows us to constrain the explosion epoch of PS1-13abg to $MJD 56408.0 \pm 1.5$. The light curves in all filters display a clear plateau until at least 100 d (rest frame) after discovery.

Table A.10: PS1-13abg: Journal of spectroscopic observations

Date	MJD	Epoch* rest frame	Wavelength range in Å	Resolution Å	Telescope+Instrument
2013-04-05	56388.06	+6.85	3760 - 9740	16.8	GTC+OSIRIS+R300B
2013-05-03	56415.93	+31.66	3700 - 9800	17.2	GTC+OSIRIS+R300B
2013-05-17	56429.93	+44.13	3800 - 9335	20.6	GTC+OSIRIS+R300B

*Rest frame epochs (assuming a redshift of 0.123) with respect to the first detection on 56380.37 (MJD). The resolution was determined from the FWHM of the O I $\lambda 5577.34$ sky line.

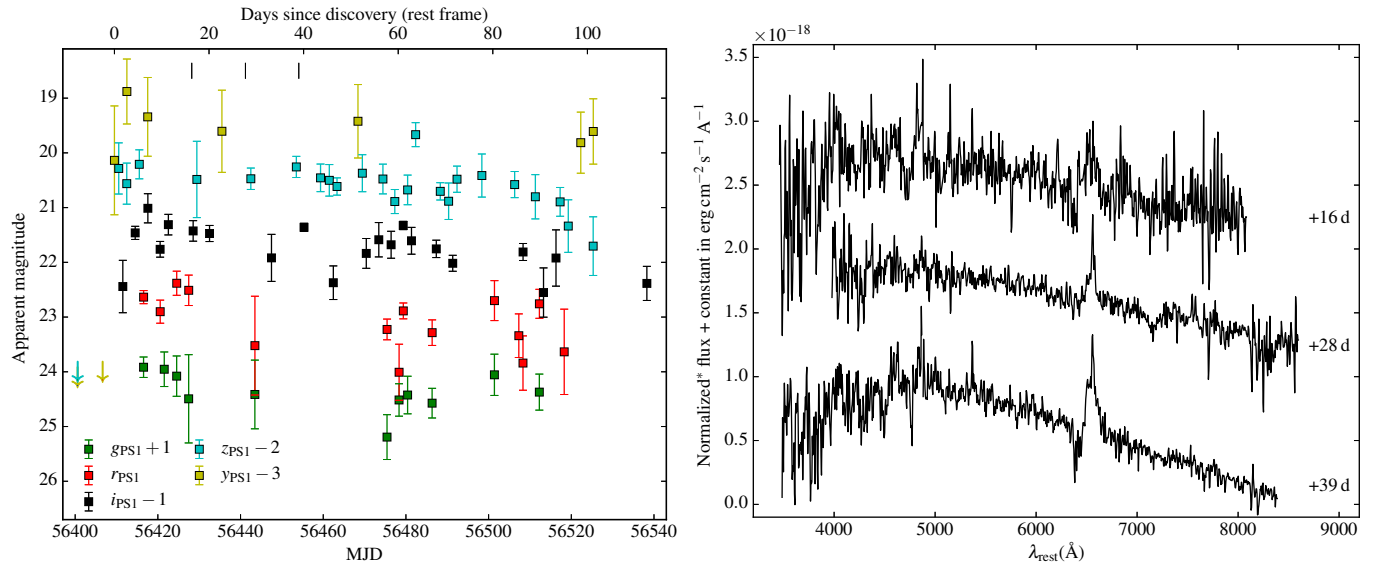


Fig. A.6: PS1-13baf. Left panel: $grizy_{PS1}$ light curves of PS1-13baf. The vertical ticks on the top mark the epochs of the observed spectra. Right panel: PS1-13baf spectroscopy. *Flux normalized to the maximum H α flux for better visibility of the features. The exact normalizations are: flux/4.1 for the +16 d spectrum; flux/3.2 for +28 d; flux/2.9 for +39 d.

Table A.12 gives the journal of spectroscopic observations for PS1-13baf. The fully reduced and calibrated spectra of PS1-13baf are presented in the right panel of Figure A.6. They are corrected for galactic reddening and redshift ($z = 0.144$). The spectra of PS1-13baf show strong features of H α and H β , with narrow components from the host galaxy overlaid in the +28 and +39 d spectra. Iron lines cannot be identified, due to the poor signal-to-noise ratio of the spectra.

Appendix A.9: PS1-13bmf

PS1-13bmf was discovered on 2013 May 8 by the PS1 MD survey. $g_{PS1}r_{PS1}i_{PS1}z_{PS1}y_{PS1}$ photometry was obtained in the course of the PS1 MD survey up to 52 d (rest frame) after the first detection. We additionally obtained a series of four GTC spectra ranging between +5 and +47 d (rest frame) after discovery.

PS1-13bmf lies in the vicinity of the galaxy SDSS J122311.46+474426.7 for which the SDSS reports a spectroscopic redshift of 0.163 ± 0.001 . This redshift was adopted also for PS1-13bmf.

Features attributable to the Na I doublet from interstellar gas either in the Milky Way or the host galaxy, are not apparent in the spectra of PS1-13bmf. However, due to the very low signal-to-noise ratio of the spectra we refrain from giving a meaningless upper limit for the EW of the Na I D blend or the host galaxy extinction. In particular, the logarithmic relation between the EW of the Na I D blend and $E(B - V)$ presented in Equation 9 of

Poznanski et al. (2012) is valid only for small EW and leads to unphysical results for $EW_{NaID} > 2 \text{ \AA}$.

The light curves of PS1-13bmf are presented in the left panel of Figure A.7. Table A.13 shows the log of imaging observations as well as the final calibrated magnitudes. PS1-13bmf was likely discovered very close to the explosion, as can be inferred by the observed initial rise in the g_{PS1} , r_{PS1} , and z_{PS1} light curves and in particular the very steep rise in the i_{PS1} band. A fit to the early photometry results in an estimate for the explosion epoch of MJD 56420.0 ± 0.1 . The g_{PS1} , r_{PS1} , i_{PS1} , and z_{PS1} light curves decline linearly, with the r_{PS1} and i_{PS1} decline rates being $1.05 \pm 0.11 \text{ mag/50 d}$ and $0.76 \pm 0.11 \text{ mag/50 d}$, respectively. We therefore classify PS1-13bmf as a Type II-L SN following Li et al. (2011).

Table A.14 gives the journal of spectroscopic observations for PS1-13bmf. The fully reduced and calibrated spectra of PS1-13bmf are presented in the right panel of Figure A.7. They are corrected for galactic reddening and redshift ($z = 0.163$). The +5 d spectrum of PS1-13abg is a featureless blue continuum and displays no visible features. The +8 d is similar, though less extreme, with very weak features of H α and H β visible. The last two spectra display more prominent lines of H α and H β as well as weak lines of iron, in particular Fe II $\lambda 5169$.

Table A.11: PS1-13baf: Photometric observations

Date	MJD	Rest frame epoch*	Magnitude	Filter	Telescope
2013-05-04	56416.54	+6.16	22.92 ± 0.19	<i>gps1</i>	PS1
2013-05-09	56421.55	+10.54	22.95 ± 0.32	<i>gps1</i>	PS1
2013-05-12	56424.55	+13.16	23.08 ± 0.37	<i>gps1</i>	PS1
2013-05-15	56427.45	+15.70	23.49 ± 0.81	<i>gps1</i>	PS1
2013-05-31	56443.46	+29.69	23.41 ± 0.63	<i>gps1</i>	PS1
2013-07-02	56475.43	+57.63	24.19 ± 0.41	<i>gps1</i>	PS1
2013-07-05	56478.34	+60.18	23.51 ± 0.30	<i>gps1</i>	PS1
2013-07-07	56480.41	+61.99	23.42 ± 0.34	<i>gps1</i>	PS1
2013-07-13	56486.33	+67.17	23.57 ± 0.27	<i>gps1</i>	PS1
2013-07-28	56501.40	+80.34	23.06 ± 0.38	<i>gps1</i>	PS1
2013-08-08	56512.27	+89.84	23.37 ± 0.33	<i>gps1</i>	PS1
2013-05-04	56416.55	+6.17	22.64 ± 0.12	<i>rps1</i>	PS1
2013-05-08	56420.57	+9.68	22.90 ± 0.21	<i>rps1</i>	PS1
2013-05-12	56424.56	+13.17	22.38 ± 0.22	<i>rps1</i>	PS1
2013-05-15	56427.46	+15.71	22.51 ± 0.28	<i>rps1</i>	PS1
2013-05-31	56443.48	+29.70	23.52 ± 0.90	<i>rps1</i>	PS1
2013-07-02	56475.44	+57.65	23.23 ± 0.19	<i>rps1</i>	PS1
2013-07-05	56478.35	+60.19	24.01 ± 0.51	<i>rps1</i>	PS1
2013-07-06	56479.37	+61.08	22.89 ± 0.14	<i>rps1</i>	PS1
2013-07-13	56486.34	+67.18	23.28 ± 0.23	<i>rps1</i>	PS1
2013-07-28	56501.41	+80.35	22.70 ± 0.36	<i>rps1</i>	PS1
2013-08-03	56507.31	+85.50	23.34 ± 0.40	<i>rps1</i>	PS1
2013-08-04	56508.31	+86.38	23.84 ± 0.50	<i>rps1</i>	PS1
2013-08-08	56512.28	+89.85	22.76 ± 0.26	<i>rps1</i>	PS1
2013-08-14	56518.29	+95.10	23.64 ± 0.78	<i>rps1</i>	PS1
2013-04-29	56411.52	+1.77	23.44 ± 0.48	<i>ips1</i>	PS1
2013-05-02	56414.52	+4.39	22.46 ± 0.12	<i>ips1</i>	PS1
2013-05-05	56417.58	+7.07	22.01 ± 0.27	<i>ips1</i>	PS1
2013-05-08	56420.55	+9.66	22.76 ± 0.14	<i>ips1</i>	PS1
2013-05-10	56422.54	+11.40	22.31 ± 0.19	<i>ips1</i>	PS1
2013-05-16	56428.54	+16.64	22.43 ± 0.19	<i>ips1</i>	PS1
2013-05-20	56432.50	+20.11	22.47 ± 0.15	<i>ips1</i>	PS1
2013-06-04	56447.48	+33.21	22.92 ± 0.43	<i>ips1</i>	PS1
2013-06-12	56455.35	+40.09	22.36 ± 0.07	<i>ips1</i>	PS1
2013-06-19	56462.44	+46.28	23.37 ± 0.31	<i>ips1</i>	PS1
2013-06-27	56470.41	+53.25	22.84 ± 0.27	<i>ips1</i>	PS1
2013-06-30	56473.44	+55.90	22.59 ± 0.31	<i>ips1</i>	PS1
2013-07-03	56476.42	+58.50	22.68 ± 0.25	<i>ips1</i>	PS1
2013-07-06	56479.35	+61.06	22.33 ± 0.08	<i>ips1</i>	PS1
2013-07-08	56481.34	+62.81	22.61 ± 0.25	<i>ips1</i>	PS1
2013-07-14	56487.35	+68.05	22.75 ± 0.16	<i>ips1</i>	PS1
2013-07-18	56491.32	+71.53	23.02 ± 0.15	<i>ips1</i>	PS1
2013-08-04	56508.33	+86.40	22.81 ± 0.16	<i>ips1</i>	PS1
2013-08-09	56513.28	+90.72	23.55 ± 0.45	<i>ips1</i>	PS1
2013-08-12	56516.30	+93.36	22.92 ± 0.51	<i>ips1</i>	PS1
2013-09-03	56538.28	+112.57	23.39 ± 0.31	<i>ips1</i>	PS1
2013-04-28	56410.54	+0.91	22.28 ± 0.47	<i>zps1</i>	PS1
2013-04-30	56412.48	+2.61	22.56 ± 0.38	<i>zps1</i>	PS1
2013-05-03	56415.51	+5.26	22.21 ± 0.26	<i>zps1</i>	PS1
2013-05-17	56429.43	+17.43	22.49 ± 0.70	<i>zps1</i>	PS1
2013-05-30	56442.49	+28.84	22.47 ± 0.20	<i>zps1</i>	PS1
2013-06-10	56453.50	+38.46	22.26 ± 0.19	<i>zps1</i>	PS1
2013-06-16	56459.35	+43.58	22.46 ± 0.25	<i>zps1</i>	PS1
2013-06-18	56461.47	+45.43	22.50 ± 0.29	<i>zps1</i>	PS1
2013-06-20	56463.33	+47.06	22.61 ± 0.16	<i>zps1</i>	PS1
2013-06-26	56469.46	+52.42	22.37 ± 0.34	<i>zps1</i>	PS1
2013-07-01	56474.44	+56.77	22.48 ± 0.27	<i>zps1</i>	PS1
2013-07-04	56477.31	+59.28	22.89 ± 0.22	<i>zps1</i>	PS1
2013-07-07	56480.41	+61.99	22.68 ± 0.27	<i>zps1</i>	PS1
2013-07-09	56482.35	+63.68	21.67 ± 0.22	<i>zps1</i>	PS1
2013-07-15	56488.31	+68.90	22.70 ± 0.16	<i>zps1</i>	PS1
2013-07-17	56490.33	+70.66	22.88 ± 0.33	<i>zps1</i>	PS1
2013-07-19	56492.36	+72.43	22.48 ± 0.24	<i>zps1</i>	PS1
2013-07-25	56498.36	+77.68	22.41 ± 0.39	<i>zps1</i>	PS1
2013-08-02	56506.30	+84.62	22.58 ± 0.24	<i>zps1</i>	PS1
2013-08-07	56511.31	+89.00	22.80 ± 0.40	<i>zps1</i>	PS1

Table A.11: (continued)

Date	MJD	Rest frame epoch*	Magnitude	Filter	Telescope
2013-08-13	56517.30	+94.23	22.90 ± 0.26	z_{PS1}	PS1
2013-08-15	56519.27	+95.96	23.34 ± 0.48	z_{PS1}	PS1
2013-08-21	56525.29	+101.22	23.70 ± 0.54	z_{PS1}	PS1
2013-04-27	56409.49	+0.00	23.14 ± 0.99	y_{PS1}	PS1
2013-04-30	56412.51	+2.63	21.88 ± 0.59	y_{PS1}	PS1
2013-05-05	56417.54	+7.04	22.34 ± 0.72	y_{PS1}	PS1
2013-05-23	56435.49	+22.73	22.61 ± 0.75	y_{PS1}	PS1
2013-06-25	56468.40	+51.49	22.42 ± 0.67	y_{PS1}	PS1
2013-08-18	56522.29	+98.60	22.81 ± 0.56	y_{PS1}	PS1
2013-08-21	56525.32	+101.24	22.61 ± 0.60	y_{PS1}	PS1

The tabulated magnitudes are given “as observed”, i.e. neither corrected for dust extinction nor K -corrected. *Rest frame epochs (assuming a redshift of 0.144) with respect to the first detection on 56409.49 (MJD). PS1 = Panoramic Survey Telescope & Rapid Response System 1.

Table A.12: PS1-13baf: Journal of spectroscopic observations

Date	MJD	Epoch* rest frame	Wavelength range in Å	Resolution Å	Telescope+Instrument
2013-05-15	56428.20	+16.35	3750 - 9245	16.9	GTC+OSIRIS+R300B
2013-05-28	56441.18	+27.70	4500 - 9835	16.6	GTC+OSIRIS+R300B
2013-06-10	56454.09	+38.98	3800 - 9600	17.1	GTC+OSIRIS+R300B

*Rest frame epochs (assuming a redshift of 0.144) with respect to the first discovery on 56409.49 (MJD). The resolution was determined from the FWHM of the $O\alpha \lambda 5577.34$ sky line.

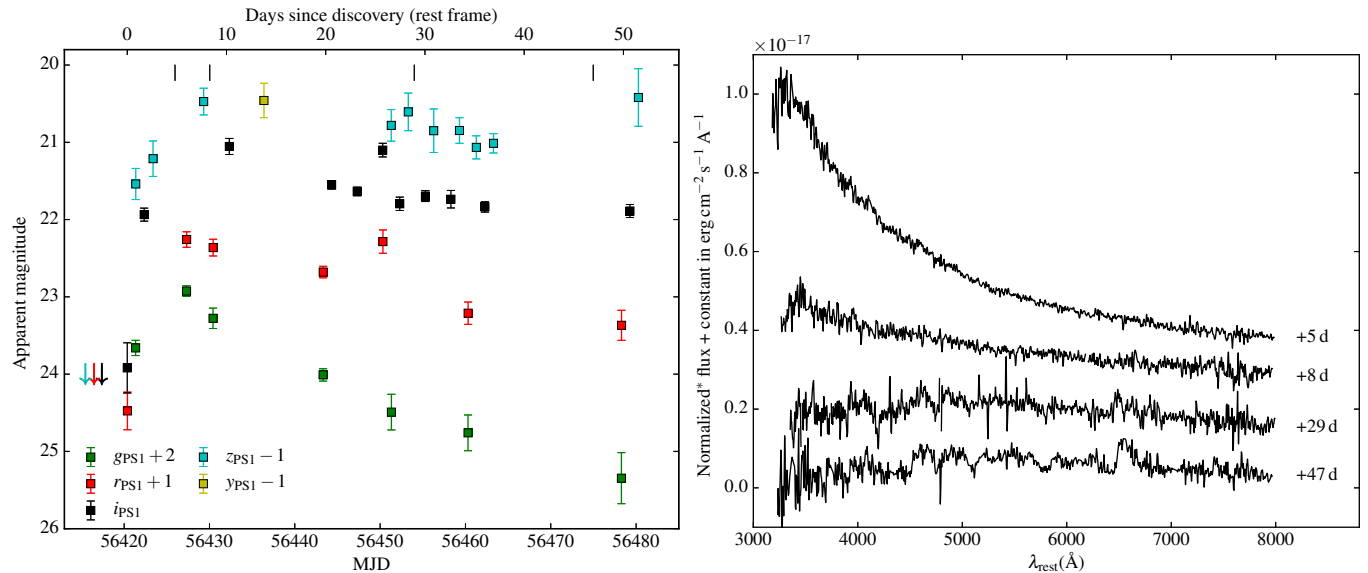


Fig. A.7: PS1-13bmf. Left panel: $grizy_{PS1}$ light curves of PS1-13bmf. The vertical ticks on the top mark the epochs of the observed spectra. Right panel: PS1-13bmf spectroscopy. *Flux normalized to the maximum $H\alpha$ flux for better visibility of the features. The exact normalizations are: flux/5.7 for the +5 d spectrum; flux/9.5 for +8 d; flux/8.8 for +29 d; flux/5.1 for +47 d.

Appendix A.10: PS1-13atm

PS1-13atm was discovered on 2013 April 14 by the PS1 MD survey. $g_{PS1}r_{PS1}i_{PS1}z_{PS1}y_{PS1}$ photometry was obtained in the course of the PS1 MD survey up to 22 d (rest frame) after the first detection. We additionally obtained a series of three GTC spectra ranging between +16 and +44 d (rest frame) after discovery.

Spectroscopic redshifts from the host galaxy were not available for PS1-13atm. The redshift of PS1-13atm was therefore determined by measuring the narrow $H\alpha$ component (presumably a

contamination from the host galaxy) in all spectra and averaging the respective results: $z = 0.220 \pm 0.001$.

Features attributable to the $Na\alpha$ doublet from interstellar gas either in the Milky Way or the host galaxy, are not apparent in the spectra of PS1-13atm. However, – as for PS1-13bmf – we refrain from giving a meaningless upper limit for the EW of the $Na\alpha$ blend or the host galaxy extinction due to the low signal-to-noise ratio of the spectra.

The light curves of PS1-13atm are presented in the left panel of Figure A.8. Table A.15 shows the log of imaging observa-

Table A.13: PS1-13bmf: Photometric observations

Date	MJD	Rest frame epoch*	Magnitude	Filter	Telescope
2013-05-09	56421.34	+0.84	21.66 ± 0.10	g_{PS1}	PS1
2013-05-15	56427.31	+5.97	20.92 ± 0.07	g_{PS1}	PS1
2013-05-18	56430.42	+8.64	21.28 ± 0.13	g_{PS1}	PS1
2013-05-31	56443.31	+19.73	22.01 ± 0.08	g_{PS1}	PS1
2013-06-08	56451.32	+26.62	22.49 ± 0.23	g_{PS1}	PS1
2013-06-17	56460.30	+34.34	22.76 ± 0.23	g_{PS1}	PS1
2013-07-05	56478.28	+49.80	23.35 ± 0.33	g_{PS1}	PS1
2013-05-08	56420.38	+0.02	23.48 ± 0.24	r_{PS1}	PS1
2013-05-15	56427.32	+5.98	21.26 ± 0.10	r_{PS1}	PS1
2013-05-18	56430.43	+8.65	21.36 ± 0.11	r_{PS1}	PS1
2013-05-31	56443.32	+19.74	21.68 ± 0.07	r_{PS1}	PS1
2013-06-07	56450.33	+25.77	21.29 ± 0.15	r_{PS1}	PS1
2013-06-17	56460.31	+34.35	22.21 ± 0.14	r_{PS1}	PS1
2013-07-05	56478.29	+49.81	22.37 ± 0.19	r_{PS1}	PS1
2013-05-08	56420.36	+0.00	23.92 ± 0.32	i_{PS1}	PS1
2013-05-10	56422.34	+1.70	21.94 ± 0.08	i_{PS1}	PS1
2013-05-20	56432.33	+10.29	21.05 ± 0.10	i_{PS1}	PS1
2013-06-01	56444.32	+20.60	21.55 ± 0.05	i_{PS1}	PS1
2013-06-04	56447.31	+23.17	21.64 ± 0.06	i_{PS1}	PS1
2013-06-07	56450.31	+25.75	21.10 ± 0.09	i_{PS1}	PS1
2013-06-09	56452.30	+27.46	21.80 ± 0.09	i_{PS1}	PS1
2013-06-12	56455.31	+30.04	21.70 ± 0.07	i_{PS1}	PS1
2013-06-15	56458.30	+32.62	21.74 ± 0.11	i_{PS1}	PS1
2013-06-19	56462.28	+36.04	21.84 ± 0.07	i_{PS1}	PS1
2013-07-06	56479.28	+50.66	21.89 ± 0.08	i_{PS1}	PS1
2013-05-09	56421.36	+0.86	22.54 ± 0.20	z_{PS1}	PS1
2013-05-11	56423.39	+2.60	22.21 ± 0.23	z_{PS1}	PS1
2013-05-17	56429.32	+7.70	21.47 ± 0.17	z_{PS1}	PS1
2013-06-08	56451.30	+26.60	21.78 ± 0.20	z_{PS1}	PS1
2013-06-10	56453.30	+28.32	21.61 ± 0.24	z_{PS1}	PS1
2013-06-13	56456.28	+30.88	21.85 ± 0.28	z_{PS1}	PS1
2013-06-16	56459.30	+33.48	21.85 ± 0.17	z_{PS1}	PS1
2013-06-18	56461.27	+35.18	22.07 ± 0.15	z_{PS1}	PS1
2013-06-20	56463.28	+36.90	22.01 ± 0.12	z_{PS1}	PS1
2013-07-07	56480.27	+51.51	21.42 ± 0.37	z_{PS1}	PS1
2013-05-24	56436.39	+13.78	21.46 ± 0.22	y_{PS1}	PS1

The tabulated magnitudes are given “as observed”, i.e. neither corrected for dust extinction nor K -corrected. *Rest frame epochs (assuming a redshift of 0.163) with respect to the first detection on 56420.36 (MJD). PS1 = Panoramic Survey Telescope & Rapid Response System 1.

Table A.14: PS1-13bmf: Journal of spectroscopic observations

Date	MJD	Epoch* rest frame	Wavelength range in Å	Resolution Å	Telescope+Instrument
2013-05-13	56425.96	+4.82	3700 - 9285	16.7	GTC+OSIRIS+R300B
2013-05-17	56430.03	+8.31	3800 - 9265	21.5	GTC+OSIRIS+R300B
2013-06-10	56454.00	+28.92	3900 - 9295	16.5	GTC+OSIRIS+R300B
2013-07-01	56474.97	+46.96	3760 - 9265	17.0	GTC+OSIRIS+R300B

*Rest frame epochs (assuming a redshift of 0.163) with respect to the first detection on 56420.36 (MJD). The resolution was determined from the FWHM of the $\text{O}_1 \lambda 5577.34$ sky line.

tions as well as the final calibrated magnitudes. PS1-13atm was discovered only one day after the last non-detection in the r_{PS1} -band on MJD 56395.29. This allows us to constrain the explosion epoch of PS1-13atm to MJD 56395.8 ± 0.5 . Unfortunately, the photometric coverage is rather sparse thereafter – in particular, the g_{PS1} - and r_{PS1} -band have only one data point – rendering a distinction between Type II-P or Type II-L rather difficult.

Table A.16 gives the journal of spectroscopic observations for PS1-13atm. The fully reduced and calibrated spectra of PS1-13atm are presented in the right panel of Figure A.8. They are corrected for galactic reddening and redshift ($z = 0.220$). The

spectra of PS1-13atm show clear features of $\text{H}\alpha$ and $\text{H}\beta$. The $\text{H}\alpha$ profile shows only a very weak absorption and is contaminated by narrow components presumably from the host galaxy. No lines of iron can be discerned in any of the spectra.

Appendix A.11: PS1-13bni

PS1-13bni was discovered on 2013 April 27 by the PS1 MD survey. g_{PS1} , r_{PS1} , i_{PS1} , z_{PS1} , y_{PS1} photometry was obtained in the course of the PS1 MD survey up to 99 d (rest frame) after the first de-

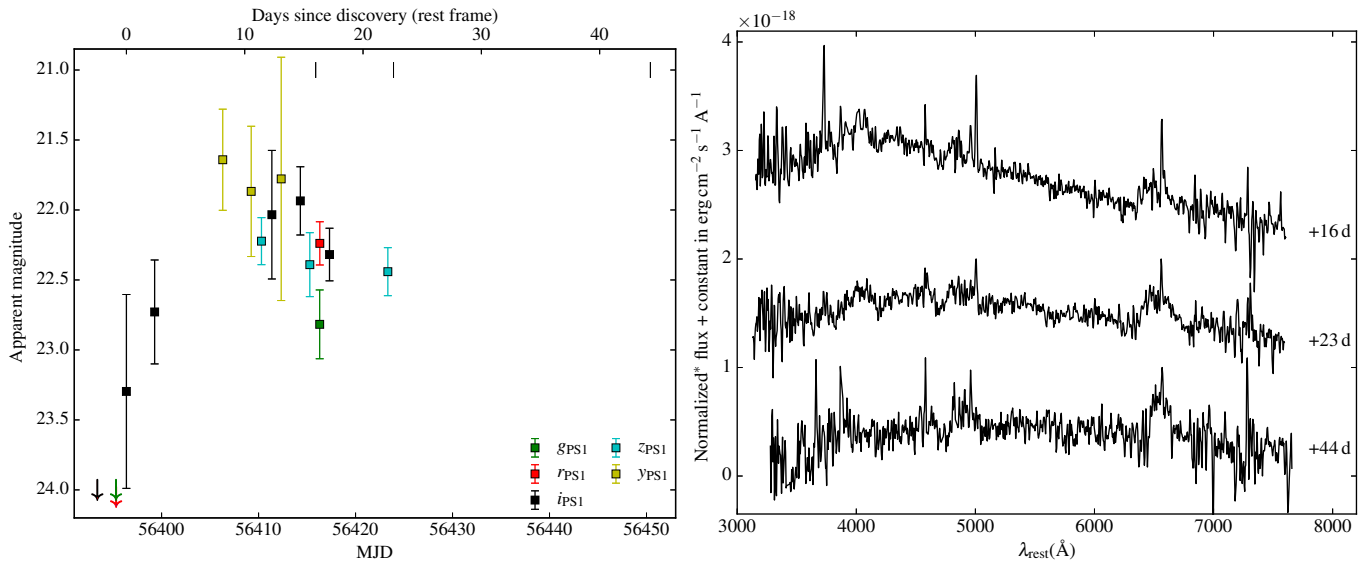


Fig. A.8: PS1-13atm. Left panel: $grizy_{\text{PS1}}$ light curves of PS1-13atm. The vertical ticks on the top mark the epochs of the observed spectra. Right panel: PS1-13atm spectroscopy. *Flux normalized to the maximum $\text{H}\alpha$ flux for better visibility of the features. The exact normalizations are: flux/4.3 for the +16 d spectrum; flux/6.1 for +23 d; flux/7.8 for +44 d.

Table A.15: PS1-13atm: Photometric observations

Date	MJD	Rest frame epoch*	Magnitude	Filter	Telescope
2013-05-04	56416.30	+16.34	22.82 ± 0.25	g_{PS1}	PS1
2013-05-04	56416.31	+16.35	22.24 ± 0.15	r_{PS1}	PS1
2013-04-14	56396.37	+0.00	23.30 ± 0.69	i_{PS1}	PS1
2013-04-17	56399.28	+2.39	22.73 ± 0.37	i_{PS1}	PS1
2013-04-29	56411.37	+12.29	22.03 ± 0.46	i_{PS1}	PS1
2013-05-02	56414.31	+14.70	21.93 ± 0.24	i_{PS1}	PS1
2013-05-05	56417.32	+17.17	22.32 ± 0.19	i_{PS1}	PS1
2013-04-28	56410.30	+11.42	22.22 ± 0.17	z_{PS1}	PS1
2013-05-03	56415.28	+15.50	22.39 ± 0.23	z_{PS1}	PS1
2013-05-11	56423.33	+22.10	22.44 ± 0.17	z_{PS1}	PS1
2013-04-24	56406.31	+8.14	21.64 ± 0.36	y_{PS1}	PS1
2013-04-27	56409.24	+10.55	21.87 ± 0.47	y_{PS1}	PS1
2013-04-30	56412.33	+13.08	21.78 ± 0.87	y_{PS1}	PS1

The tabulated magnitudes are given “as observed”, i.e. neither corrected for dust extinction nor K -corrected. *Rest frame epochs (assuming a redshift of 0.220) with respect to the first detection on 56396.37 (MJD). PS1 = Panoramic Survey Telescope & Rapid Response System 1.

Table A.16: PS1-13atm: Journal of spectroscopic observations

Date	MJD	Epoch* rest frame	Wavelength range in Å	Resolution Å	Telescope+Instrument
2013-05-03	56415.89	+16.00	3850 - 9280	17.0	GTC+OSIRIS+R300B
2013-05-11	56423.91	+22.58	3820 - 9265	16.8	GTC+OSIRIS+R300B
2013-06-07	56450.40	+44.29	4000 - 9415	16.8	GTC+OSIRIS+R300B

*Rest frame epochs (assuming a redshift of 0.220) with respect to the first detection on 56396.37 (MJD). The resolution was determined from the FWHM of the $\text{O I } \lambda 5577.34$ sky line.

tection. We additionally obtained a series of five GTC spectra ranging between +14 and +51 d (rest frame) after discovery.

PS1-13bni displays neither narrow emissions reminiscent of the host galaxy nor is a spectroscopic redshift for its host galaxies available in a public data base. With the objective of estimating the redshift of PS1-13bni, we performed a series of cross correlations using SNID (Blondin & Tonry 2007). Suggested matches were scrutinized and the selected results span

a range of redshifts between 0.323 and 0.344 with a median of 0.335. We therefore adopt this values as the redshift of the SN, and give the range in redshifts mentioned above as a conservative estimate of its uncertainty: $z = 0.335^{+0.009}_{-0.012}$.

Features attributable to the Na I doublet from interstellar gas either in the Milky Way or the host galaxy, are not apparent in the spectra of PS1-13bni. However, – as for PS1-13bmf – we refrain from giving a meaningless upper limit for the EW of the Na I D

blend or the host galaxy extinction due to the low signal-to-noise ratio of the spectra.

The light curves of PS1-13bni are presented in the left panel of Figure A.9. Table A.17 shows the log of imaging observations as well as the final calibrated magnitudes. The light curves of PS1-13bni decline at rates of 0.64 ± 0.40 mag/50 d in the r_{PS1} -band, 0.29 ± 0.50 mag/50 d in the i_{PS1} -band, and 0.28 ± 0.35 mag/50 d in the z_{PS1} -band. While PS1-13bni is likely a Type II-P SNe, the relatively large uncertainties in the decline rates, stemming from similarly uncertain photometry make it difficult to clearly classify PS1-13bni as either a Type II-P or II-L SN.

Table A.18 gives the journal of spectroscopic observations for PS1-13bni. The fully reduced and calibrated spectra of PS1-13bni are presented in the right panel of Figure A.9. They are corrected for galactic reddening and redshift ($z = 0.335$). The spectra of PS1-13bni show clear features of $\text{H}\beta$ become more prominent as time elapses. Unfortunately, the $\text{H}\alpha$ falls onto the border region of the spectrum with poor sensitivity of the detector, due to the high redshift of $z = 0.335$ of PS1-13bni. Lines of iron cannot be discerned in any of the spectra.

Appendix B: Additional Tables

Appendix B.1: Temperature evolution

Table B.1 shows the rest frame photometry, interpolated to the times of spectral observations and temperature evolution for each SN (see Section 3.3).

Appendix B.2: Fit parameters for Equation 1

Table B.2 gives the fit parameters that represent the velocity evolution of the SNe 1999em, 1999gi, 2004et, 2005cs and 2006bp following Equation 1 for the $\text{H}\alpha$, $\text{H}\beta$ and $\text{Fe II } \lambda 5169$ lines.

Appendix B.3: EPM quantities

Table B.3 gives the derived EPM quantities for each SN that are used to perform the distance fits (see Section 3.5 and Table 4).

Appendix C: EPM fits of individual SNe

Figures C.1-C.8 show the fits through χ for the B , V , and I filters to determine the distance and – when unknown – the time of explosion of SNe 2013ca, LSQ13cuw, PS1-13wr, PS1-12bku, PS1-13abg, PS1-13baf, PS1-13bmf, and PS1-13bni. The fit was performed twice for each SN using the dilution factors as given either by Hamuy et al. (2001) or Dessart & Hillier (2005). The distance of SN 2013eq was adopted from Gall et al. (2016) and the corresponding fit is illustrated in their Figure 4. The fit for PS1-14vk is presented in Section 3.5.

Table A.17: PS1-13bni: Photometric observations

Date	MJD	Rest frame epoch*	Magnitude	Filter	Telescope
2013-05-04	56416.54	+5.28	23.12 ± 0.19	<i>gps1</i>	PS1
2013-05-09	56421.55	+9.03	22.93 ± 0.17	<i>gps1</i>	PS1
2013-05-12	56424.55	+11.28	22.90 ± 0.25	<i>gps1</i>	PS1
2013-05-15	56427.45	+13.45	23.42 ± 0.60	<i>gps1</i>	PS1
2013-05-31	56443.46	+25.44	23.27 ± 0.47	<i>gps1</i>	PS1
2013-06-08	56451.45	+31.43	23.78 ± 0.85	<i>gps1</i>	PS1
2013-07-02	56475.43	+49.39	24.80 ± 0.50	<i>gps1</i>	PS1
2013-05-04	56416.55	+5.29	23.05 ± 0.23	<i>rps1</i>	PS1
2013-05-08	56420.57	+8.29	23.06 ± 0.22	<i>rps1</i>	PS1
2013-05-12	56424.56	+11.29	22.81 ± 0.17	<i>rps1</i>	PS1
2013-05-15	56427.46	+13.46	22.91 ± 0.34	<i>rps1</i>	PS1
2013-05-31	56443.48	+25.45	23.04 ± 0.48	<i>rps1</i>	PS1
2013-06-07	56450.52	+30.73	23.93 ± 0.99	<i>rps1</i>	PS1
2013-06-17	56460.46	+38.17	23.32 ± 0.37	<i>rps1</i>	PS1
2013-06-29	56472.43	+47.15	23.36 ± 0.54	<i>rps1</i>	PS1
2013-07-02	56475.44	+49.40	23.65 ± 0.21	<i>rps1</i>	PS1
2013-07-05	56478.35	+51.58	23.50 ± 0.51	<i>rps1</i>	PS1
2013-07-06	56479.37	+52.34	24.01 ± 0.38	<i>rps1</i>	PS1
2013-07-13	56486.34	+57.57	24.18 ± 0.64	<i>rps1</i>	PS1
2013-07-28	56501.41	+68.85	23.96 ± 0.92	<i>rps1</i>	PS1
2013-08-03	56507.31	+73.27	23.82 ± 0.64	<i>rps1</i>	PS1
2013-08-04	56508.31	+74.02	24.34 ± 0.64	<i>rps1</i>	PS1
2013-04-29	56411.52	+1.52	23.24 ± 0.52	<i>ips1</i>	PS1
2013-05-02	56414.52	+3.77	23.22 ± 0.24	<i>ips1</i>	PS1
2013-05-05	56417.58	+6.06	22.60 ± 0.42	<i>ips1</i>	PS1
2013-05-08	56420.55	+8.28	23.03 ± 0.15	<i>ips1</i>	PS1
2013-05-10	56422.54	+9.77	22.74 ± 0.27	<i>ips1</i>	PS1
2013-05-16	56428.54	+14.26	22.82 ± 0.35	<i>ips1</i>	PS1
2013-05-20	56432.50	+17.23	22.75 ± 0.18	<i>ips1</i>	PS1
2013-06-04	56447.48	+28.45	22.89 ± 0.37	<i>ips1</i>	PS1
2013-06-07	56450.50	+30.72	22.81 ± 0.39	<i>ips1</i>	PS1
2013-06-09	56452.45	+32.18	22.98 ± 0.54	<i>ips1</i>	PS1
2013-06-12	56455.35	+34.35	23.12 ± 0.18	<i>ips1</i>	PS1
2013-06-15	56458.41	+36.64	22.65 ± 0.43	<i>ips1</i>	PS1
2013-06-19	56462.44	+39.66	23.45 ± 0.31	<i>ips1</i>	PS1
2013-06-27	56470.41	+45.63	23.77 ± 0.67	<i>ips1</i>	PS1
2013-06-30	56473.44	+47.90	23.29 ± 0.32	<i>ips1</i>	PS1
2013-07-03	56476.42	+50.13	23.47 ± 0.51	<i>ips1</i>	PS1
2013-07-06	56479.35	+52.32	23.37 ± 0.23	<i>ips1</i>	PS1
2013-07-08	56481.34	+53.82	23.25 ± 0.62	<i>ips1</i>	PS1
2013-07-14	56487.35	+58.32	23.46 ± 0.38	<i>ips1</i>	PS1
2013-07-18	56491.32	+61.29	23.86 ± 0.37	<i>ips1</i>	PS1
2013-07-29	56502.32	+69.53	23.28 ± 0.33	<i>ips1</i>	PS1
2013-08-04	56508.33	+74.04	23.64 ± 0.32	<i>ips1</i>	PS1
2013-08-09	56513.28	+77.74	23.59 ± 0.34	<i>ips1</i>	PS1
2013-08-16	56520.31	+83.01	23.20 ± 0.47	<i>ips1</i>	PS1
2013-09-03	56538.28	+96.47	24.06 ± 0.52	<i>ips1</i>	PS1
2013-04-28	56410.54	+0.78	22.72 ± 0.88	<i>zps1</i>	PS1
2013-04-30	56412.48	+2.23	23.10 ± 0.62	<i>zps1</i>	PS1
2013-05-03	56415.51	+4.51	22.77 ± 0.36	<i>zps1</i>	PS1
2013-05-09	56421.53	+9.02	22.57 ± 0.20	<i>zps1</i>	PS1
2013-05-25	56437.49	+20.97	20.73 ± 0.36	<i>zps1</i>	PS1
2013-05-30	56442.49	+24.71	22.85 ± 0.29	<i>zps1</i>	PS1
2013-06-10	56453.50	+32.96	22.88 ± 0.34	<i>zps1</i>	PS1
2013-06-16	56459.35	+37.34	22.77 ± 0.25	<i>zps1</i>	PS1
2013-06-18	56461.47	+38.93	22.86 ± 0.42	<i>zps1</i>	PS1
2013-06-20	56463.33	+40.33	23.45 ± 0.45	<i>zps1</i>	PS1
2013-06-28	56471.43	+46.39	22.17 ± 0.48	<i>zps1</i>	PS1
2013-07-01	56474.44	+48.65	22.97 ± 0.39	<i>zps1</i>	PS1
2013-07-04	56477.31	+50.80	23.18 ± 0.31	<i>zps1</i>	PS1
2013-07-07	56480.41	+53.12	22.93 ± 0.31	<i>zps1</i>	PS1
2013-07-09	56482.35	+54.57	23.20 ± 0.76	<i>zps1</i>	PS1
2013-07-15	56488.31	+59.04	22.96 ± 0.31	<i>zps1</i>	PS1
2013-07-17	56490.33	+60.55	23.54 ± 0.77	<i>zps1</i>	PS1
2013-07-19	56492.36	+62.07	23.24 ± 0.43	<i>zps1</i>	PS1
2013-08-02	56506.30	+72.51	22.99 ± 0.37	<i>zps1</i>	PS1

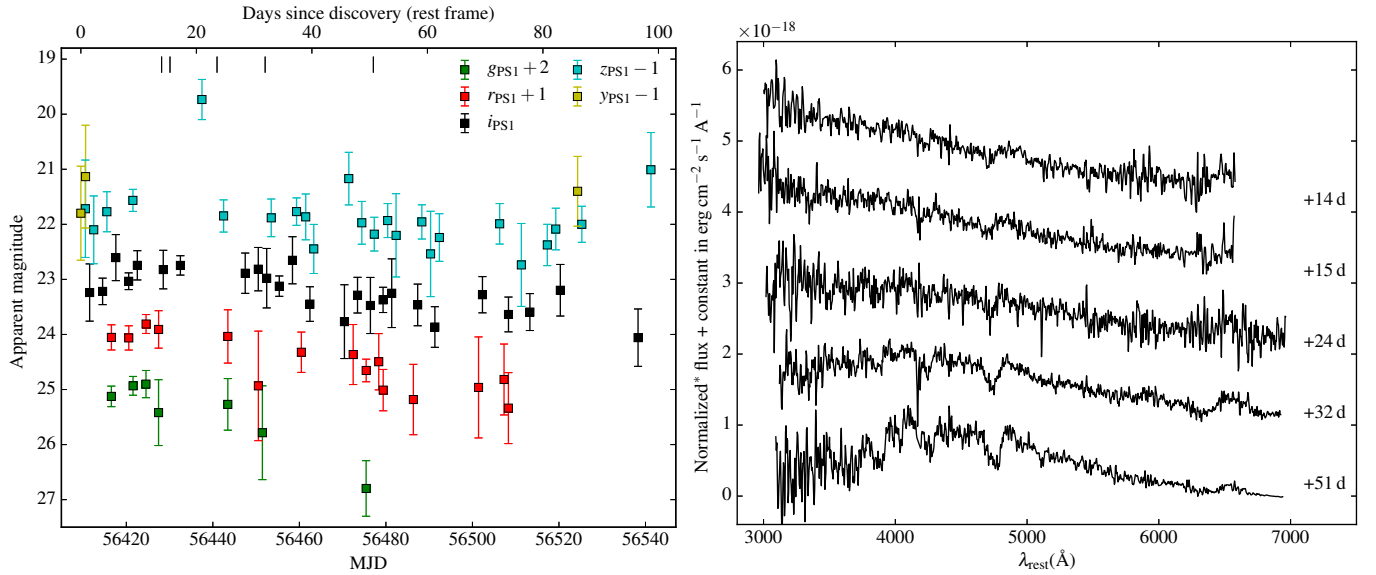


Fig. A.9: PS1-13bni. Left panel: $grizy_{PS1}$ light curves of PS1-13bni. The vertical ticks on the top mark the epochs of the observed spectra. Right panel: PS1-13bni spectroscopy. *Flux normalized to the maximum $H\alpha$ flux for better visibility of the features. The exact normalizations are: flux/2.5 for the +14 d spectrum; flux/2.5 for +15 d; flux/2.5 for +24 d; flux/2.2 for +32 d; flux/2.1 for +51 d.

Table A.17: (continued)

Date	MJD	Rest frame epoch*	Magnitude	Filter	Telescope
2013-08-07	56511.31	+76.26	23.74 ± 0.75	z_{PS1}	PS1
2013-08-13	56517.30	+80.75	23.38 ± 0.38	z_{PS1}	PS1
2013-08-15	56519.27	+82.23	23.09 ± 0.38	z_{PS1}	PS1
2013-08-21	56525.29	+86.74	23.00 ± 0.33	z_{PS1}	PS1
2013-09-06	56541.27	+98.71	22.01 ± 0.68	z_{PS1}	PS1
2013-04-27	56409.49	+0.00	22.80 ± 0.85	y_{PS1}	PS1
2013-04-28	56410.58	+0.81	22.13 ± 0.93	y_{PS1}	PS1
2013-08-20	56524.31	+86.01	22.40 ± 0.63	y_{PS1}	PS1

The tabulated magnitudes are given “as observed”, i.e. neither corrected for dust extinction nor K -corrected. *Rest frame epochs (assuming a redshift of 0.335) with respect to the date of discovery on 56409.49 (MJD). PS1 = Panoramic Survey Telescope & Rapid Response System 1.

Table A.18: PS1-13bni: Journal of spectroscopic observations

Date	MJD	Epoch* rest frame	Wavelength range in Å	Resolution Å	Telescope+Instrument
2013-05-15	56428.16	+13.98	3800 - 9245	21.3	GTC+OSIRIS+R300B
2013-05-17	56430.10	+15.43	3800 - 9245	21.4	GTC+OSIRIS+R300B
2013-05-28	56440.97	+23.58	4030 - 9295	21.3	GTC+OSIRIS+R300B
2013-06-08	56452.09	+31.90	3750 - 9245	21.6	GTC+OSIRIS+R300B
2013-07-03	56477.09	+50.63	3870 - 9265	21.5	GTC+OSIRIS+R300B

*Rest frame epochs (assuming a redshift of 0.335) with respect to the first detection on 56409.49 (MJD). The resolution was determined from the FWHM of the $O\alpha \lambda 5577.34$ sky line.

Table B.1: Interpolated rest frame photometry and temperature evolution

SN	Date	MJD	Epoch* rest frame (d)	B^{**} mag	V^{**} mag	I^{**} mag	$T_{\star,BVI}$ K
SN 2013ca	2013-05-10	56422.97	+29.63	19.27 ± 0.11	18.88 ± 0.06	18.41 ± 0.15	7279 ± 557
	2013-05-15	56428.02	+34.46	19.43 ± 0.11	18.92 ± 0.06	18.43 ± 0.15	6744 ± 454
	2013-05-27	56439.99	+45.92	19.77 ± 0.12	19.05 ± 0.07	18.58 ± 0.14	6108 ± 331
	2013-06-11	56454.91	+60.20	20.26 ± 0.14	19.19 ± 0.08	18.62 ± 0.13	5286 ± 207
LSQ13cuw	2013-11-24	56620.08	+25.49	19.49 ± 0.12	19.09 ± 0.09	18.55 ± 0.09	7067 ± 524
	2013-11-26	56622.21	+27.53	19.62 ± 0.12	19.27 ± 0.09	18.68 ± 0.11	7195 ± 584
	2013-12-01	56627.22	+32.32	19.96 ± 0.12	19.60 ± 0.09	19.04 ± 0.09	7245 ± 575
	2013-12-22	56648.15	+52.33	21.08 ± 0.12	20.62 ± 0.09	20.04 ± 0.09	6734 ± 448
	2014-01-24	56681.13	+83.86	22.29 ± 0.12	21.30 ± 0.09	21.00 ± 0.09	5751 ± 205
PS1-13wr	2013-03-11	56362.26	+11.77	21.59 ± 0.25	20.90 ± 0.16	20.23 ± 0.12	5856 ± 573
	2013-03-17	56369.12	+18.14	21.69 ± 0.25	20.94 ± 0.16	20.24 ± 0.12	5653 ± 501
	2013-03-25	56376.23	+24.74	21.78 ± 0.25	20.96 ± 0.16	20.24 ± 0.12	5477 ± 440
	2013-04-11	56394.15	+41.40	22.00 ± 0.25	21.03 ± 0.16	20.23 ± 0.12	5111 ± 338
PS1-14vk	2014-03-26	56743.15	+2.44	20.32 ± 0.05	20.03 ± 0.12	19.96 ± 0.15	8865 ± 732
	2014-04-04	56752.03	+10.66	20.60 ± 0.05	20.31 ± 0.12	20.20 ± 0.15	8787 ± 718
	2014-04-08	56755.91	+14.26	20.72 ± 0.05	20.40 ± 0.12	20.32 ± 0.15	8645 ± 681
	2014-04-21	56769.13	+26.50	21.68 ± 0.21	20.84 ± 0.12	20.56 ± 0.15	6090 ± 398
	2014-04-28	56775.93	+32.79	22.09 ± 0.21	21.03 ± 0.12	20.59 ± 0.15	5472 ± 315
	2014-05-16	56793.93	+49.46	22.77 ± 0.21	21.43 ± 0.12	20.99 ± 0.15	5106 ± 222
PS1-12bku	2012-09-16	56186.01	+22.66	20.33 ± 0.09	20.32 ± 0.07	20.01 ± 0.06	11479 ± 1556
	2012-09-20	56190.90	+27.15	20.50 ± 0.09	20.37 ± 0.07	20.06 ± 0.06	9668 ± 3485
	2012-10-05	56205.94	+40.98	21.00 ± 0.09	20.51 ± 0.07	20.10 ± 0.06	6990 ± 342
	2012-11-17	56249.92	+81.40	21.99 ± 0.09	20.58 ± 0.09	20.39 ± 0.07	5288 ± 95
PS1-13abg	2013-04-05	56388.06	+6.85	21.89 ± 0.05	21.85 ± 0.07	21.25 ± 0.09	9503 ± 2939
	2013-05-03	56415.93	+31.66	22.86 ± 0.05	22.10 ± 0.07	21.18 ± 0.09	5265 ± 150
	2013-05-17	56429.93	+44.13	23.35 ± 0.05	22.21 ± 0.07	21.10 ± 0.09	4481 ± 108
PS1-13baf	2013-05-15	56428.20	+16.35	23.15 ± 0.21	22.84 ± 0.22	22.12 ± 0.12	7073 ± 2439
	2013-05-28	56441.18	+27.70	23.26 ± 0.21	22.91 ± 0.22	22.20 ± 0.12	6931 ± 2072
	2013-06-10	56454.09	+38.98	23.36 ± 0.21	22.98 ± 0.22	22.29 ± 0.12	6801 ± 1981
PS1-13bmf	2013-05-13	56425.96	+4.82	21.21 ± 0.04	21.60 ± 0.06	21.66 ± 0.11	108139 ± 31530
	2013-05-17	56430.03	+8.31	21.44 ± 0.04	21.48 ± 0.06	21.22 ± 0.11	12607 ± 1221
	2013-06-10	56454.00	+28.92	22.54 ± 0.04	22.14 ± 0.06	21.68 ± 0.11	7280 ± 347
	2013-07-01	56474.97	+46.96	23.20 ± 0.04	22.45 ± 0.06	21.79 ± 0.11	5727 ± 157
PS1-13bni	2013-05-15	56428.16	+13.98	23.30 ± 0.20	23.17 ± 0.25	22.93 ± 0.20	10036 ± 2359
	2013-05-17	56430.10	+15.43	23.34 ± 0.20	23.17 ± 0.25	22.96 ± 0.20	9655 ± 2595
	2013-05-28	56440.97	+23.58	23.55 ± 0.20	23.23 ± 0.25	23.08 ± 0.20	8459 ± 2302
	2013-06-08	56452.09	+31.90	23.76 ± 0.20	23.32 ± 0.25	23.15 ± 0.20	7690 ± 1515
	2013-07-03	56477.09	+50.63	24.20 ± 0.20	23.41 ± 0.25	23.13 ± 0.19	6208 ± 602

*Epoch relative to discovery in the SN rest frame. **Magnitudes in the Johnson-Cousins Filter System, K -corrected and amended for dust extinction.

Table B.2: Fit parameters for the H α , H β and Fe II $\lambda 5169$ velocity evolutions

SN	Line	a in 1000 km s $^{-1}$	b in 0.01 d $^{-1}$	c in 1000 km s $^{-1}$	RMSE in km s $^{-1}$
SN 1999em	H α	11.25	1.67	0.41	290
	H β	10.34	2.97	1.45	222
	Fe II $\lambda 5169$	7.40	3.27	2.29	355
SN 1999gi	H α	13.82	2.08	1.17	199
	H β	11.68	2.52	1.39	56
	Fe II $\lambda 5169$	8.48	3.43	2.92	64
SN 2004et	H α	6.61	1.18	3.59	139
	H β	7.47	2.12	3.54	128
	Fe II $\lambda 5169$	8.46	3.32	2.50	126
SN 2005cs	H α	9.36	1.78	-1.58	354
	H β	8.22	3.10	-0.46	182
	Fe II $\lambda 5169$	6.69	6.62	1.54	266
SN 2006bp	H α	8.18	4.70	8.00	270
	H β	10.15	4.71	6.03	320
	Fe II $\lambda 5169$	13.21	5.80	4.76	107

Fit parameters for the H α , H β and Fe II $\lambda 5169$ velocity evolutions. RMSE = root mean square error.

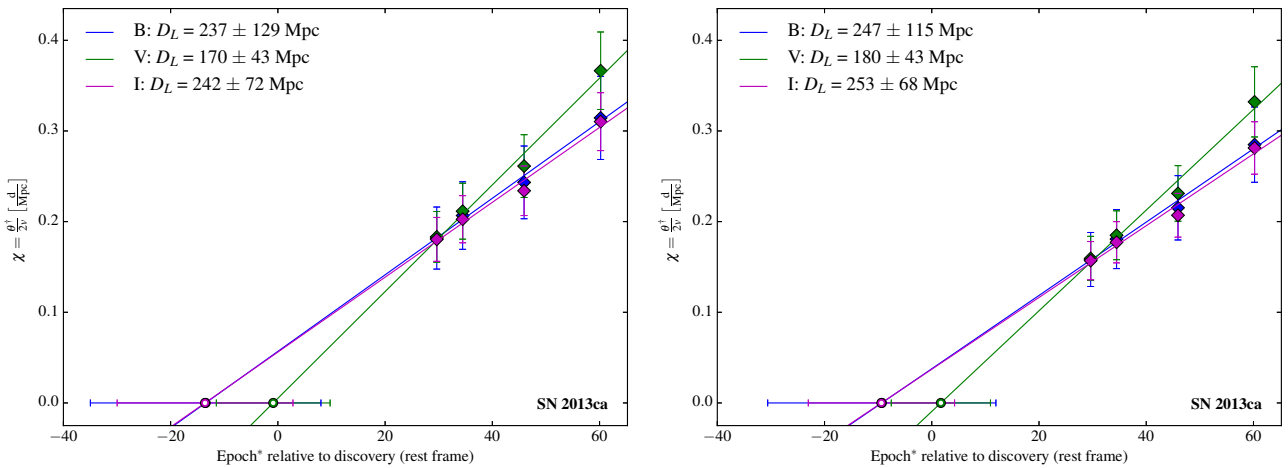


Fig. C.1: Distance fit for SN 2013ca using ζ_{BVI} as given in Hamuy et al. (2001) (left panel) and Dessart & Hillier (2005) (right panel). The diamond markers denote values of χ through which the fit is made.

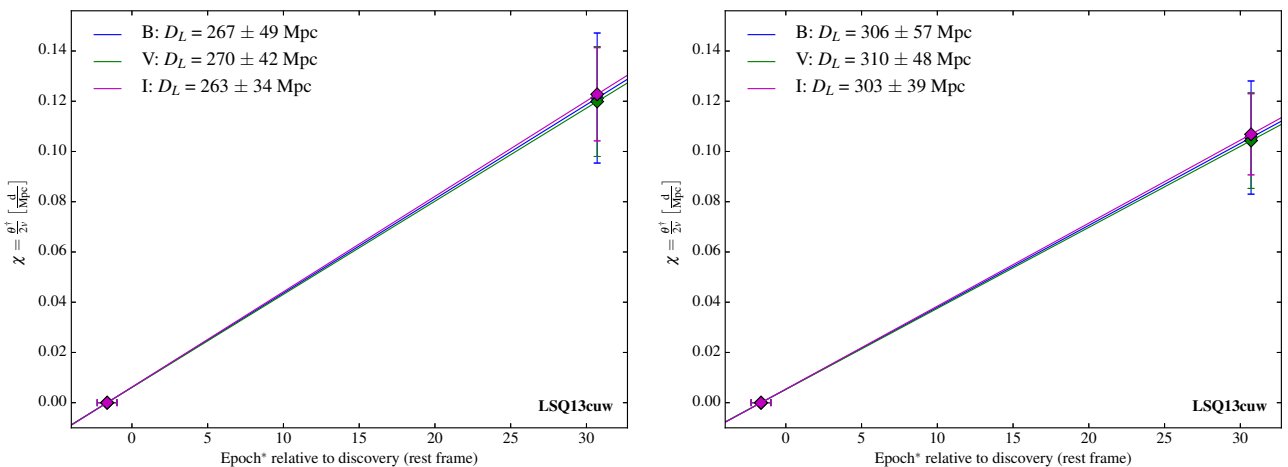


Fig. C.2: Distance fit for LSQ13cuw using ζ_{BVI} as given in Hamuy et al. (2001) (left panel) and Dessart & Hillier (2005) (right panel). The diamond markers denote values of χ through which the fit is made.

Table B.3: EPM quantities for the SNe in our sample

SN	Epoch* rest frame (d)	Velocity km s ⁻¹	Estimate of velocity via	$\theta_B^\dagger \times 10^{12}$	$\theta_V^\dagger \times 10^{12}$	$\theta_I^\dagger \times 10^{12}$	Dilution factor ζ_{BVI}	reference
SN 2013ca	+29.63	6245 \pm 312	Fe II λ 5169	6.4 \pm 1.2	6.4 \pm 0.9	6.3 \pm 0.8	0.49	H01
	+34.46	5885 \pm 294		5.5 \pm 1.0	5.6 \pm 0.8	5.5 \pm 0.7	0.64	D05
	+45.92	5167 \pm 258		6.8 \pm 1.2	7.0 \pm 1.0	6.7 \pm 0.8	0.53	H01
	+60.20	4314 \pm 216		6.0 \pm 1.0	6.1 \pm 0.8	5.8 \pm 0.7	0.69	D05
				7.0 \pm 1.1	7.6 \pm 0.9	6.8 \pm 0.7	0.60	H01
LSQ13cuw	+32.34	6873 \pm 674	H β	6.2 \pm 1.0	6.7 \pm 0.9	6.0 \pm 0.6	0.77	D05
				6.2 \pm 1.0	6.7 \pm 0.8	6.0 \pm 0.6	0.76	H01
PS1-13wr	+11.77	5786 \pm 289	Fe II λ 5169	7.6 \pm 1.0	8.9 \pm 0.9	7.5 \pm 0.7	0.76	D05
	+18.14	5528 \pm 276		6.9 \pm 0.9	8.0 \pm 0.8	6.8 \pm 0.6	0.92	H01
	+24.74	4800 \pm 240		7.6 \pm 1.0	8.9 \pm 0.9	7.5 \pm 0.7	0.76	H01
	+41.40	3450 \pm 173		6.9 \pm 0.9	8.0 \pm 0.8	6.8 \pm 0.6	0.92	D05
				7.6 \pm 1.0	8.9 \pm 0.9	7.5 \pm 0.7	0.76	H01
PS1-14vk	+10.66	6417 \pm 321	Fe II λ 5169	2.5 \pm 0.4	2.6 \pm 0.4	2.3 \pm 0.3	0.43	H01
	+26.50	5348 \pm 267		2.2 \pm 0.3	2.2 \pm 0.3	2.0 \pm 0.2	0.56	D05
	+32.79	4882 \pm 244		2.9 \pm 0.6	3.3 \pm 0.5	2.7 \pm 0.3	0.60	H01
	+49.46	4507 \pm 225		2.6 \pm 0.5	3.0 \pm 0.5	2.4 \pm 0.3	0.77	D05
				3.0 \pm 0.6	3.6 \pm 0.5	2.9 \pm 0.4	0.71	H01
PS1-12bku	+22.66	6050 \pm 303	Fe II λ 5169	2.7 \pm 0.4	3.2 \pm 0.3	2.6 \pm 0.3	0.88	D05
	+27.15	5619 \pm 281		2.2 \pm 1.4	2.2 \pm 1.1	2.3 \pm 0.9	0.42	H01
	+40.98	4700 \pm 235		1.9 \pm 1.2	1.9 \pm 1.0	2.0 \pm 0.8	0.54	D05
PS1-13abg	+44.13	4733 \pm 237	Fe II λ 5169	2.4 \pm 0.4	3.0 \pm 0.4	2.6 \pm 0.3	0.67	H01
				2.4 \pm 0.4	3.0 \pm 0.4	2.4 \pm 0.2	0.97	D05
PS1-13baf	+16.35	6762 \pm 423	H β	1.8 \pm 0.4	1.8 \pm 0.3	1.9 \pm 0.3	0.41	H01
	+27.70	5103 \pm 417		1.6 \pm 0.3	1.6 \pm 0.3	1.7 \pm 0.2	0.51	D05
	+28.92	6194 \pm 310		2.2 \pm 1.4	2.2 \pm 1.1	2.3 \pm 0.9	0.42	H01
	+46.96	3385 \pm 169		1.9 \pm 1.2	1.9 \pm 1.0	2.0 \pm 0.8	0.54	D05
PS1-13bmf	+15.43	8795 \pm 562	H β	3.1 \pm 0.4	3.2 \pm 0.3	3.0 \pm 0.2	0.51	H01
	+23.58	7146 \pm 604		2.7 \pm 0.3	2.8 \pm 0.3	2.6 \pm 0.2	0.67	D05
	+28.92	6194 \pm 310		1.4 \pm 0.2	1.4 \pm 0.1	1.4 \pm 0.1	0.49	H01
	+46.96	3385 \pm 169		1.2 \pm 0.1	1.2 \pm 0.1	1.2 \pm 0.1	0.64	D05
PS1-13bni	+15.43	8795 \pm 562	H β	1.6 \pm 0.1	1.7 \pm 0.1	1.6 \pm 0.1	0.66	H01
	+23.58	7146 \pm 604		1.5 \pm 0.1	1.6 \pm 0.1	1.4 \pm 0.1	0.83	D05
	+28.92	6194 \pm 310		0.6 \pm 0.3	0.6 \pm 0.2	0.6 \pm 0.2	0.42	H01

*Epoch in SN rest frame. H01 = Hamuy et al. (2001); D05 = Dessart & Hillier (2005).

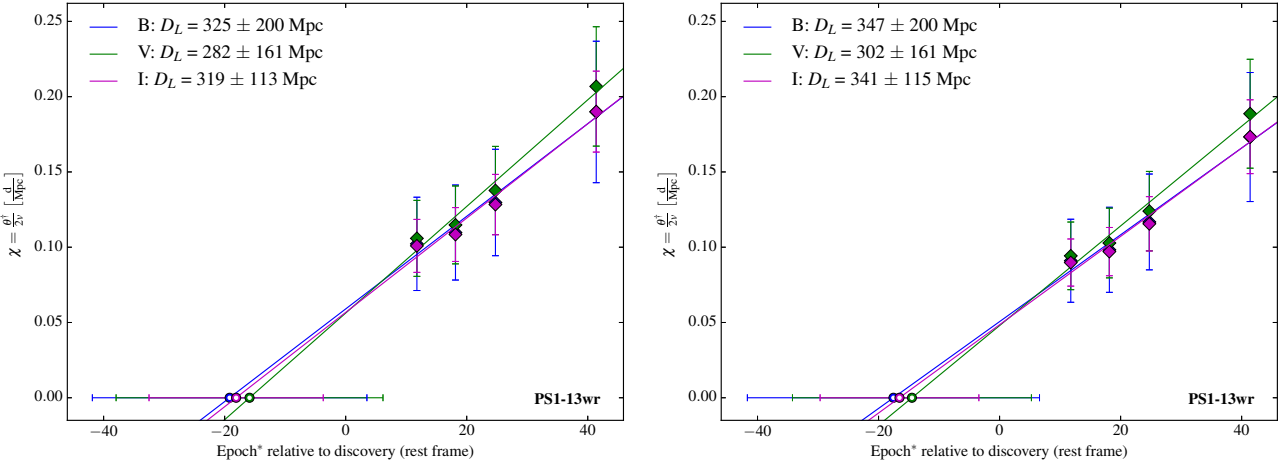


Fig. C.3: Distance fit for PS1-13wr using ζ_{BVI} as given in Hamuy et al. (2001) (left panel) and Dessart & Hillier (2005) (right panel). The diamond markers denote values of χ through which the fit is made.

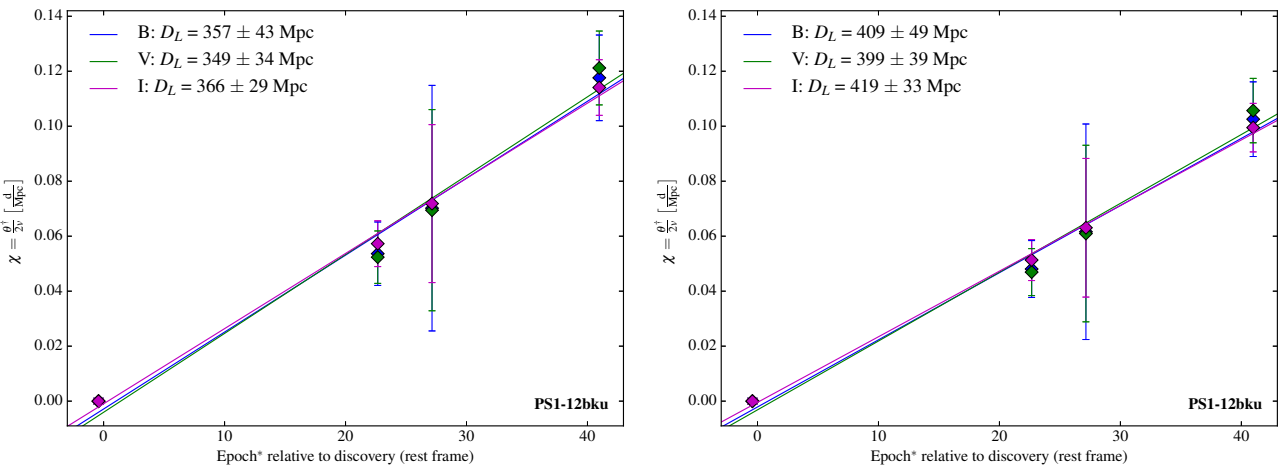


Fig. C.4: Distance fit for PS1-12bku using ζ_{BVI} as given in Hamuy et al. (2001) (left panel) and Dessart & Hillier (2005) (right panel). The diamond markers denote values of χ through which the fit is made.

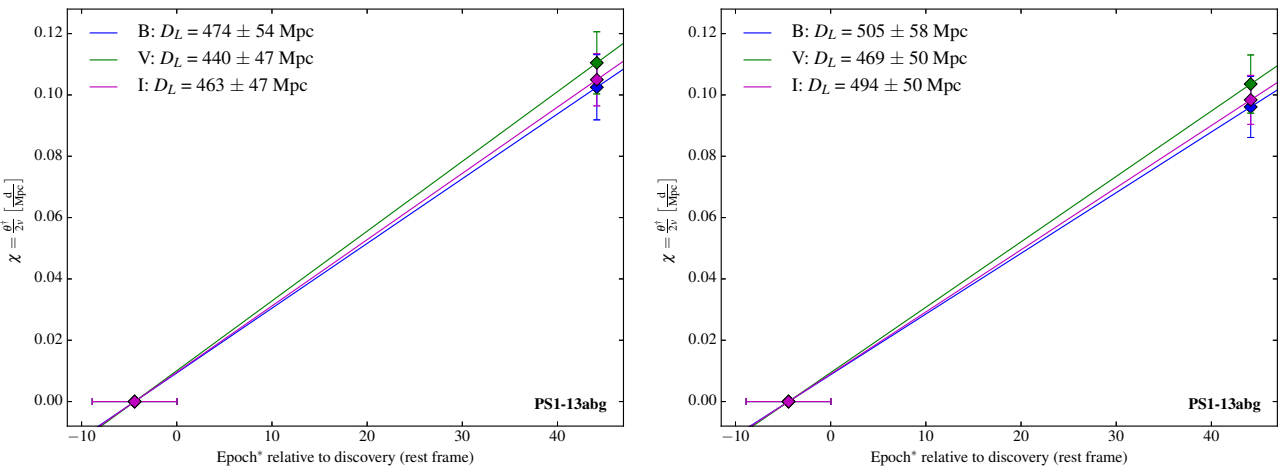


Fig. C.5: Distance fit for PS1-13abg using ζ_{BVI} as given in Hamuy et al. (2001) (left panel) and Dessart & Hillier (2005) (right panel). The diamond markers denote values of χ through which the fit is made.

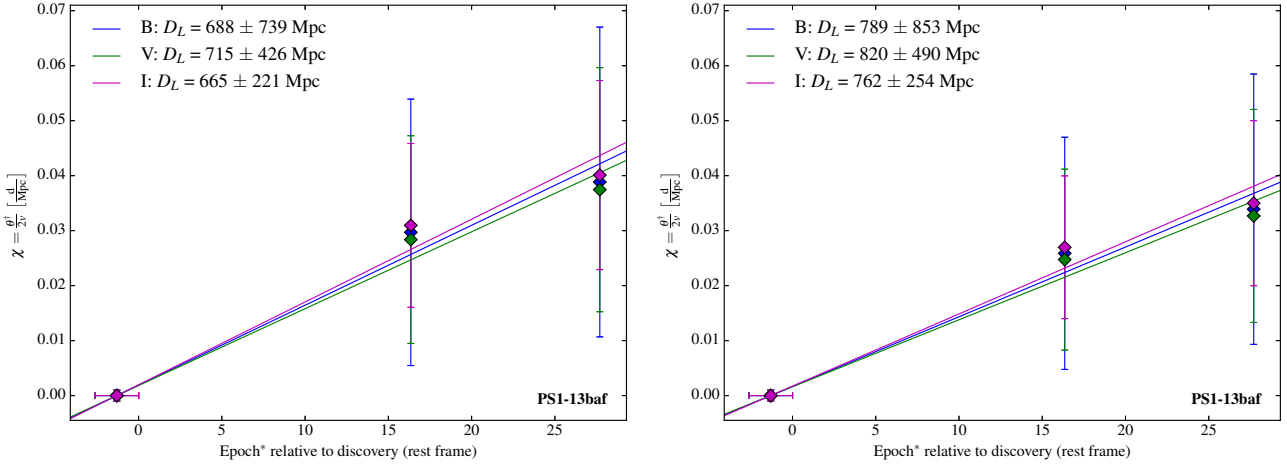


Fig. C.6: Distance fit for PS1-13baf using ζ_{BVI} as given in Hamuy et al. (2001) (left panel) and Dessart & Hillier (2005) (right panel). The diamond markers denote values of χ through which the fit is made.

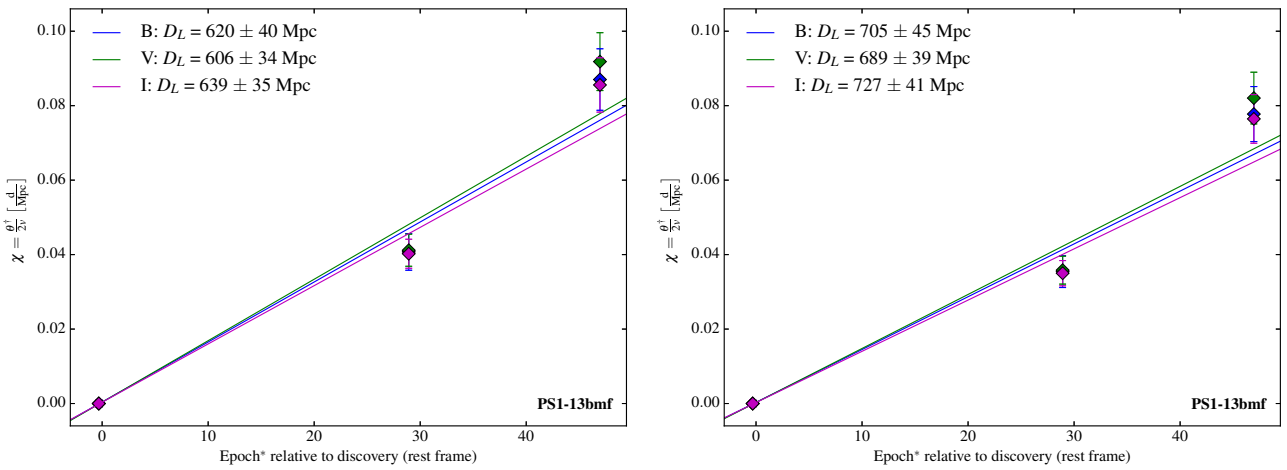


Fig. C.7: Distance fit for PS1-13bmf using ζ_{BVI} as given in Hamuy et al. (2001) (left panel) and Dessart & Hillier (2005) (right panel). The diamond markers denote values of χ through which the fit is made.

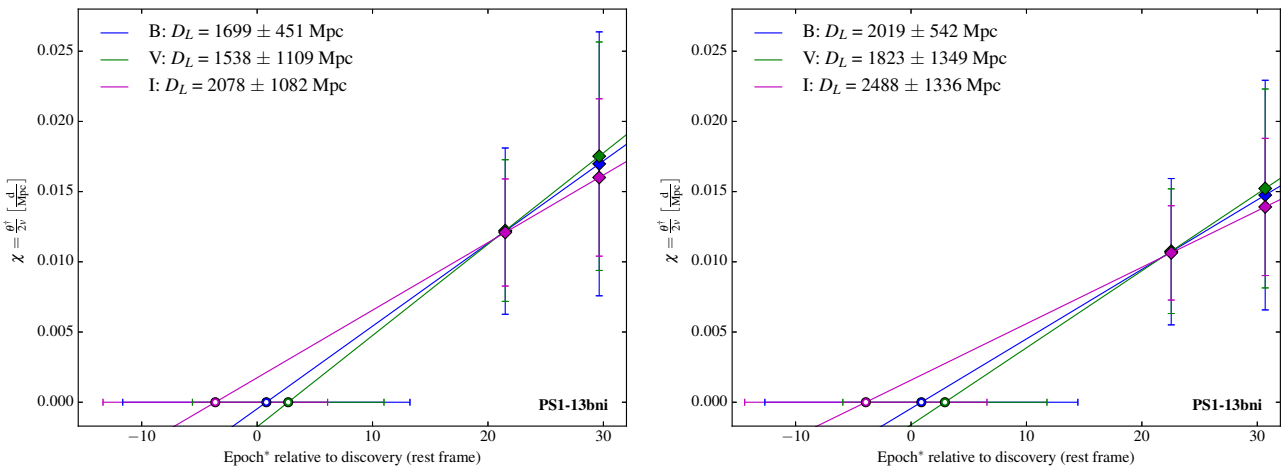


Fig. C.8: Distance fit for PS1-13bni using ζ_{BVI} as given in Hamuy et al. (2001) (left panel) and Dessart & Hillier (2005) (right panel). The diamond markers denote values of χ through which the fit is made. Note that this figure shows the last step of the iteration as described in Section 3.5.12.